

AD _____

Award Number DAMD17-96-1-6119

TITLE: MR Measurement of Breast Tissue's Anisotropic Mechanical Properties

PRINCIPAL INVESTIGATOR: John B. Weaver, Ph.D.

CONTRACTING ORGANIZATION: Dartmouth College
Hanover, New Hampshire 03755

REPORT DATE: July 1999

TYPE OF REPORT: Final

PREPARED FOR: U.S. Army Medical Research and Materiel Command
Fort Detrick, Maryland 21702-5012

DISTRIBUTION STATEMENT: Approved for Public Release;
Distribution Unlimited

The views, opinions and/or findings contained in this report are those of the author(s) and should not be construed as an official Department of the Army position, policy or decision unless so designated by other documentation.

20010122 079

REPORT DOCUMENTATION PAGE

Form Approved
OMB No. 0704-0188

Public reporting burden for this collection of information is estimated to average 1 hour per response, including the time for reviewing instructions, searching existing data sources, gathering and maintaining the data needed, and completing and reviewing the collection of information. Send comments regarding this burden estimate or any other aspect of this collection of information, including suggestions for reducing this burden, to Washington Headquarters Services, Directorate for Information Operations and Reports, 1215 Jefferson Davis Highway, Suite 1204, Arlington, VA 22202-4302, and to the Office of Management and Budget, Paperwork Reduction Project (0704-0188), Washington, DC 20503.

1. AGENCY USE ONLY (Leave blank)		2. REPORT DATE July 1999	3. REPORT TYPE AND DATES COVERED Final (1 Jul 96 - 30 Jun 99)	
4. TITLE AND SUBTITLE MR Measurement of Breast Tissue's Anisotropic Mechanical Properties			5. FUNDING NUMBERS DAMD17-96-1-6119	
6. AUTHOR(S) John B. Weaver, Ph.D.				
7. PERFORMING ORGANIZATION NAME(S) AND ADDRESS(ES) Dartmouth College Hanover, New Hampshire 03755			8. PERFORMING ORGANIZATION REPORT NUMBER	
9. SPONSORING / MONITORING AGENCY NAME(S) AND ADDRESS(ES) U.S. Army Material Research and Material Command Fort Detrick, Maryland 21702-5012			10. SPONSORING / MONITORING AGENCY REPORT NUMBER	
11. SUPPLEMENTARY NOTES This report contains colored photos				
12a. DISTRIBUTION / AVAILABILITY STATEMENT Approved for Public Release; Distribution Unlimited			12b. DISTRIBUTION CODE	
13. ABSTRACT (Maximum 200 words) The purpose of this grant was to develop methods to estimate the mechanical properties of tissue, especially the elasticity, in vivo. These methods will be used to evaluate mechanical properties, such as the elasticity, as indicators of breast cancer. MR images were used to measure the displacement of tissue resulting from a low frequency vibration of the tissue. We developed methods of vibrating tissue in the magnetic field of the MR system, developed the MR pulse sequences that measure the resulting displacement and developed the an algorithm to reconstruct the elasticity from the measured displacements. The algorithm to reconstruct the elasticity allows spatial resolution a factor of at least ten better than previous methods.				
14. SUBJECT TERMS Breast cancer			15. NUMBER OF PAGES 71	
			16. PRICE CODE	
17. SECURITY CLASSIFICATION OF REPORT Unclassified	18. SECURITY CLASSIFICATION OF THIS PAGE Unclassified	19. SECURITY CLASSIFICATION OF ABSTRACT Unclassified	20. LIMITATION OF ABSTRACT Unlimited	

FOREWORD

Opinions, interpretations, conclusions and recommendations are those of the author and are not necessarily endorsed by the U.S. Army.

NA Where copyrighted material is quoted, permission has been obtained to use such material.

NA Where material from documents designated for limited distribution is quoted, permission has been obtained to use the material.

Y Citations of commercial organizations and trade names in this report do not constitute an official Department of Army endorsement or approval of the products or services of these organizations.

NA In conducting research using animals, the investigator(s) adhered to the "Guide for the Care and Use of Laboratory Animals," prepared by the Committee on Care and use of Laboratory Animals of the Institute of Laboratory Resources, national Research Council (NIH Publication No. 86-23, Revised 1985).

NA For the protection of human subjects, the investigator(s) adhered to policies of applicable Federal Law 45 CFR 46.

NA In conducting research utilizing recombinant DNA technology, the investigator(s) adhered to current guidelines promulgated by the National Institutes of Health.

NA In the conduct of research utilizing recombinant DNA, the investigator(s) adhered to the NIH Guidelines for Research Involving Recombinant DNA Molecules.

NA In the conduct of research involving hazardous organisms, the investigator(s) adhered to the CDC-NIH Guide for Biosafety in Microbiological and Biomedical Laboratories.

John Weir 7/26/99
PI - Signature Date

Table of Contents:

Front Cover	1
Standard Form (SF) 298, Report Documentation Page	2
Foreword	3
Table of Contents	4
Introduction	5
Body	6
Research Accomplishments	9
Reportable Outcomes	9
Conclusions	10
References and List of Personnel	11
Appendices	13

Introduction:

The purpose of this grant was to develop methods to estimate the mechanical properties of tissue, especially the elasticity, in vivo. These methods will be used to evaluate those mechanical properties as indicators of breast cancer. MR images were used to measure the displacement of tissue resulting from a low frequency vibration of the tissue. We developed methods of vibrating tissue in the magnetic field of the MR system, developed the MR pulse sequences that measure the resulting displacement and developed the an algorithm to reconstruct the elasticity from the measured displacements. The algorithm to reconstruct the elasticity allows resolutions a factor of at least ten better than previous methods.

Body:

- *Technical Objective 1: Refine the MR measurement of three dimensional displacement during vibration. Build the high power, low noise apparatus to measure the three dimensional displacement during vibration. Compare the measured displacement to measurements from a calibrated hydrophone and tune the system.*

We have developed a driver to vibrate tissue at low frequencies in the MR magnet. It is made of three stacks of piezoelectric crystals that produce very high forces and have a very linear response. See Fig. 1 below. The apparatus is described in the manuscript submitted to Medical Physics [2] and included in the Appendix. We have measured displacements in the magnet using a gradient echo pulse sequence that measures displacements in all three directions. The measured displacements agree well with independent measurements using a Capacitec Model 410-SC probe. The displacements measured with the MR and the Capacitec probe agree very well; the gel at the edges of the phantoms are within 25% with the Capacitec measurements of the motion of the plastic wall holding the phantom.

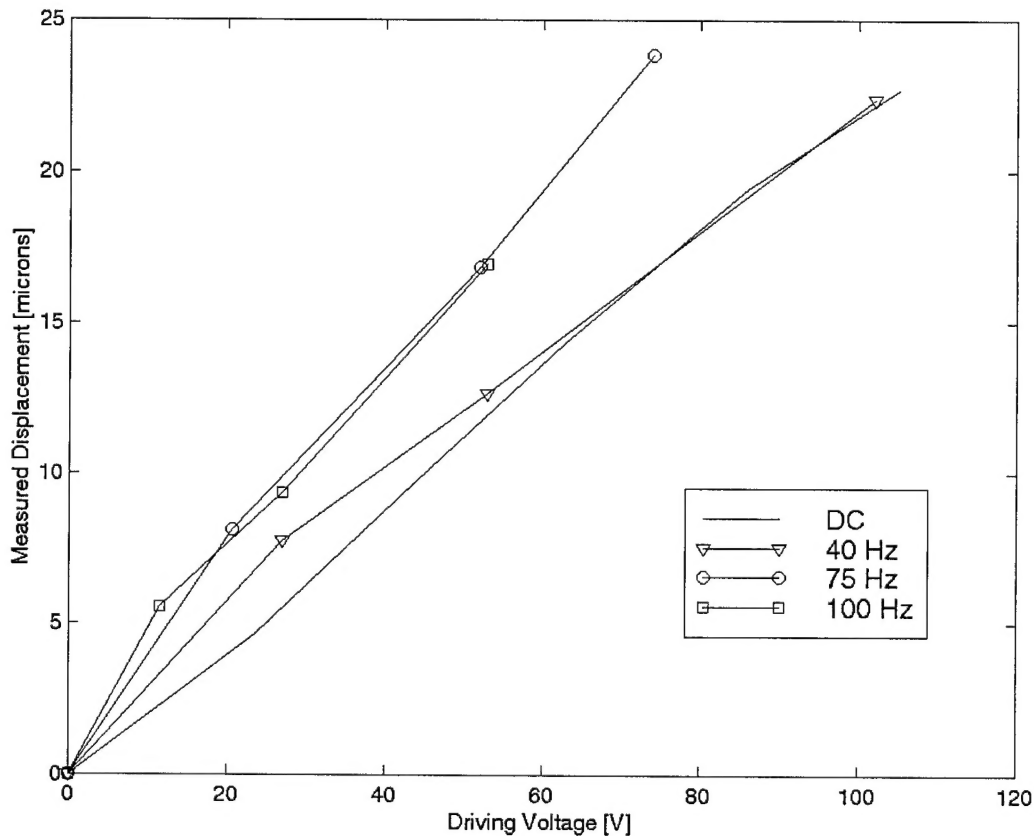


Figure 1: The measured displacements vs. driving voltage at several frequencies.

We also developed noise reduction methods to improve the MR estimates of displacement [3,4,5,8,10] especially at very low displacement.

- *Technical Objective 2: Compare the elasticity calculated from the MR displacements with a linear model to known elasticity's for isotropic and anisotropic materials. Modify the scale with the vernier to measure the elasticity manually with a mechanical method. Build phantoms and compare the elasticity calculated from the MR displacements with a linear model to known elasticity's for isotropic and anisotropic materials.*

We have implemented finite element code that models the displacement of a variety of gels and tissue. It is clear from the MR measurements and from the simulations that the full partial differential equation is needed to accurately describe the system. Representative examples of those simulations are shown in [1,2,6,9]. Copies of the posters and papers are in the Appendix. We have measured the elasticity of gel phantoms with mechanical methods, by estimating the wavelength of 100 Hz vibrations in the MR displacement images and by the inversion of the partial differential equations using the method we developed and have reported on in Mag. Reson. Med. [1]. The three methods agree to a reasonable extent. However, we believe the best way to estimate the elasticity of homogeneous gels is by estimating the wavelength in the MR displacement images. Any frequency effects are accounted for and Poisson's ratio need not be estimated. These results are also shown in the four publications listed above and included in the Appendix.

- *Technical Objective 3: Establish the limits of the linear, lossless elastic model of tissue motion during vibration. Find the dependence of MR elasticity on the frequency and amplitude of the vibration. Measure motion perpendicular to the direction of forced vibration. Measure viscous losses by the attenuation of the vibration across the material. Develop and test finite element code to calculate the displacement. Compare the measured displacements with the displacements calculated with a finite element analysis for: Phantoms with simple geometry, Complicated phantoms, Lean meat (probably a roast), Meat with fat and muscle (probably a slab of bacon).*

We have established the limits of the linear model with simulations and measurements on phantoms (results of technical objective 2) without getting to more complicated structures; the full partial differential equations (PDE's) are required to describe motion accurately. We have measured viscous losses with reconstruction methods [2,7,9]. We have developed finite element code to calculate the displacements with known materials (the forward problem) and compared them to measured displacements [1,2,6,7,9].

The results we now have suggest that we need to measure steady state vibration in the tissue to allow accurate reconstruction of the elasticity using the PDE's for harmonic motion. The PDE's for harmonic motion assume steady state motion. It is possible to solve the PDE's for transient motion as well but it is significantly easier to solve the steady state equations than the equations for transient motion. We have designed a system to drive the tissue in steady state using the MR system's clock so the vibration remains in sync with the MR over the entire acquisition [11]. We have begun to gather steady state data on gels and the reconstructions are very good [11].

We have made some, limited tissue measurements as well as measurements on gels. We were lucky enough to get some breast tissue from a breast reduction surgery. We made measurements on that tissue instead of the meat we proposed because it represents real breast tissue much better than

meat which is mostly muscle. Recent publications such as [Krouskop, T.A, et. al., "Elastic moduli of breast and prostate tissues under compression" Ultrasonic Imaging 20(4):260-74, 1998], suggest that there are significant differences between breast tissue and muscle. The MR images of breast tissue from breast reduction surgery are excellent but the motion is very small because the mechanical coupling between the tissue and the plexiglas wall is poor without the skin to hold the tissue. There are several possible approaches to the coupling problem but we had no time to pursue them. However, we did make a first effort at vibrating breasts of volunteers. We have measured adequate vibrations in a volunteer but the apparatus proved to be too uncomfortable to use. We are currently modifying the apparatus extensively to make it usable; this work is being done under the new NIH grant.

There are two significant aspects to our reconstruction algorithm [1,2,7,11,12]. The most significant aspect of the new algorithm is that it reconstructs the elasticity with resolution on the order of the pixel size of the MR images. Previous elasticity estimates from dynamic displacements had spatial resolution on the order of the wavelength of the vibration which is much larger than the pixel size. The other significant aspect of the algorithm is that it is readily extended to three dimensional problems [12]. The zones used in the method can be made small enough that they can be solved in three dimensions. There are several groups that believe the three dimensional problem must be solved to get accurate estimates of the elasticity in vivo.

We believe that extensive in vivo measurements should be possible in approximately one year. Clinical results should then yield the usefulness of elasticity in breast cancer detection. The current line of research provides a workable approach to generating elasticity from dynamic vibration. The results of this work should be compared to the elasticity estimates from quasi-static MR and ultrasound to see if the extra information generated from dynamic measurements is productive.

Research Accomplishments:

- Method of reconstructing the in vivo elasticity from measured displacements. The method has been tested in 2D and can be extended to 3D.
- Developed apparatus to vibrate tissue in the MR with large forces and accurate synchronization with the MR imaging system.
- New noise reduction methods were developed to improve the MR estimates of displacement.

Reportable Outcomes:

- Five papers and five peer reviewed presentations with abstracts have resulted from this grant. The papers and presentations are listed in the Bibliography.
- The methods and results from the work supported by this grant have formed one section of a Program Project Grant submitted to the NIH in June of 1998. It received very good scores and was resubmitted in June of 1999. The 1999 resubmission was funded.

Conclusions:

We have shown that partial differential equation solutions are needed to accurately estimate the elasticity from measured displacements, even with very small displacements. Further, we have proposed and tested an algorithm to solve for the elasticity from measured displacements. The algorithm performs exceptionally well in simulation and produces generally accurate solutions from measured data. We have good evidence that most of the inaccuracies in the reconstruction of measured data results from transient effects in the tissue vibration. The most significant aspect of the new algorithm is that it reconstructs the elasticity with resolution on the order of the pixel size of the MR images. Previous elasticity estimates from dynamic displacements had spatial resolution on the order of the wavelength of the vibration which is much larger than the pixel size.

With improved steady state vibration, which we have developed and have begun testing, and the extension of our reconstruction algorithm from 2D to 3D, which we have started, obtaining accurate estimates of the elasticity of tissue in vivo is possible. Therefore, clinical evaluation of elasticity as an indicator of cancer should be possible within a year or, at most, two.

Publications and abstracts resulting from the research supported by this grant:

Publications:

- 1.) E.E.W. Van Houten, K.D. Paulsen, M.I. Miga, F.E. Kennedy and J.B. Weaver: "An Overlapping Subzone Technique for MR Based Elastic Property Reconstruction," Magnetic Resonance in Medicine 42(4):779-786.
- 2.) E.E.W. Van Houten, J.B. Weaver, M.I. Miga, F.E. Kennedy and K.D. Paulsen: "Elasticity Reconstruction from Experimental MR Displacement Data: Initial Experience with an Overlapping Subzone Finite Element Inversion Process," Medical Physics 27(1):101-107.
- 3.) J.B. Weaver: "Applications of Monotonic Noise Reduction Algorithms in fMRI, Phase Estimation and Contrast Enhancement," International Journal of Imaging Science and Technology, Special Issue on Signal Processing in MRI, pp 177-185 (invited paper), 1998.
- 4.) J.B. Weaver: "Reducing Noise in Images by Forcing Monotonic Change Between Extrema," Inverse Problems, Tomography, and Image Processing (ISAAC), pp189-199 (invited paper), 1997.
- 5.) J. B. Weaver: "Monotonic Noise Suppression Used to Improve the Sensitivity of fMRI Activation Maps," Journal of Digital Imaging 11:3 Suppl 1, pp. 46-52, Aug 1998.

Peer Reviewed Presentations with Abstracts:

- 6.) J.B. Weaver, E.E.W. Van Houten, M. I. Miga, F. E. Kennedy, A. Hartov, S. P. Poplack, H. M. Nagy, K. D. Paulsen: "Measurement of Harmonic Motion for MR Elastography," Proceedings of the Society of Magnetic Resonance, Philadelphia, Pennsylvania, May, 1999, p. 1617 (Abstract).
- 7.) E.E.W. Van Houten, M. I. Miga, F.E. Kennedy, J.B. Weaver and K.D. Paulsen: "MRI Elastography Reconstruction Using a Harmonic Elastodynamic Model," Proceedings of the Society of Magnetic Resonance, Philadelphia, Pennsylvania, May, 1999, p. 260 (Abstract).
- 8.) J.B. Weaver: "Contrast Enhancement Using Monotonic Noise Suppression Methods," American Association of Physicists in Medicine (AAPM), July 1998. Medical Physics 25(7) part 1, p. A122-3 (Abstract).
- 9.) J.B. Weaver, E.E. Van Houten, M.I. Miga, K.D. Paulsen: "Elasticity estimates using phase contrast MRI measurements of displacement," American Association of Physicists in Medicine (AAPM), July 1998. Medical Physics 25(7) part 1, p. A212 (Abstract).
- 10.) J.B. Weaver: "Removing Noise from Images: Least Squares Monotonic Functions on Line Segments Through the Image" Proceedings of the Society of Magnetic Resonance, Vancouver, Canada, August, 1997, p 2043 (Abstract).
- 11.) J.B. Weaver, E.E.W. Van Houten, M. I. Miga, F. E. Kennedy and K. D. Paulsen: "Acquisition of MR Elastography Measurements Using Steady State Motion," Accepted for the Proceedings of the Society of Magnetic Resonance, Denver, Col.,

May, 2000.

- 12.) E.E.W. Van Houten, M. I. Miga, F. E. Kennedy, J.B. Weaver and K. D. Paulsen:
"Three Dimensional Reconstructive Elastography Imaging," Accepted for the
Proceedings of the Society of Magnetic Resonance, Denver, Col., May, 2000.

Personnel Supported by This Grant:

John B. Weaver, Ph.D.

Senthil Periaswamy

Hongxia Quan

Nader S. Akhnoukh

Appendices:

An Overlapping Subzone Technique for MR-Based Elastic Property Reconstruction

E.E.W. Van Houten,^{1*} K.D. Paulsen,^{1,2,3} M.I. Miga,¹ F.E. Kennedy,¹ and J.B. Weaver²

A finite element-based nonlinear inversion scheme for magnetic resonance (MR) elastography is detailed. The algorithm operates on small overlapping subzones of the total region of interest, processed in a hierarchical order as determined by progressive error minimization. This zoned approach allows for a high degree of spatial discretization, taking advantage of the data-rich environment afforded by the MR. The inversion technique is tested in simulation under high-noise conditions (15% random noise applied to the displacement data) with both complicated user-defined stiffness distributions and realistic tissue geometries obtained by thresholding MR image slices. In both cases the process has proved successful and has been capable of discerning small inclusions near 4 mm in diameter. *Magn Reson Med* 42:779–786, 1999. © 1999 Wiley-Liss, Inc.

Key words: elasticity reconstruction; nonlinear inversion; finite element method; magnetic resonance elastography; subzone technique; model-based imaging

The diagnostic value of tissue elasticity has long been appreciated in a broad spectrum of medical applications, and understanding of its importance continues to grow. From pathology detection (1,2), to robotic surgery (3,4), to the use of computational modeling during surgical procedures (5–7), a demand for detailed and accurate tissue elasticity information has been generated. Recent research into the use of mechanical properties of biological tissue for clinical decision making has moved away from direct mechanical measurements (8,9) and turned toward various medical imaging technologies to assess tissue behavior under mechanical loads. The idea of ultrasound elastography has been introduced (10–16) in which some form of ultrasonic displacement measurement technique is used to detect subsurface tissue motion. This displacement information can then be correlated to the elastic property distribution in the tissue with the aid of a model for tissue motion as a function of shear or Young's modulus (17–19).

Ultrasound's inherent lack of lateral resolution and limited axial resolution when compared with other clinically available imaging modalities has motivated the development of magnetic resonance (MR) elastography methods (20–22). MR offers the potential of generating highly resolved, three-dimensional (3D) information with relative ease, as opposed to the considerable challenge associated with obtaining equivalent data from ultrasound techniques. However, given the availability of finely sampled

3D displacement fields, the task of developing a robust algorithm capable of deducing elastic property distributions from these displacement images while maintaining the refinement of the MR data remains.

Strategies for addressing the reconstruction problem have varied widely to date. Chenevert et al. are investigating MR elastography through a quasistatic displacement approach (23), whereas Raghavan and Yagle have developed an inversion technique based on a finite difference formulation of the global elasticity equations (24). A collaboration between Lewa and De Certaines has attempted to determine the viscoelastic properties directly from MR measurements (25). Manduca et al. have developed an inversion scheme based on a local frequency estimation that is correlated to a local elasticity value (26), and Sumi and Nakayama have presented a method for numerically integrating the two-dimensional (2D) stress-strain relations to reconstruct a shear modulus distribution from strain measurements (27).

In this report, we present a finite element-based method for solving the elastography inversion problem by use of a least-squares minimization of the difference between measured displacement data from the MR and computed displacement solutions. Our approach is not unlike that recently presented by Kallel and Bertrand for ultrasound techniques (18), except that model-based optimization is performed on small overlapping subzones of the total tissue region of interest that are processed in an hierarchical order determined by progressive error minimization. This is a significant shift in the conceptual framework for property inversion that allows the recovery of an elasticity distribution at the MR displacement measurement resolution. Property estimation at the MR pixel level is not computationally viable as a single global minimization problem; however, the subzone approach we have identified eliminates this limitation by recasting the image reconstruction objective as a sum of minimizations rather than a single minimization of sums. The results show that the overlapping zone concept is robust with respect to simulated measurement noise and that local minimization of the least-squares match between the model and the MR displacement data leads to high-quality global property distribution images.

SUBZONE INVERSION

Our approach capitalizes on recent advances in model-based image reconstruction of tissue properties whereby the nonlinear relationship between the physical property distribution to be determined and the measured tissue response to an applied stimulus is preserved (28–30). Specifically, we formulate the MR elastography image-reconstruction problem as a constrained optimization task

¹Thayer School of Engineering, Dartmouth College, Hanover, New Hampshire.

²Dartmouth Hitchcock Medical Center, Lebanon, New Hampshire.

³Norris Cotton Cancer Center, Lebanon, New Hampshire.

Grant sponsor: National Institute of Neurological Disorders and Stroke; Grant number: R01-NS33900.

*Correspondence to: Elijah Van Houten, 8000 Cummings Hall, Dartmouth College, Hanover, NH 03755. E-mail: elijah.van.houten@dartmouth.edu

Received 15 April 1999; revised 1 July 1999; accepted 6 July 1999.

© 1999 Wiley-Liss, Inc.

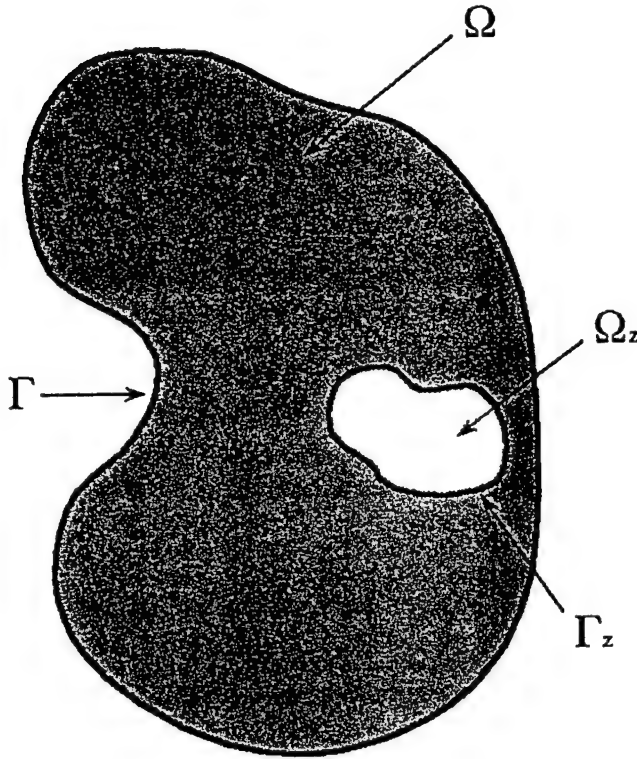


FIG. 1. Schematic diagram of the subzone concept. Ω , total problem domain; Γ , boundary; Ω_z , single subzone domain; Γ_z , single subzone boundary.

whose objective is to minimize the difference between a set of measured displacement fields and those computed by a model description in which the tissue property distribution is parameterized as a set of unknown coefficients. The typical strategy is to define a single objective to be minimized that is the sum of the squared differences between measured and calculated quantities over the entire set of tissue response observations that are available (31):

$$\min F(E), \quad [1a]$$

where

$$F(E) = \sum_{l=1}^N (u_l^m - u_l^c)^2 + (v_l^m - v_l^c)^2 \quad [1b]$$

and u_l^m and v_l^m are the x and y vector components of the measured displacement at location l , while u_l^c and v_l^c are the calculated vector components at the same position, for a total of N different locations. E is the M -dimensional vector of elasticity parameters that is expanded on a continuous basis set, ϕ , to define the tissue property distribution of the total region of interest, Ω .

This total problem domain, Ω , may be thought of as the union of multiple "subzones," Ω_z , of the total ROI, as illustrated in Fig. 1, so that we may rewrite the global functional, $F(E)$, as a sum of locally defined functionals,

$F_z(E_z)$, for the z th subzone. For Q subzones,

$$F(E) = \sum_{z=1}^Q F_z(E_z), \quad [2]$$

where the minimization of the sum is replaced by the sum of minimizations on the individual subzones:

$$\min F(E) = \min \left\{ \sum_{z=1}^Q F_z(E_z) \right\} \Rightarrow \sum_{z=1}^Q \min F_z(E_z) \quad [3a]$$

with

$$F_z(E_z) = \sum_{l_z=1}^{N_z} (u_{l_z}^m - u_{l_z}^c)^2 + (v_{l_z}^m - v_{l_z}^c)^2, \quad [3b]$$

when each subzone consists of N_z tissue response observations and M_z tissue property parameters such that $N_z \ll N$ and $M_z \ll M$.

The advantages of this approach are severalfold. First, the nonlinear minimization process occurs on only M_z tissue property parameters using N_z observations at a time. The significant reduction in the size of the inversion problem is important because the least-squares approach scales cubically in the number of optimization parameters to be determined. Second, it maximizes the utilization of the complete MR displacement data set and the concomitant tissue property resolution that can be achieved. Assuming that tissue displacements can be measured at the MR pixel level, the total amount of tissue response data and tissue property values that could be recovered in a single minimization problem exceeds the computational resources available today. By dividing the problem into subzones, high-resolution (MR pixel-level) property maps can be deduced that take full advantage of the high density of tissue measurements that the MR technique provides.

Once defined on the subzone, the minimization problem proceeds in standard fashion. Determination of the subzone elastic properties requires differentiation of F_z in Eq. [3b] with respect to each of the M_z property parameters contained in E_z , which produces the nonlinear system

$$\begin{aligned} f_1 &= \frac{\partial F_z}{\partial E_{z_1}} = \sum_{l_z=1}^{N_z} (u_{l_z}^m - u_{l_z}^c) \frac{\partial u_{l_z}^c}{\partial E_{z_1}} + \sum_{l_z=1}^{N_z} (v_{l_z}^m - v_{l_z}^c) \frac{\partial v_{l_z}^c}{\partial E_{z_1}} = 0 \\ f_2 &= \frac{\partial F_z}{\partial E_{z_2}} = \sum_{l_z=1}^{N_z} (u_{l_z}^m - u_{l_z}^c) \frac{\partial u_{l_z}^c}{\partial E_{z_2}} + \sum_{l_z=1}^{N_z} (v_{l_z}^m - v_{l_z}^c) \frac{\partial v_{l_z}^c}{\partial E_{z_2}} = 0 \\ &\vdots \\ f_{M_z} &= \frac{\partial F_z}{\partial E_{z_{M_z}}} = \sum_{l_z=1}^{N_z} (u_{l_z}^m - u_{l_z}^c) \frac{\partial u_{l_z}^c}{\partial E_{z_{M_z}}} \\ &\quad + \sum_{l_z=1}^{N_z} (v_{l_z}^m - v_{l_z}^c) \frac{\partial v_{l_z}^c}{\partial E_{z_{M_z}}} = 0. \end{aligned} \quad [4]$$

Solution of this equation set by Newton's method leads to iterative improvements in the elastic property profile such that

$$E_z^{(n+1)} = E_z^n + \Delta E_z, \quad [5a]$$

where ΔE_z is the property update vector determined from the solution of the regularized matrix system

$$[(H_z^n + \alpha I)] [\Delta E_z] = [-f_z^n] \quad [5b]$$

with $f_z = [f_1^n, f_2^n, \dots, f_{M_z}^n]^T$ and the approximate Hessian matrix (second-order terms are dropped), H_z^n , having the elements

$$h_{ij}^n = \frac{\partial f_i^n}{\partial E_{z_j}^n} = - \sum_{l_z=1}^{N_z} \left[\frac{\partial u_{l_z}^f}{\partial E_{z_i}^n} \frac{\partial u_{l_z}^c}{\partial E_{z_j}^n} + \frac{\partial v_{l_z}^c}{\partial E_{z_i}^n} \frac{\partial v_{l_z}^c}{\partial E_{z_j}^n} \right] \quad [5c]$$

evaluated at the current property estimate denoted by the superscript n . In Eq. (5b), α is a scalar regularization parameter added to the diagonal of H to facilitate its inversion, because H is known to be poorly conditioned. This parameter is scaled to the subzone problem at hand by use of the Levenberg-Marquardt approach (32).

Solution of Eq. (5b) requires a vehicle for calculating the subzone displacement field and its derivatives with respect to each property parameter given the current estimate of the property distribution on the subzone. Here, we assume that the displacement field is described by the partial differential equation governing time-harmonic, isotropic, linearly elastic motion:

$$\nabla \cdot G \nabla \mathbf{u} + \nabla(\lambda + G) \nabla \cdot \mathbf{u} = -\rho \omega^2 \mathbf{u}, \quad [6a]$$

where \mathbf{u} is the displacement vector, ρ is the tissue density and G and λ are Lamé's constants

$$G = \frac{E}{(2 + 2\nu)} \quad [6b]$$

$$\lambda = \frac{\nu E}{(1 + \nu)(1 - 2\nu)} \quad [6c]$$

for Poisson's Ratio, ν , and Young's modulus, E . For simplicity, we consider ρ and ν to be known constants, leaving G , or equivalently E , as the elastic property parameter distribution to be estimated from the displacement field. To solve Eq. (6a), we use the finite element method as summarized in the Appendix.

The required derivatives are calculated by differentiating Eq. (6a) directly with respect to each property parameter, E_{z_j} for $j = 1, 2, \dots, M_z$, and solving the resulting partial differential equation in the derivative quantity of interest

on the same finite element discretization:

$$\begin{aligned} \frac{\partial}{\partial E_{z_j}} [\nabla \cdot G \nabla \mathbf{u} + \nabla(\lambda + G) \nabla \cdot \mathbf{u}] &= -\rho \omega^2 \frac{\partial \mathbf{u}}{\partial E_{z_j}} \\ &= \nabla \cdot \frac{\partial G}{\partial E_{z_j}} \nabla \mathbf{u} + \nabla \cdot G \nabla \frac{\partial \mathbf{u}}{\partial E_{z_j}} + \nabla \frac{\partial}{\partial E_{z_j}} (\lambda + G) \nabla \cdot \mathbf{u} \\ &\quad + \nabla(\lambda + G) \nabla \cdot \frac{\partial \mathbf{u}}{\partial E_{z_j}} = -\rho \omega^2 \frac{\partial \mathbf{u}}{\partial E_{z_j}}, \quad [7a] \end{aligned}$$

which when rewritten in the form

$$\begin{aligned} \nabla \cdot G \nabla \mathbf{u}_j' + \nabla(\lambda + G) \nabla \cdot \mathbf{u}_j' &= -\rho \omega^2 \mathbf{u}_j' - \nabla \cdot \frac{\partial G}{\partial E_{z_j}} \nabla \mathbf{u} \\ &\quad - \nabla \frac{\partial}{\partial E_{z_j}} (\lambda + G) \nabla \cdot \mathbf{u}, \quad [7b] \end{aligned}$$

where $\mathbf{u}_j' = \partial \mathbf{u} / \partial E_{z_j}$, has the identical form of Eq. (6a) in the quantity \mathbf{u}_j' except for the occurrence of two additional right-hand-side quantities expressed in terms of \mathbf{u} . Because Eq. (5b) is evaluated at the current property estimate, \mathbf{u} can be computed through Eq. (6a) leaving \mathbf{u}_j' as the only unknown in Eq. (7b). Evaluation of the terms expressing the differentiation of the elastic property distribution with respect to its parameterization, $\partial G / \partial E_{z_j}$, is facilitated by expanding the elastic constants in the finite element basis so that $E = \sum_{j=1}^{M_z} E_{z_j} \phi_j$. The finite element discretization of Eq. (7b) is described in further detail in the Appendix.

In practice, the subzone inversion algorithm begins with an initial estimate of the elastic property distribution, E^0 , defined over the entire problem space, Ω . From this estimate, a global displacement field, \mathbf{u}^c , is computed from Eq. (6a) with the finite element method based on known displacement conditions from the MR data set, \mathbf{u}^m , applied along the global boundary, Γ . The squared error between the resulting displacement solution and the measured MR data is then calculated for each element. By using this error metric, an hierarchical list of element centroids is generated in which the element order is based on a decreasing squared-error contribution. A subzone domain, Ω_z , is then formed about an element centroid in the list by including all nearby elements whose centroids are within a user-defined radial distance from the subzone center. Figure 2 shows an example of a simple global finite element mesh with a close-up view of a single subzone that has been extracted for illustrative purposes. Once the subzone has been identified, a displacement field is calculated on the subzone by using the latest property parameter estimate, E_z^n , and the MR displacement information on the subzone boundary, Γ_z , as the boundary conditions required for finite element solution. The subzone property distribution is iteratively updated with the inversion process embodied in Eq. (5b) until a local convergence criterion between the computed and measured displacements internal to the subzone has been reached. At this point, the next element centroid in the error contribution list having participated in the fewest inversion operations is used to define another subzone, and the process of local convergence in the displacement field between computed and measured quan-

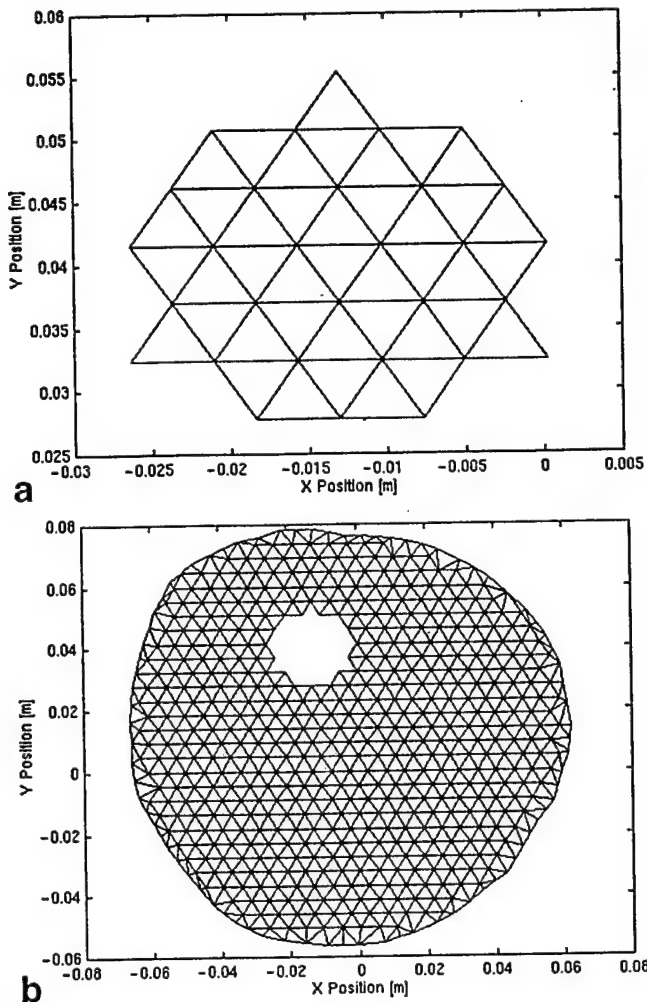


FIG. 2. Illustration of the mesh-based subzone technique in which a single subzone (a) has been extracted from a global finite element mesh (b).

ties is repeated. The zoning process continues until every element in the global mesh has been iterated a minimum number of times. The subzone solutions then end, another global displacement field calculation is executed with the latest property profile, and the zoning procedure begins again. Figure 3 illustrates the overall image reconstruction process.

RESULTS

Initial evaluations of the zoning algorithm have been performed on various numerical simulations of the displacement patterns generated in vibrating tissue. For these experiments, synthetic data were produced with the finite element method displacement calculation described in the Appendix. The mesh geometries were developed from MR images taken from actual patients, one being a modified anatomically coronal breast slice and the other a coronal brain image. For simplicity, we have assumed that the only unknown elastic parameter is Young's modulus, although this is not an inherent limitation in our algorithmic approach per se. Values for tissue density and Poisson's ratio were prescribed as 1020 kg/cm^3 and 0.49 , respectively. The small wavelengths that develop in soft tissue (a Young's modulus of 8000 Pa was used for the background tissue value here) require that the planar MR image be divided into a large number of elements to ensure that the wave propagation is adequately well resolved. For example, the mesh used for the breast geometry consisted of $16,555$ nodes and $32,635$ linear triangular elements, resolving the tissue continuum to approximately 0.8 mm . The wavelength of a 100-Hz shear wave in this case is 1.62 cm/cycle , so this resolution provides approximately 18 or 19 nodes per mechanical wavelength. For synthetic data production, a spatial elasticity distribution is required. We have generated property distributions by thresholding MR images that contain either an arbitrary, user-defined elasticity map, as shown in Figure 4a, or one that follows tissue substructures that are identifiable in the MR image, as represented

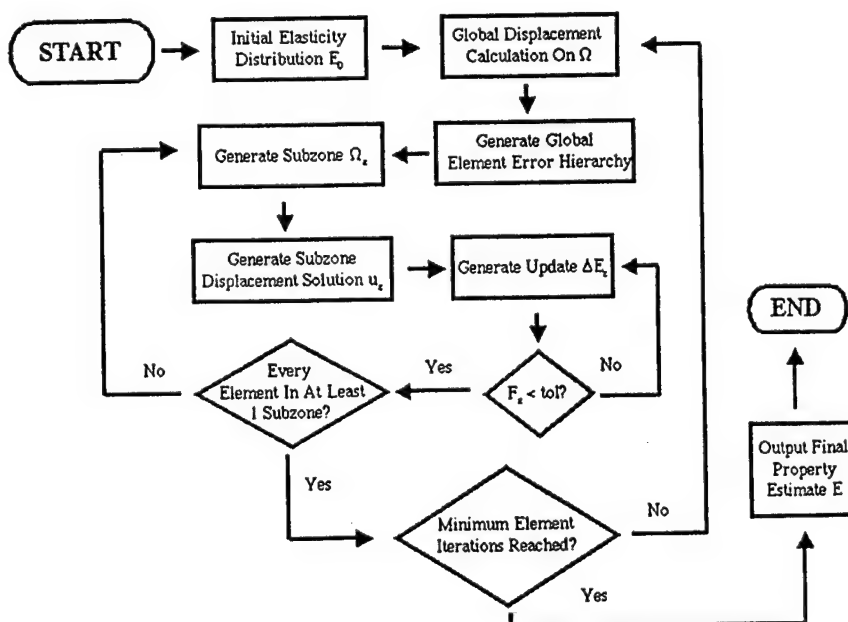


FIG. 3. Flowchart of the subzone inversion algorithm.

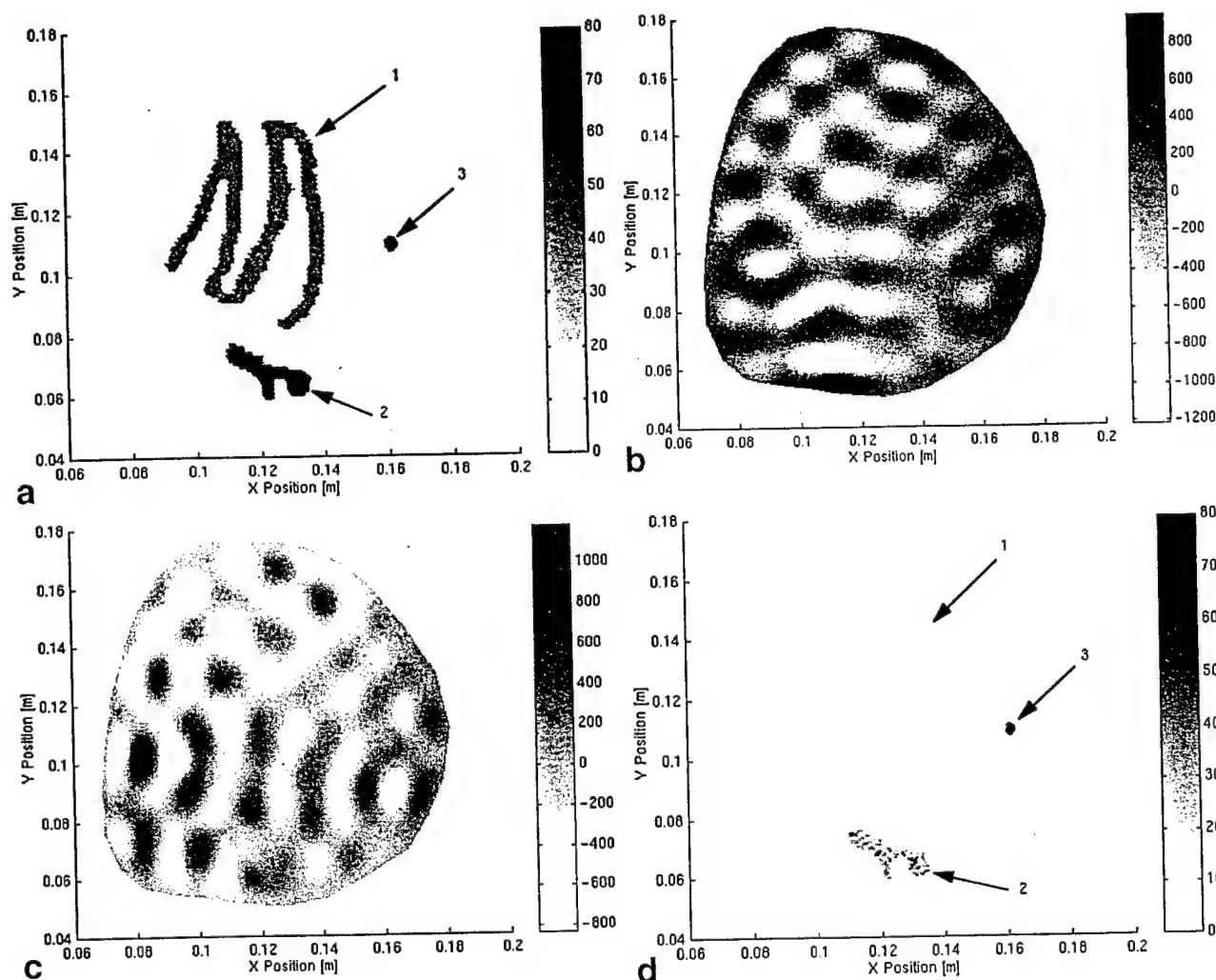


FIG. 4. Breast elasticity problem consisting of an artificial property distribution containing three heterogeneities of increasing contrast with the background. **a**: Exact Young's modulus distribution (kPa), which includes three heterogeneities, designated as objects 1, 2, and 3. **b**: Synthetic x-direction displacement magnitude (μm). **c**: Synthetic y-direction displacement magnitude (μm). **d**: Reconstructed Young's modulus distribution (kPa) in the presence of 15% measurement noise.

in Figure 5a. Before inversion, a certain percentage of random noise is added to the synthetic data to simulate signal degradation that will occur in practice. This noise is generated by scaling the average displacement with a random number up to a given percentage and adding or subtracting that value from the original displacement at a particular node. The noisy solution is then used by the inversion algorithm described above as the measured data set.

For the breast case, an elasticity distribution was created that provided challenging inclusion geometries as well as a variety of inclusion stiffnesses. The background tissue stiffness was assigned a Young's modulus of 8000 Pa, which is believed to be at the lower end of actual soft tissue values (8,9,33). Inclusion stiffness ranges were determined as multiples ($2\times$ for object 1, $5\times$ for object 2 and $10\times$ for object 3 in Fig. 4a) of the background stiffness to test the contrast resolution of the numerical algorithm. The stiffest of the inclusions (object 3 in Fig. 4a) is roughly 4 mm in diameter, representing a very small tumor within the tissue. Once the stiffness information has been formulated for the forward problem, boundary conditions of 100 Hz

and 10 μm sinusoidal displacements are applied and the displacement solution is generated, shown here as x and y displacement magnitudes in Fig. 4b and c, respectively. Note the complex nature of this displacement pattern. For the small wavelengths expected in soft tissue, these complex displacement fields could lead to difficulties in generating property distributions based on direct interpretation of the displacement or strain image. The property inversion shown in Fig. 4d was generated by using synthetic data with 15% added noise with an initial guess of a uniform Young's modulus of 7000 Pa. The inversion process consisted of 18 sweeps over the entire space, each sweep involving roughly 1000 subzones of approximately 150 elements and 100 nodes each to ensure that every node was operated on at least once.

To demonstrate the ability of the algorithm to process realistic geometries generated from MR images, an elasticity distribution was reconstructed on a mesh generated from a coronal brain slice with two simulated inclusions as shown in Fig. 5a. To ensure accurate resolution, this mesh consisted of 19,446 nodes and 38,332 linear triangular elements. For this tissue, a background Young's modulus of

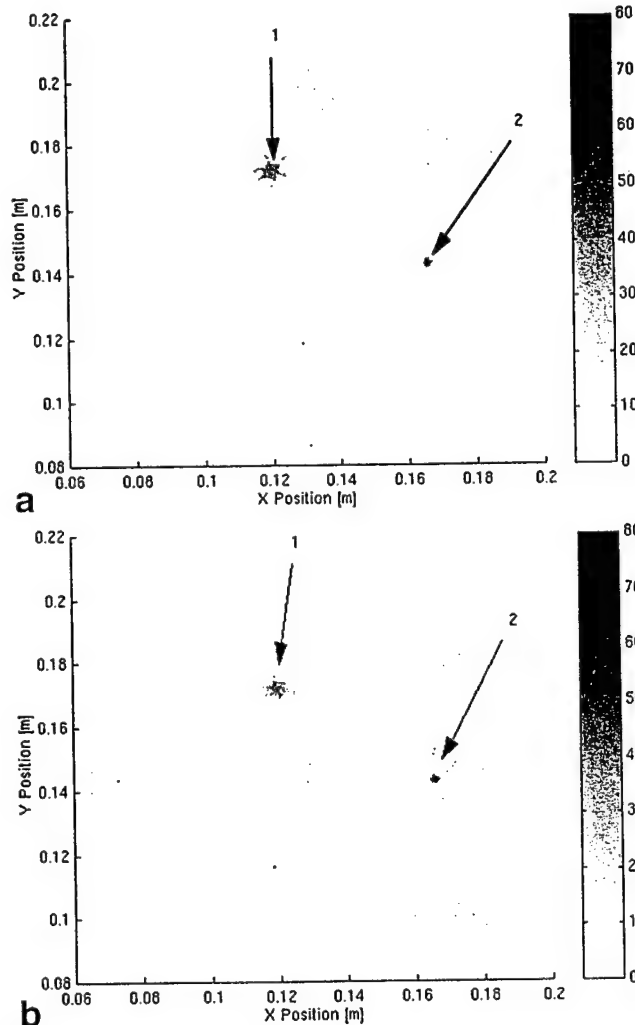


FIG. 5. Brain elasticity problem consisting of a property distribution derived from white/gray matter segmentation of a coronal MR image. **a:** Exact Young's modulus distribution (kPa) of the white/gray matter background with two artificially placed stiff anomalies designated as objects 1 and 2. **b:** Reconstructed Young's modulus distribution (kPa) in the presence of 15% measurement noise.

8000 Pa was used (33), representing the white matter, while the gray matter was assumed to be twice as stiff. The larger inclusion (designated as object 1 in Fig. 5a) measures approximately 1 cm and was assigned a stiffness five times that of the white matter, whereas the smaller inclusion (designated as object 2 in Fig. 5a) is roughly 4 mm in diameter and was specified as being an order of magnitude stiffer than white matter. The inversion process was completed in six global sweeps of 1240 subzones on average, with approximately 164 elements and 100 nodes in each zone. Figure 5b shows the recovered property distribution in the presence of 15% added noise; which compares very favorably with the exact distribution contained in Fig. 5a. A small degree of spatial filtering was found to be helpful in achieving a convergent solution in this case of high noise (34). This technique works to average the local property value at node i with the values at its immediately adjacent nodes so that $E_i^{\text{new}} = (1 - \theta)E_i^{\text{old}} + \theta/N_i \sum_{j=1}^{N_i} E_j^{\text{old}}$, where N_i is the number of neighbor nodes connected to

node i . For the inversion shown in Fig. 5b, a value of 0.2 was used for θ . Note that no spatial filtering was used (i.e., $\theta = 0$) during the inversion shown in Fig. 4d.

CONCLUSIONS

The image reconstructions presented in Figs. 4 and 5 show that the zoned inversion scheme is able to generate accurate Young's modulus distribution images on the basis of displacement information obtained in the presence of high noise (up to 15%). The zoned inversion method also allows for a high degree of parameter discretization, taking full advantage of the data-rich nature of an MR displacement image. This high resolution allowed the inversion routine to discern hard inclusions as small as 4 mm in diameter during simulation. Although there are additional complexities associated with the inversion of actual MR data, these promising simulation results suggest that the subzone technique should provide a powerful framework for recovering elasticity distributions with MR elastography. Specifically, it provides a computationally viable approach that capitalizes on the MR measurement density to yield high-resolution (pixel-level) tissue property maps. The complex nature of the displacement fields that develop in soft tissue makes an imaging algorithm that exploits modeling concepts essential. Use of the finite element method allows the incorporation of tissue mechanics into the analysis of measured displacement patterns so that the complicated waveforms inherent in multidimensional elastic systems may be taken into account.

The finite element inversion process also provides some important avenues for dealing with noisy data and more complicated physical models. The iterative inversion scheme detailed here is amenable to a total variation minimization process, which can be useful in reducing the effects of noise degradation (35). Work is also under way to incorporate a Maxwellian damping term into the inversion process so that tissue-damping effects can be both accounted for and measured in the same manner that Young's modulus is recovered with the algorithm detailed here. Furthermore, the process should be adaptable to modeling transient motion rather than using a steady-state assumption if steady-state data sets cannot be obtained from the MR. In summary, this zoned finite element inversion technique provides a powerful method for deriving highly resolved Young's modulus distribution information in a way that is robust in the presence of high noise and adaptable to a variety of modifications that could improve its performance in the future.

APPENDIX

Here we describe the finite element formulation of the forward and inverse problems in more detail. The governing equation of linear elasticity, Eq. [6a], is cast in terms of the Cauchy stress tensor, \mathcal{T} , which leads more readily to the 2D plane stress or plane strain conditions assumed for the forward and inverse solutions presented.

The Forward Problem

If steady-state harmonic motion is assumed, the real valued displacement vector solution can be represented as the real part of a complex-valued, spatially varying displacement phasor multiplied by the complex exponential

$$u(x, y, t) = \text{Re}[\bar{u}(x, y)e^{i\omega t}], \quad [8]$$

where spatial coordinates x and y and complex displacement components u and v define

$$\bar{u}(x, y) = \begin{Bmatrix} u \\ v \end{Bmatrix}. \quad [9]$$

In stress tensor notation, the harmonic equilibrium condition will then be (36)

$$\nabla \cdot \mathcal{T} = -\rho\omega^2 \bar{u} + \mathbf{F}, \quad [10]$$

making use of the complex harmonic inertia, $\rho\partial^2 u/\partial t^2 = -\rho\omega^2 \bar{u}e^{i\omega t}$, and including any additional body forces \mathbf{F} that may be present. The stress tensor \mathcal{T} can be defined as

$$\begin{aligned} \mathcal{T} &= \hat{\mathbf{i}}\tau_x + \hat{\mathbf{j}}\tau_y + \hat{\mathbf{k}}\tau_z \\ \tau_x &= \hat{\mathbf{i}}\sigma_x + \hat{\mathbf{j}}\tau_{xy} + \hat{\mathbf{k}}\tau_{xz} \\ \tau_y &= \hat{\mathbf{i}}\tau_{yx} + \hat{\mathbf{j}}\sigma_y + \hat{\mathbf{k}}\tau_{yz} \\ \tau_z &= \hat{\mathbf{i}}\tau_{zx} + \hat{\mathbf{j}}\tau_{zy} + \hat{\mathbf{k}}\sigma_z, \end{aligned}$$

and for 2D plane strain or plane stress assumptions the stress-strain relations for elastic solids can be written in the matrix form

$$\begin{Bmatrix} \sigma_x \\ \sigma_y \\ \tau_{xy} \end{Bmatrix} = E \cdot \mathcal{L}_1 \begin{bmatrix} 1 & \mathcal{L}_2 & 0 \\ \mathcal{L}_2 & 1 & 0 \\ 0 & 0 & \mathcal{L}_1 \end{bmatrix} \begin{Bmatrix} \frac{\partial u}{\partial x} \\ \frac{\partial v}{\partial y} \\ \frac{\partial u}{\partial y} + \frac{\partial v}{\partial x} \end{Bmatrix}, \quad [11]$$

with

$$\mathcal{L}_1 = \frac{1-\nu}{(1+\nu)(1-2\nu)} \text{ (plane strain) or } \frac{1}{1-\nu^2} \text{ (plane stress)}$$

$$\mathcal{L}_2 = \frac{\nu}{1-\nu} \text{ (plane strain) or } \nu \text{ (plane stress)}$$

$$\mathcal{L}_3 = \frac{1}{2(1+\nu)},$$

where E is Young's modulus.

To facilitate the solution of this set of equations for complicated geometries containing realistic property distributions, a finite element discretization method is adopted where \hat{u} , the approximate solution to the displacement magnitude \bar{u} , is expanded on a set of locally active, spatially varying Lagrangian basis functions, ϕ_j , so that

$$\hat{u} = \sum_{j=1}^N u_j \phi_j, \text{ and } \hat{v} = \sum_{j=1}^N v_j \phi_j, \quad [12]$$

where u_j and v_j are the approximate x and y directed displacements at the j th of N nodes. Developing a Galerkin weak form of Eq. [10] generates the system of equations

$$[\mathbf{A}] \begin{Bmatrix} \hat{u} \\ \hat{v} \end{Bmatrix} = [\mathbf{b}], \quad [13]$$

with matrix $[\mathbf{A}]$ consisting of the subelements

$$[a_{ij}] = \begin{bmatrix} \alpha_{11} & \alpha_{12} \\ \alpha_{21} & \alpha_{22} \end{bmatrix} \quad [14]$$

where

$$\begin{aligned} \alpha_{11} &= \left\langle \frac{\partial \phi_i}{\partial x} \frac{\partial \phi_j}{\partial x} E \cdot \mathcal{L}_1 + \frac{\partial \phi_i}{\partial y} \frac{\partial \phi_j}{\partial y} E \cdot \mathcal{L}_3 - \rho\omega^2 \phi_i \phi_j \right\rangle \\ \alpha_{12} &= \left\langle \frac{\partial \phi_i}{\partial x} \frac{\partial \phi_j}{\partial y} E \cdot \mathcal{L}_1 \mathcal{L}_2 + \frac{\partial \phi_i}{\partial y} \frac{\partial \phi_j}{\partial x} E \cdot \mathcal{L}_3 \right\rangle \\ \alpha_{21} &= \left\langle \frac{\partial \phi_i}{\partial y} \frac{\partial \phi_j}{\partial x} E \cdot \mathcal{L}_1 \mathcal{L}_2 + \frac{\partial \phi_i}{\partial x} \frac{\partial \phi_j}{\partial y} E \cdot \mathcal{L}_3 \right\rangle \\ \alpha_{22} &= \left\langle \frac{\partial \phi_i}{\partial y} \frac{\partial \phi_j}{\partial y} E \cdot \mathcal{L}_1 + \frac{\partial \phi_i}{\partial x} \frac{\partial \phi_j}{\partial x} E \cdot \mathcal{L}_3 - \rho\omega^2 \phi_i \phi_j \right\rangle, \end{aligned}$$

and the column vectors of unknown nodal displacements and right-hand-side forcing being written as

$$\begin{Bmatrix} \hat{u} \\ \hat{v} \end{Bmatrix} = [\hat{\mathbf{u}}] = [\hat{u}_1, \hat{v}_1, \hat{u}_2, \hat{v}_2, \dots, \hat{u}_N, \hat{v}_N]^T, \quad [15]$$

and

$$b_i = \begin{Bmatrix} \hat{\mathbf{x}} \cdot [\phi_i \mathcal{T} \cdot \hat{\mathbf{n}} \phi_i ds - \langle \mathbf{F} \phi_i \rangle] \\ \hat{\mathbf{y}} \cdot [\phi_i \mathcal{T} \cdot \hat{\mathbf{n}} \phi_i ds - \langle \mathbf{F} \phi_i \rangle] \end{Bmatrix} \quad [16]$$

for i and j running from 1 to N .

The Inverse Problem

For the inversion problem, the basis set used to expand the parameterized elasticity solution is taken to be the same finite element basis set used to expand the displacement solution \hat{u} . The calculation of the $\partial \mathbf{u} / \partial E$ terms needed to generate the Hessian matrix and the right-hand-side vector \mathbf{f} in Eq. [5b] is then achieved directly by the differentiation of Eq. [13], the discretized version of Eq. [10], with respect

to E , leading to

$$\frac{\partial \hat{\mathbf{u}}}{\partial E_k} = -[\mathbf{A}]^{-1} \frac{\partial \mathbf{A}}{\partial E_k} \cdot \hat{\mathbf{u}}, \quad [17]$$

where $\partial \mathbf{A} / \partial E_k$ has terms

$$\left[\frac{\partial a_{i,j}}{\partial E_k} \right] = \begin{bmatrix} \frac{\partial \alpha_{11}}{\partial E_k} & \frac{\partial \alpha_{12}}{\partial E_k} \\ \frac{\partial \alpha_{21}}{\partial E_k} & \frac{\partial \alpha_{22}}{\partial E_k} \end{bmatrix} \quad [18]$$

with

$$\frac{\partial \alpha_{11}}{\partial E_k} = \left(\frac{\partial \phi_i}{\partial x} \frac{\partial \phi_j}{\partial x} \phi_k \zeta_1 + \frac{\partial \phi_i}{\partial y} \frac{\partial \phi_j}{\partial y} \phi_k \zeta_2 \right)$$

$$\frac{\partial \alpha_{12}}{\partial E_k} = \left(\frac{\partial \phi_i}{\partial x} \frac{\partial \phi_j}{\partial y} \phi_k \zeta_1 \zeta_2 + \frac{\partial \phi_i}{\partial y} \frac{\partial \phi_j}{\partial x} \phi_k \zeta_2 \right)$$

$$\frac{\partial \alpha_{21}}{\partial E_k} = \left(\frac{\partial \phi_i}{\partial y} \frac{\partial \phi_j}{\partial x} \phi_k \zeta_1 \zeta_2 + \frac{\partial \phi_i}{\partial x} \frac{\partial \phi_j}{\partial y} \phi_k \zeta_2 \right)$$

$$\frac{\partial \alpha_{22}}{\partial E_k} = \left(\frac{\partial \phi_i}{\partial y} \frac{\partial \phi_j}{\partial y} \phi_k \zeta_1 + \frac{\partial \phi_i}{\partial x} \frac{\partial \phi_j}{\partial x} \phi_k \zeta_2 \right)$$

REFERENCES

- Parker KJ, Gao L, Lerner RM, Levinson SF. Techniques for elastic imaging: a review. *IEEE Eng Med Biol Mag* 1996;15:52-59.
- Muthupillai R, Rosman PJ, Greenleaf JF, Manduca A, Ehman RL. Magnetic resonance elastography by direct visualization of propagating acoustic strain waves. *Science* 1995;269:1854-1857.
- Davies BL, Harris SJ, Lin WJ, Hibberd RD, Middleton R, Cobb JC. Active compliance in robotic surgery: the use of force control as a dynamic constraint. *Proc Inst Mech Eng [H]* 1997;211:285-292.
- Delp SL, Stulberg SD, Davies B, Picard F, Leitner F. Computer assisted knee replacement. *Clin Orthop Rel Res* 1998;354:49-56.
- Miga MI, Paulsen KD, Hoopes PJ, Kennedy FE, Hartov A, Roberts DW. *In-vivo* quantification of a homogeneous brain deformation model for updating preoperative images during surgery. *IEEE Trans Biomed Eng* 1999, in press.
- Paulsen KD, Miga MI, Kennedy FE, Hoopes PJ, Hartov A, Roberts DW. A computational model for tracking subsurface tissue deformation during stereotactic neurosurgery. *IEEE Trans Biomed Eng* 1999;46:213-225.
- Roberts DW, Miga MI, Hartov A, Eisner S, Lemory J, Kennedy FE, Paulsen KD. Intraoperatively updated neuroimaging using brain modeling and sparse data. *Neurosurgery* 1999, in press.
- Fung YC. *Biomechanics: mechanical properties of living tissues*, 2nd ed. New York: Springer-Verlag; 1993.
- Park JB. *Biomaterials science and engineering*. New York: Plenum; 1984.
- Céspedes I, Ophir J, Ponnekanti H, Maklad N. Elastography: elasticity imaging using ultrasound with application to muscle and breast *in-vivo*. *Ultrason Imaging* 1993;15:73-88.
- Gao L, Parker KJ, Alam SK, Lerner RM. Sonoelasticity imaging: theory and experimental verification. *J Acoust Soc Am* 1995;97:3875-3886.
- Kallel F, Ophir J. A least-squares strain estimator for elastography. *Ultrason Imaging* 1997;19:195-208.
- Lerner RM, Huang SR, Parker KJ. "Sonoelasticity" images derived from ultrasound signals in mechanically vibrated tissues. *Ultrasound Med Biol* 1990;16:231-239.
- Nicholas D, Nassiri DK, Garbutt P, Hill CR. Tissue characterization from ultrasound B-scan data. *Ultrasound Med Biol* 1986;12:135-143.
- Ophir J, Céspedes I, Ponnekanti H, Yazdi Y, Li X. Elastography: a quantitative method for imaging the elasticity of biological tissues. *Ultrason Imaging* 1991;13:111-134.
- Yamakoshi Y, Sato J, Sato T. Ultrasonic imaging of internal vibration of soft tissue under forced vibration. *IEEE Trans Ultrason Ferroelectrics Frequency Control* 1990;37:45-53.
- Gao L, Alam SK, Parker KJ. A new vibration theory for sonoelasticity imaging. In: *Proceedings of the IEEE Ultrasonics Symposium*, Baltimore, 1993, p. 879-882.
- Kallel F, Bertrand M. Tissue elasticity reconstruction using linear perturbation method. *IEEE Trans Med Imaging* 1996;15:299-313.
- Skovoroda AR, Emelianov SY, Lubinski MA, Sarvazyan AP, O'Donnell M. Theoretical analysis and verification of ultrasound displacement and strain imaging. *IEEE Trans Ultrason Ferroelectrics Frequency Control* 1994;41:302-313.
- Bishop J, Poole G, Leitch M, Plewes DB. Magnetic resonance imaging of shear wave propagation in excised tissue. *J Magn Reson Imaging* 1998;8:1257-1265.
- Lowa CJ. Magnetic resonance imaging in the presence of mechanical waves. *Spectrosc Lett* 1991;24:55-67.
- Muthupillai R, Rosman PJ, Lomas DJ, Greenleaf JF, Riederer SJ, Ehman RL. Magnetic resonance imaging of transverse acoustic strain waves. *Magn Reson Med* 1996;36:266-274.
- Chenevert TL, Skovoroda AR, O'Donnell M, Emelianov SY. Elasticity reconstructive imaging by means of stimulated echo MRI. *Magn Reson Med* 1998;39:482-490.
- Raghavan KR, Yagle AE. Forward and inverse problems in elasticity imaging of soft tissues. *IEEE Trans Nucl Sci* 1994;41:1639-1648.
- Lewa CJ, De Certaines JD. Viscoelastic property detection by elastic displacement NMR measurements. *J Magn Reson Imaging* 1996;6:652-656.
- Manduca A, Muthupillai R, Rosman PJ, Greenleaf JF, Ehman RL. Image processing for magnetic resonance elastography. *SPIE* 1996;2710:616-623.
- Sumi C, Nakayama K. A robust numerical solution to reconstruct a globally relative shear modulus distribution from strain measurements. *IEEE Trans Med Imaging* 1998;17:419-428.
- Paulsen KD, Moskowitz MJ, Ryan TP. Temperature field estimation using electrical impedance profiling methods. I. Reconstruction algorithm and simulated results. *Int J Hyperthermia* 1994;10:209-228.
- Paulsen KD, Jiang H. Spatially varying optical property reconstruction using a finite element diffusion equation approximation. *Med Phys* 1995;22:691-701.
- Paulsen KD, Jiang H. An enhanced electrical impedance imaging algorithm for hyperthermia applications. *Int J Hyperthermia* 1997;13:459-480.
- Press WH, Flannery BP, Teukolsky SA, Vetterling WT. *Numerical recipes: the art of scientific computing*. New York: Cambridge University Press, 1986. Section 14.4.
- Marquardt DW. An algorithm for least-squares estimation of nonlinear parameters. *SIAM J Appl Math* 1963;11:431-441.
- Nagashima T, Shirakuni T, Rapoport SI. A two-dimensional, finite element analysis of vasogenic brain edema. *Neurol Med Chir (Tokyo)* 1990;30:1-9.
- Jiang H, Paulsen KD, Osterberg UL, Pogue BW, Patterson MS. Optical image reconstruction using frequency domain data: simulations and experiments. *J Opt Soc Am A* 1996;13:253-266.
- Paulsen KD, Jiang H. Enhanced frequency-domain optical image reconstruction in tissues through total-variation minimization. *Appl Opt* 1996;35:3447-3458.
- Chou PC, Pagano NJ. *Elasticity: Tensor, Dyadic and Engineering Approaches*. New York: Dover Publications; 1967.

Elasticity reconstruction from experimental MR displacement data: initial experience with an overlapping subzone finite element inversion process

E. E. W. Van Houten

Thayer School of Engineering, Dartmouth College, Hanover, New Hampshire 03755

J. B. Weaver

Department of Radiology, Dartmouth Hitchcock Medical Center, Lebanon, New Hampshire 03766

M. I. Miga and F. E. Kennedy

Thayer School of Engineering, Dartmouth College, Hanover, New Hampshire 03755

K. D. Paulsen

*Thayer School of Engineering, Dartmouth College, Hanover, New Hampshire 03755,
and Norris Cotton Cancer Center, Lebanon, New Hampshire 03766*

(Received 6 May 1999; accepted for publication 22 October 1999)

The determination of the elastic property distribution in heterogeneous gel samples with a finite element based reconstruction scheme is considered. The algorithm operates on small overlapping subzones of the total field to allow for a high degree of spatial discretization while maintaining computational tractability. By including a Maxwellian-type viscoelastic property in the model physics and optimizing the spatial distribution of this property in the same manner as elasticity, a Young's modulus image is obtained which reasonably reflects the true distribution within the gel. However, the image lacks the clarity and accuracy expected based on simulation experience. Preliminary investigations suggest that transient effects in the data are the cause of a significant mismatch between the inversion model, which assumes steady-state conditions, and the actual displacements as measured by a phase contrast MR technique. © 2000 American Association of Physicists in Medicine.[S0094-2405(00)01901-5]

Key words: MR elastography, experimental elasticity reconstruction, viscoelastic tissue behavior, finite element inversion techniques

I. INTRODUCTION

Interest in accurate, quantitative evaluation of the physical properties of biological tissue is rapidly increasing as the value of this information has been appreciated in such applications as lesion detection, medical examination, and computer assisted surgical procedures. One particular area of interest includes the assessment of the elastic properties of tissue through the analysis of noninvasive image-based, strain measurements. Ultrasound elastography has been studied for some time,¹⁻⁸ where ultrasonic imaging is used to detect subsurface displacement response to an externally applied displacement source. While ultrasound elastography continues to hold promise in terms of providing valuable tissue data, it is presently limited by the lack of lateral resolution in ultrasonic imaging compared to other available modalities. This potential drawback has led to the investigation of MR-based strain imaging techniques.⁹⁻¹⁴ In addition to fully three-dimensional imaging capabilities, MR offers higher resolution than ultrasound, making it a very appealing method for discerning micron level displacement fields in biological structures.

Regardless of the strain imaging technique, it is generally agreed that some type of model-based reconstruction procedure is required for determination of elastic property distributions.^{15,16} To date these models have varied widely in complexity, from simple algorithms relating a Local Fre-

quency Estimation (LFE) to stiffness via a standard wave equation formulation¹⁷ to nonlinear inversion schemes which operate on a partial differential equation (PDE).^{3,18-22} While many of the methods proposed to date have shown promise in simulation, there has been limited success in producing accurate inversions of measured dynamic strain data. This points to a variety of issues, such as viscoelastic behavior and transient effects, which need investigation in order to develop successful, robust algorithms for elasticity imaging through interpretation of harmonic displacement fields.

While inversion in the case of dynamic, rather than quasi-static, mechanical motion has shown the need for a high level of algorithmic sophistication, the benefits of the procedure are potentially significant. By generating strain fields through dynamic displacement propagation, elasticity information can be inferred in structures inaccessible by means of quasi-static surface actuation, e.g., the brain. In addition, dynamic displacements are useful for estimating tissue properties other than elasticity, such as dispersion and density. This paper examines the first applications of a subzone-based elastic property reconstruction scheme,²⁰ with an additional Maxwellian-type viscoelastic term, to experimental MR data. This algorithm is based on a well-established nonlinear inversion scheme,^{3,18,19} where the global reconstruction technique is instead performed on small, local "subzones" of the tissue region of interest (ROI). The improvements in algo-

rhythmic performance found through the addition of viscoelastic behavior are encouraging but not complete. Evidence presented here suggests that the method's assumption of steady-state motion in the MR generated data may be the primary discrepancy in the data-model match.

II. INVERSION METHOD

The nonlinear elastic property reconstruction scheme that forms the core of the subzone inversion technique is centered around a squared error minimization formulation,^{3,18-20} where the agreement between the calculated displacements derived from the most recent property estimate, u_l^c at location l , and the measured displacement data at that location, u_l^m , is sensed by the functional

$$F = \sum_{l=1}^N (u_l^m - u_l^c)^2, \quad (1)$$

for N measurement locations. Minimization of this functional is accomplished by equating its derivatives with respect to the reconstruction parameters to zero, generating the matrix system

$$[(H + \alpha I)]\{\Delta \Gamma\} - \{f\} = 0, \quad (2)$$

with $\Delta \Gamma$ representing the vector of parameter updates, f being the derivatives of F in Eq. (1) with respect to the parameter field Γ , and H being the approximate Hessian matrix. The regularization parameter α is added to the diagonal of H and scaled to the inversion problem at hand by the Levenberg-Marquardt method²³ to facilitate solution of Eq. (2).

Two elastodynamic models have been implemented to date in order to provide displacement calculations based on the estimated parameter distributions. The simplest involves an undamped linear elastic relationship, while the other adds a Maxwellian viscoelastic coefficient to account for the attenuation of displacement in tissue. Expressed in terms of a PDE in displacement, u , these models can be written as²⁴

$$\nabla \cdot G \nabla u + \nabla(\lambda + G) \nabla \cdot u = \rho \frac{\partial^2 u}{\partial t^2}, \quad (3)$$

for a linear elastic tissue of density ρ having properties G and λ and

$$\nabla \cdot G \nabla u + \nabla(\lambda + G) \nabla \cdot u = \zeta \frac{\partial u}{\partial t} + \rho \frac{\partial^2 u}{\partial t^2}, \quad (4)$$

for a Maxwellian viscoelastic material with damping coefficient ζ .

In general, the inversion problem defined in Eq. (2) is intractable for highly resolved material property distributions as computing a single solution update scales cubically with the size of the vector Γ . To overcome this resolution limitation, a subzone inversion scheme has been developed²⁰ which recasts the global error functional in Eq. (1) as a sum of functionals defined on small subzones of the total ROI,

$$F = \sum_{z=1}^Q F_z. \quad (5)$$

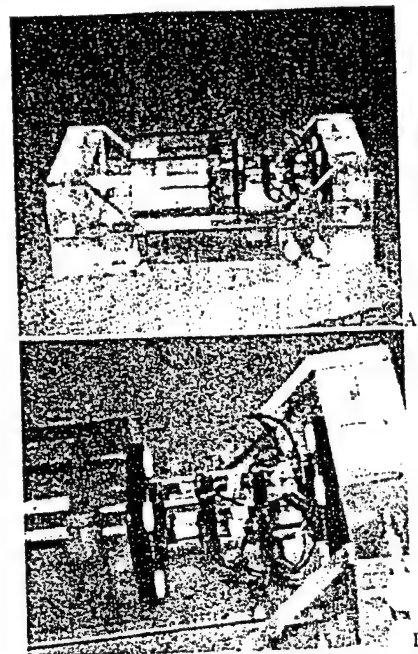


FIG. 1. Piezoelectric displacement actuator with image A showing the entire device including the phantom box on the left and image B showing a close up of the nine parallel driven piezoelectric stacks attached to one wall of the rigid phantom container. The imparted motion is parallel to the long axis of the piezoelectric actuator which is denoted as the x direction in subsequent figures.

where $\min(F)$ is replaced by

$$\sum_{z=1}^Q \min(F_z) \quad (6)$$

for Q subzones. Further details on the mathematical and computational underpinnings of this technique are described in Ref. 20; the algorithm essentially relying on foundations previously developed in Refs. 18, 19. In numerical simulations the formulation has been found to be very effective in reconstructing high resolution (MR pixel level) parameter distributions even in the presence of high noise (up to 15% in the undamped linear elastic case), as reported in Ref. 20. The subzone-based inversion method has also been found to execute relatively quickly, with global property distribution solutions for meshes of approximately 20 000 nodes being completed in a few hours. Direct solution of the full inverse problem for a mesh of this size is computationally infeasible on workstations currently available. Here, we describe our initial experience in applying the algorithm to dynamic MR displacement data measured in gel phantoms.

III. MR DISPLACEMENT IMAGING TECHNIQUE

To obtain displacement measurements, we have developed an MR-compatible mechanical driver which can vibrate tissue-like gel phantoms in a strong magnetic field. Figure 1 shows the device which is currently in use. The design is centered around an actuator constructed of nine piezoelectric stacks wired in parallel. Three layers, each separated by stabilizing ceramic plates and consisting of three piezostacks,

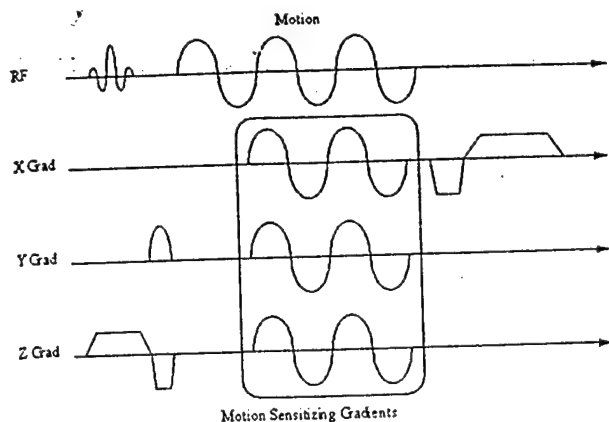


FIG. 2. MR motion sensitizing gradient sequence showing that the duration of mechanical motion is directly linked to the data acquisition time associated with one phase encoding event.

were used to provide adequate displacement under dynamic load. Individually, each stack is capable of $\pm 7 \mu\text{m}$ of displacement when driven by a 100-Vpp signal, so that the assembly as a whole can ideally produce $\pm 21 \mu\text{m}$ of motion. The stacks are powered by a wide band amplifier which boosts the sinusoidal driving signal generated by the MR pulse program. Using the MR pulse sequence to generate the driving signal for mechanical vibration allows almost any waveform to be used and also allows highly accurate control of the phase between the mechanical vibration and the motion encoding gradient. However, this also limits the time of mechanical stimulation to the signal duration of the motion sensitizing gradients as described below (see Fig. 2). Independent measurements of actuator motion using a capacitively coupled displacement probe have demonstrated that the response of the actuators is linear in the applied voltage for a given frequency, yielding 10–15 μm of displacement at 100 Hz, 60 Vpp.

The motion encoding MR gradient sequence, based on a simple gradient echo sequence, is illustrated in Fig. 2. The imaging process involves three cycles of mechanical motion driven by signal from the RF, the last two of which coincide with the sensitizing gradients. The phase in the MR image is recorded for different phase relationships between the applied motion and the encoding gradients to calculate the harmonic displacement in each pixel of an image. Four such phase relationships are used to ensure internal consistency between the measured phase and the fit to the expression $C + M \cos \phi$, where the amplitude, M , and the relative phase, ϕ , completely characterize the harmonic motion. The constant phase offset, C , has no bearing on the measured motion. MR timing and resolution parameters for these image acquisitions are: $TR = 300 \text{ ms}$; $TE = 58 \text{ ms}$; $FOV = 8 \text{ cm}$; 256×128 pixels; 10-mm slice thickness.

IV. EXPERIMENTAL RESULTS

Initially, homogeneous gels were used to validate the MR measurement system. Figure 3 shows a typical example of the displacements obtained in a homogeneous gel phantom ($5 \text{ cm} \times 5 \text{ cm} \times 4 \text{ cm}$), where the 100-Hz, x-directed actuation

was applied through the bottom and two side walls of the rigid gel container (see Fig. 1). The displacements were recorded in both the horizontal (x) and vertical (y) directions such that they form a two component vector field in the imaging plane parallel to the axis of mechanical translation. Because of the symmetry in this case, only a single central plane is illustrated. Distortional (shear) wave fronts are evident with a wavelength of approximately 1 cm. This wavelength is consistent with the known Young's modulus of the gel (3–5 kPa, as measured in separate mechanical tests). Peak displacements measured in the gel at the walls of the box were approximately 10 μm , which mirrors the data collected with an independent measurement probe.

In Fig. 3, the images in the first column represent data collected for x -directed (horizontal) motion while the second column shows the corresponding data for y -directed (vertical) motion. The first row, *A*, shows a standard grayscale MR image of the homogeneous gel phantom, while rows *B* and *C* show the reconstructed motion parameters M and ϕ , respectively. The bottom row, *D*, shows the overall displacement field, given by $M \cos \phi$ for each vector displacement component. It is interesting to note that there is a small discrepancy between these displacement images and the known boundary conditions, i.e., a nonzero displacement along the bottom of the gel phantom. This is due to an imperfection in an early prototype of the mechanical driver, where the horizontal plane of motion did not exactly correspond to the horizontal plane of the MR, leading to a uniform y -directed displacement offset within the gel.

The development of wavelike behavior is readily visible in the magnitude (row *B*) and displacement fields (row *D*) as expected. However, the mechanics of the wave propagation are fairly complex, even for a homogeneous gel phantom as illustrated in Fig. 3, due to the asymmetric (top to bottom) boundary conditions which exist. From the x directional displacement (row *D*, left), it is evident that the predominant mode of wave propagation is shear motion caused by the bottom surface acting as a distortional wave source. The uniform horizontal peaks and valleys suggest the gel is nearly incompressible at this length scale (short compared to the dilatational wavelength) and low frequency, so that dilatational wave propagation is not supported. The same conclusion is reached by examining the y motion in Fig. 3 (row *D*, right) where uniform vertical contours exist, indicating a shear mode of propagation. Another noticeable characteristic is the apparent damping of motion from the walls to the center of the gel (row *B*) suggesting that the wavefronts may have undergone some dispersion or may not represent fully developed harmonic motion.

Figure 4 shows MR generated x and y displacement data for a block of agar gel with a hard, spherical agar gel inclusion approximately 1.5 cm in diameter. The plane shown is the same as Fig. 3, cutting through the center of the phantom with its x -axis in line with the direction of vibration. The y -directed displacement offset associated with Fig. 3 has been removed by the elimination of the imperfection in the mechanical driver. Figure 5 presents a standard grayscale MR image of the gel phantom. Interestingly, the inclusion is

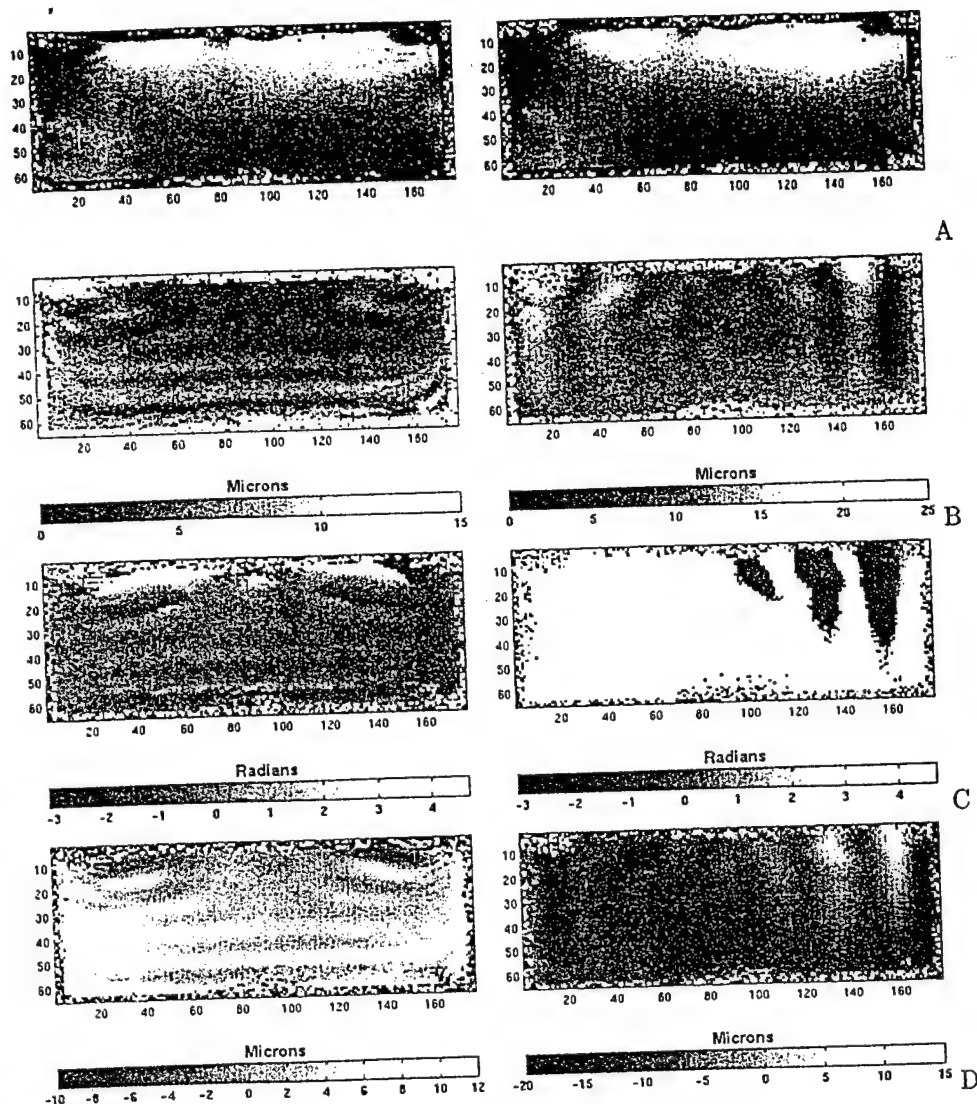


FIG. 3. Raw data from MR motion encoding gradients using a homogeneous gel phantom within the device shown in Fig. 1 with voxel intensity grayscale images (row A), magnitudes of x and y displacement respectively [μm] (row B), phase of x and y directional displacement [rad] (row C), and reconstructed x and y displacement from magnitude and phase [μm] (row D). The left-hand column represents x directed motion sensitivity while the right represents y directed sensitivity. Note that the images in this figure are dimensioned in pixel coordinates.

barely visible in image A, showing that the elastic property contrast does not translate into conventional MR image contrast. It is also the case that the displacement fields themselves (Fig. 4) do not clearly indicate the presence of the harder inclusion embedded within the gel. For visualization purposes, the area of heterogeneity has been outlined in image B of Fig. 5.

Image reconstructions of the elastic property distribution in the heterogeneous gel sample (Fig. 5) obtained from the MR displacement data (Fig. 4) are presented in Fig. 6. Two inversions are shown: one with the undamped elastic model from Eq. (3) (image A) and the other with the damped model presented in Eq. (4) (images B and C), where image B shows the elasticity distribution and image C shows the map of the Maxwellian attenuation coefficient for the damped model reconstruction. While both images A and B clearly recover the presence of a hard inclusion near the center of the gel, the size and overall localization of the inclusion are more accurately represented in the damped model inversion. Image C indicates that the surrounding gel has a relatively low attenu-

ation component while the inclusion exhibits a level of increased damping.

The results in Fig. 6 are encouraging, especially since they represent one of the first elastic property images derived from experimental MR data where displacements have been measured under conditions of a dynamically applied mechanical stimulus. However, further improvements are desirable and necessary if MR elastography is to progress clinically. While qualitatively satisfying, the images in Fig. 6 are not immediately as promising as those achieved in simulation studies,²⁰ which raises important questions about the adequacy of the model relative to the imaging physics. The improvement in the elastic property image with the addition of attenuation effects demonstrated in Fig. 6 suggests that data-model match is critical. In this regard it is important to note that the MR displacement field is acquired during the first three harmonic cycles of the displacement stimulation which is intermittently applied with the pulse sequencing (see Fig. 2) as the data associated with each pixel/voxel is generated. Hence, it is quite possible that the measured dis-

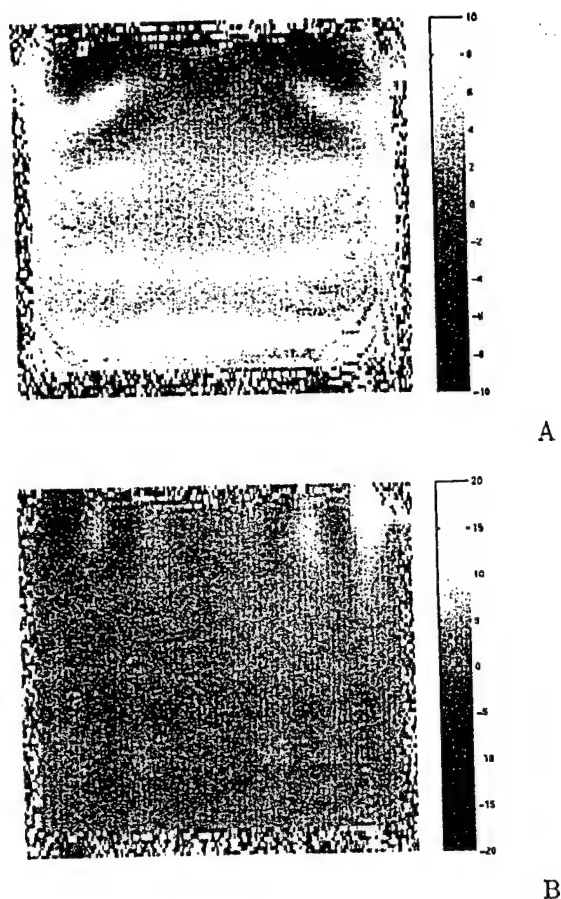


FIG. 4. Displacement data generated by the phase contrast MR imaging method for the gel sample shown in Fig. 5. Image A shows the x direction displacement while image B shows the y direction displacement, both in μm .

placements do not reflect fully developed wavefronts which have reached the dynamic steady state, creating a conflict with the harmonic motion assumption used in the inversion model.

To investigate this possibility, we simulated the transient behavior of the MR data acquisition using a time-domain solution of Eq. (4) where the stimulation was applied to the walls of the phantom for three cycles at 100 Hz. The time history of each node in the finite element mesh which comprises the measured displacement field was then Fourier transformed and the 100-Hz component (magnitude and phase) was extracted in order to represent the MR displacement measurements. This data was then supplied to our frequency domain inversion algorithm (after being corrupted with 10% added noise), which produced the elastic property image shown in image A of Fig. 7. This image is strikingly similar in character to the images in Fig. 6. In image B of Fig. 7, we also show the case where the simulated measurement data is taken from the steady-state solution (with 10% added noise) and inverted with the algorithm. The improvement in the recovery of the elastic property distribution is remarkable and suggests that the degradation of the image in Fig. 6 results in part from data-model mismatch between the transient motion which is measured and the time-harmonic

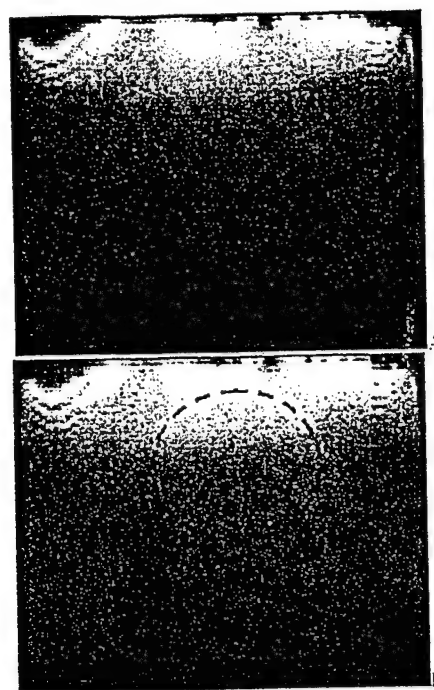


FIG. 5. Standard MR contrast image of a heterogeneous gel sample where image B includes a superimposed outline of the hard inclusion.

model which is assumed. It is also interesting to note that the recovery of the elastic properties is quantitative for the steady-state data image (image B) whereas the reconstructed properties are an order of magnitude too high for the transient data image (image A), presumably due to some form of artificial hardening which tries to compensate for the data-model mismatch. The reconstructions from experimental data in Fig. 6 exhibit the same character (i.e., an effective hardening of the embedded inclusion).

V. CONCLUSIONS

Previous simulations²⁰ indicate that quantitative image reconstruction of elastic property distributions can be recovered in the presence of considerable measurement noise (up to 15%) using an overlapping zone finite element inversion technique. Reconstructed property resolution can be preserved at the MR measurement level (i.e., pixel resolution) with this approach. Initial experience with reconstructions of actual MR data in heterogeneous gel phantoms consisting of harder inclusions embedded in a softer background is encouraging and shows that the localized increase in stiffness can be found (despite a lack of conventional MR image contrast or contrast observable directly in the displacement field itself). In this regard, the incorporation of displacement attenuation through the addition of a Maxwellian viscoelastic term in the governing computational model has been shown to improve the recovery of the size, shape, and location of the hard inclusion. However, simulations of the potential transient effects in the MR displacement measurements indicate that the data-model mismatch between the MR data acquisition method and the assumed steady-state image recon-

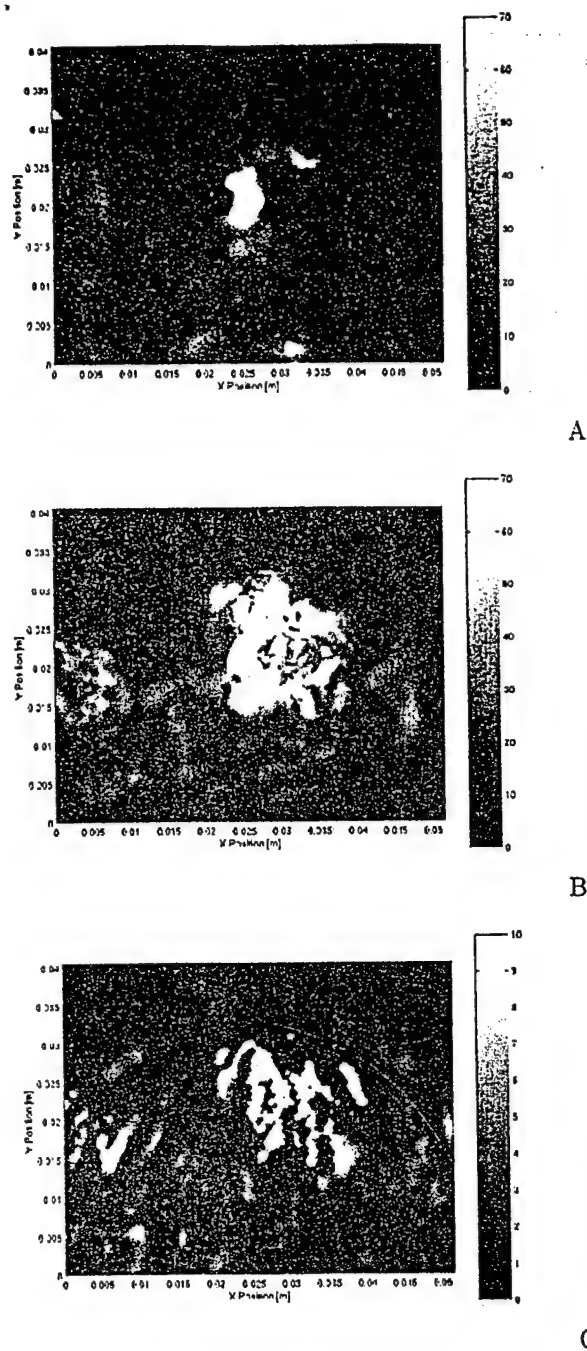


FIG. 6. Two inversions of the MR displacement data shown in Fig. 4. Image A shows the reconstruction based on the undamped linear elastic model in Eq. (3) [kPa] and images B and C show the resulting elasticity (image B) and Maxwellian damping (image C) distributions of the viscoelastic model [Eq. (4)] inversion, in units of [kPa] and [$\text{kg/s } 1e6$], respectively.

struction model may be the most important factor which presently limits the recovered property image quality.

Two immediate pathways for resolving this inconsistency present themselves. As demonstrated in the transient simulation reported here, the MR displacement encoding gradient imaging process can be modeled by taking the frequency component of the transient displacement solution related to the harmonic excitation. By incorporating this process into

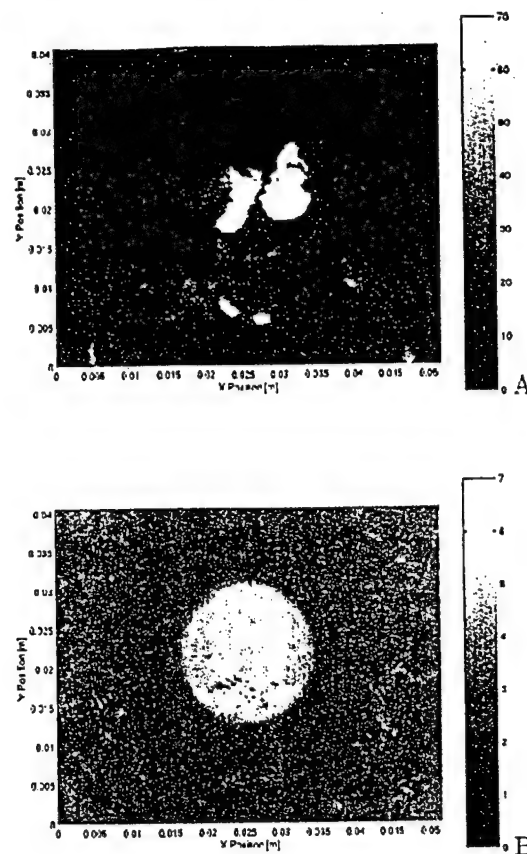


FIG. 7. Two inversions of the simulated data set where image A shows the reconstruction based on displacement data generated in three cycles of motion starting from rest [kPa] while image B shows the same reconstruction process carried out on steady-state data [kPa].

the subzone inversion technique, the transient effects present in displacement images generated in three or four cycles of actuation could be modeled, presumably leading to high quality inversions from transient data sets of this type. Alternatively, by separating the driving signal for the mechanical actuator from the gradient signal, but maintaining phase coherency with the MR gradients through the use of a phase-lock loop, mechanical excitation could be applied throughout the image acquisition process. This would assure that the resulting displacement images represent the steady-state motion of the sample, which should also lead to high quality property reconstructions. Which approach provides the best image reconstructions while still offering a convenient and feasible imaging process remains to be determined. At this point both of the strategies mentioned here remain as viable options.

ACKNOWLEDGMENTS

This work was supported in part by NIH Grant No. R01-NS33900, awarded by the National Institute of Neurological Disorders and Stroke and in part by DOD-AMRD, DAMP 17-96-1-6119.

- ¹I. Céspedes, J. Ophir, H. Ponnekanti, and N. Maklad, "Elastography: Elasticity imaging using ultrasound with application to muscle and breast *In Vivo*," *Ultrason. Imaging* 15, 73–88 (1993).
- ²L. Gao, K. J. Parker, S. K. Alam, and R. M. Lerner, "Sonoelasticity imaging: Theory and experimental verification," *J. Acoust. Soc. Am.* 97, 3875–3886 (1995).
- ³F. Kallel and J. Ophir, "A least-squares strain estimator for elastography," *Ultrason. Imaging* 19, 195–208 (1997).
- ⁴R. M. Lerner, S. R. Huang, and K. J. Parker, "'Sonoelasticity' images derived from ultrasound signals in mechanically vibrated tissues," *Ultrasound Med. Biol.* 16, 231–239 (1990).
- ⁵D. Nicholas, D. K. Nassiri, P. Garbutt, and C. R. Hill, "Tissue characterization from ultrasound B-scan data," *Ultrasound Med. Biol.* 12, 135–143 (1986).
- ⁶J. Ophir, I. Céspedes, H. Ponnekanti, Y. Yazdi, and X. Li, "Elastography: A quantitative method for imaging the elasticity of biological tissues," *Ultrason. Imaging* 13, 111–134 (1991).
- ⁷Y. Yamakoshi, J. Sato, and T. Sato, "Ultrasonic imaging of internal vibration of soft tissue under forced vibration," *IEEE Trans. Ultrason. Ferroelectr. Freq. Control* 37, 45–53 (1990).
- ⁸A. R. Skovoroda, S. Y. Emelianov, M. A. Lubinski, A. P. Sarvazyan, and M. O'Donnell, "Theoretical analysis and verification of ultrasound displacement and strain imaging," *IEEE Trans. Ultrason. Ferroelectr. Freq. Control* 41, 302–313 (1994).
- ⁹J. Bishop, G. Poole, M. Leitch, and D. B. Plewes, "Magnetic resonance imaging of shear wave propagation in excised tissue," *J. Magn. Reson. Imaging* 8, 1257–1265 (1998).
- ¹⁰T. L. Chenevert, S. Y. Emelianov, and A. R. Skovoroda, "Elasticity reconstructive imaging using static displacement and strain estimations," in *Proc. of the Int. Soc. of Magnetic Resonance in Medicine*, 461.
- ¹¹T. L. Chenevert, A. R. Skovoroda, M. O'Donnell, and S. Y. Emelianov, "Elasticity reconstructive imaging by means of stimulated echo MRI," *Magn. Reson. Med.* 39, 482–490 (1998).
- ¹²C. J. Lewa, "Magnetic resonance imaging in the presence of mechanical waves," *Spectrosc. Lett.* 24, 55–67 (1991).
- ¹³R. Muthupillai, P. J. Rossman, D. J. Lomas, J. F. Greenleaf, S. J. Riederer, and R. L. Ehman, "Magnetic resonance imaging of transverse acoustic strain waves," *Magn. Reson. Med.* 36, 266–274 (1996).
- ¹⁴R. Muthupillai, D. J. Lomas, P. J. Rossman, J. F. Greenleaf, A. Manduca, and R. L. Ehman, "Magnetic resonance elastography by direct visualization of propagating acoustic strain waves," *Science* 269, 1854–1857 (1995).
- ¹⁵C. Sumi and K. Nakayama, "A robust numerical solution to reconstruct a globally relative shear modulus distribution from strain measurements," *IEEE Trans. Med. Imaging* 17, 419–428 (1998).
- ¹⁶K. R. Raghavan and A. E. Yagle, "Forward and inverse problems in elasticity imaging of soft tissues," *IEEE Trans. Nucl. Sci.* 41, 1639–1648 (1994).
- ¹⁷A. Manduca, R. Muthupillai, P. J. Rossman, J. F. Greenleaf, and R. L. Ehman, "Image processing for magnetic resonance elastography," *Proc. SPIE* 2710, 616–623 (1996).
- ¹⁸K. D. Paulsen and H. Jiang, "Spatially varying optical property reconstruction using a finite element diffusing equation approximation," *Med. Phys.* 22, 691–701 (1995).
- ¹⁹K. D. Paulsen and H. Jiang, "An enhanced electrical impedance imaging algorithm for hyperthermia applications," *Int. J. Hyperthermia* 13, 459–480 (1997).
- ²⁰E. E. W. Van Houten, K. D. Paulsen, M. I. Miga, F. E. Kennedy, and J. B. Weaver, "An overlapping subzone technique for MR based elastic property reconstruction," *Magn. Reson. Med.* 42, 779–786 (1999).
- ²¹A. Manduca, V. Dutt, D. T. Borup, R. Muthupillai, R. L. Ehman, and J. F. Greenleaf, "Reconstruction of elasticity and attenuation maps in shear wave imaging: An inverse approach," in *Lecture Notes in Computer Science—Medical Image Computing and Computer-Assisted Intervention '98*, edited by W. M. Wells, A. Colchester, and S. Delp (Springer-Verlag, Berlin, 1996), pp. 606–613.
- ²²F. Kallel and M. Bertrand, "Tissue elasticity reconstruction using linear perturbation method," *IEEE Trans. Med. Imaging* 15, 299–313 (1996).
- ²³D. W. Marquardt, "An algorithm for least-squares estimation of nonlinear parameters," *SIAM (Soc. Ind. Appl. Math.) J. Appl. Math.* 11, 431–441 (1963).
- ²⁴P. C. Chou and N. J. Pagano, *Elasticity; Tensor, Dyadic and Engineering Approaches* (Dover, New York, 1967).

Applications of Monotonic Noise Reduction Algorithms in fMRI, Phase Estimation, and Contrast Enhancement

John B. Weaver

Department of Radiology, Dartmouth-Hitchcock Medical Center, Lebanon, NH 03755

ABSTRACT: Noise reduction using monotonic fits between extrema has been shown to work well on images, especially those with very low signal-to-noise ratios (SNRs). In this article we will explore three applications of monotonic noise reduction in magnetic resonance imaging (MRI). The first application is reducing noise in function MRI (fMRI) studies. Reduced noise allows greater flexibility. For example, it allows the activated regions to be identified using noisier images acquired in less time or fewer cycles of stimulation. Activation maps were calculated from the images after noise reduction had been applied to each image in the series. The parameters used in the noise reduction were optimized so the images produced best matched the average of the entire series. The CNR was improved significantly in the activation maps. The results can be extended to any other fMRI paradigm. The second application was reducing noise in complex data to improve the SNR of the phase in the complex MRI image. The error in the phase was reduced by a factor of three in the simulations shown. In the third application, we introduced a simple contrast-enhancement method using monotonic noise reduction. To enhance contrast, the coarse features were reduced in size; the smaller size features were increased in size; very small features that are likely to be noise were attenuated. The result is a simple, effective method of improving the contrast of features of a selected size in images with no false features introduced. © 1999 John Wiley & Sons, Inc. *Int J Imaging Syst Technol*, 10, 177–185, 1999

Key words: noise reduction; fMRI; contrast enhancement; phase estimation

I. INTRODUCTION

Monotonic noise reduction is a relatively new method that is effective at lower signal-to-noise ratios (SNRs) than other methods (Weaver, 1997). It also avoids Gibb's ringing and blurring, two common problems that afflict currently used methods. Noise reduction filters and denoising methods fit many adjacent data points to a set of basis functions. This change of basis allows the parts of the data most likely to be noise to be suppressed. The effectiveness of the particular method depends on how well the basis separates noise from data. In high noise regions, projection onto the basis functions that average large numbers of pixels represents the data most accurately and therefore has the least noise. Representing the data with only those basis functions leads directly to bandlimiting loss of spatial resolution and undersampling artifacts. Monotonic noise

reduction does not fit the data with a limited set of basis functions, so no undersampling or ringing artifacts are introduced and there is no bandlimiting. It simply constrains the data to be monotonic between extrema.

A. Monotonic Noise Reduction in One Dimension. Monotonic noise reduction is simplest in one dimension. An elegant algorithm (Demetriou, 1990; Demetriou and Powell, 1991) that produces the monotonically increasing series that fits a data set best in a least-squares sense is used. The algorithm travels through the data until it finds a decrease. A decrease violates the monotonic condition. When it finds a decrease, the algorithm averages that decreasing data point with as many previous points as is necessary to establish monotonic increase. The algorithm then continues the process by searching for the next decrease. When all of the decreases are averaged away, the algorithm is completed.

The primary advantage of this algorithm for noise reduction is that it smooths the data as little as possible and does not blur edges. The algorithm leaves all increases unchanged; both sharp and smooth increases remain unchanged so no smoothing occurs at all. The algorithm averages just as many data points as necessary to get a monotonically increasing series so the data are smoothed as little as possible.

However, not all signals are monotonically increasing functions. A monotonically decreasing series can be easily obtained with the same algorithm by reversing the order of the data or by subtracting the data from some large constant. The algorithm can also be used to produce a piecewise monotonic series by breaking the data into regions between extrema that are each fit to increasing or decreasing monotonic series.

The key to fitting piecewise monotonic series is to identify the extrema correctly. In this sense, monotonic noise reduction is very similar to wavelet denoising. The key in both cases is in identifying the extrema. In wavelet denoising, extrema in the gradient are required and in monotonic noise reduction the signal peaks are required. To select significant extrema, we have used a Fourier filter to smooth small extrema away. Then only extrema that are different from previous and subsequent extrema by more than a user-defined threshold are used. There are two parameters that the user must set to find the extrema: the bandwidth allowed through the Fourier filter and the minimum difference between extrema that is allowed. When the extrema are found, noise can be suppressed by forcing monotonic change between the extrema. The algorithm in one dimension is shown in Figure 1.

Contract grant sponsor: DOD-AMRD

Contract grant sponsor: DAMD; Contract grant number: 17-96-1-6119

Contract grant sponsor: NIH; Contract grant number: H133G70031-98

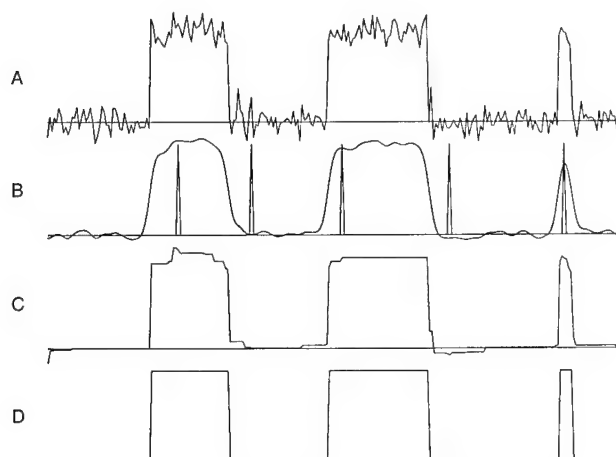


Figure 1. The one-dimensional monotonic noise-reduction algorithm. (Top to bottom) The original signal, the signal plus added noise, the blurred signal with the selected extrema shown as vertical lines, and the results of monotonic noise reduction. The SNR is 10; the standard deviation of the noise is one tenth and the peak signal is one so the total signal energy is less than 10 times the total noise energy.

B. Monotonic Noise Reduction in Two Dimensions. The extension of the algorithm to multiple dimensions is accomplished by ordering the pixels in the image into a one-dimensional series where the one-dimensional algorithm can be used. In previous versions of this algorithm, the one-dimensional algorithm was run on the rows and then the columns of rotated versions of the image (Weaver, 1997b). As many rotations as needed were used. However, most of the noise is eliminated using just four angles. Therefore, a faster version of the algorithm that uses the one-dimensional algorithm on the rows, columns, and diagonals of the image is used here. Figures 2 and 3 illustrate the steps used in the algorithm. No interpolation is required to rotate the image to other angles, which speeds up the algorithm significantly. This version of the algorithm was used in all of the applications presented here. This algorithm was coded in Matlab® with two subroutines coded in C. It runs in 10–20 s on a 256×256 -pixel image on a DEC Alpha®. Earlier versions of the algorithm required 2–3 min. In both cases, the time required depends on the number of extrema identified. More extrema increases the run time. Interactive languages like Matlab® are significantly slower than Fortran or C, so execution times could be reduced significantly.

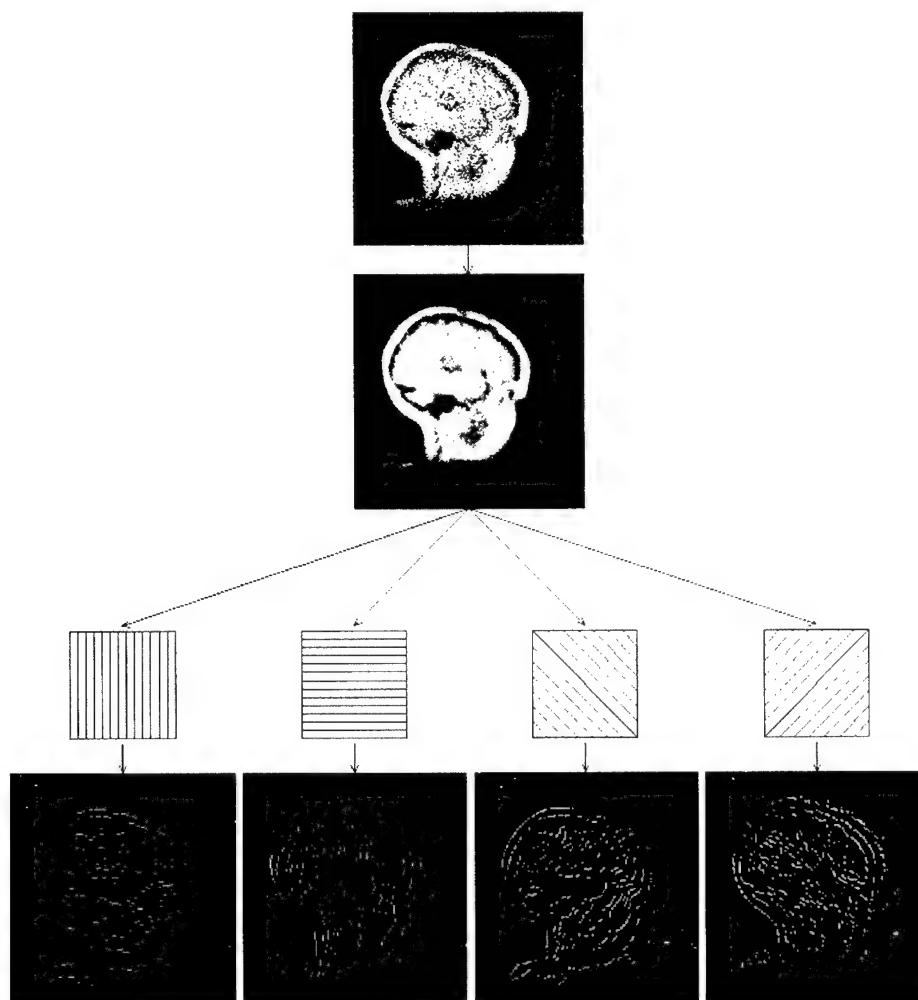


Figure 2. The selection of extrema in the two-dimensional monotonic noise reduction algorithm. The top image is the original image with significant noise. The Fourier blurred image is shown below the original image. The extrema are selected along the columns, rows, and both diagonals of the two-dimensionally blurred image. The four images at the bottom show the position of the selected extrema for all four directions.

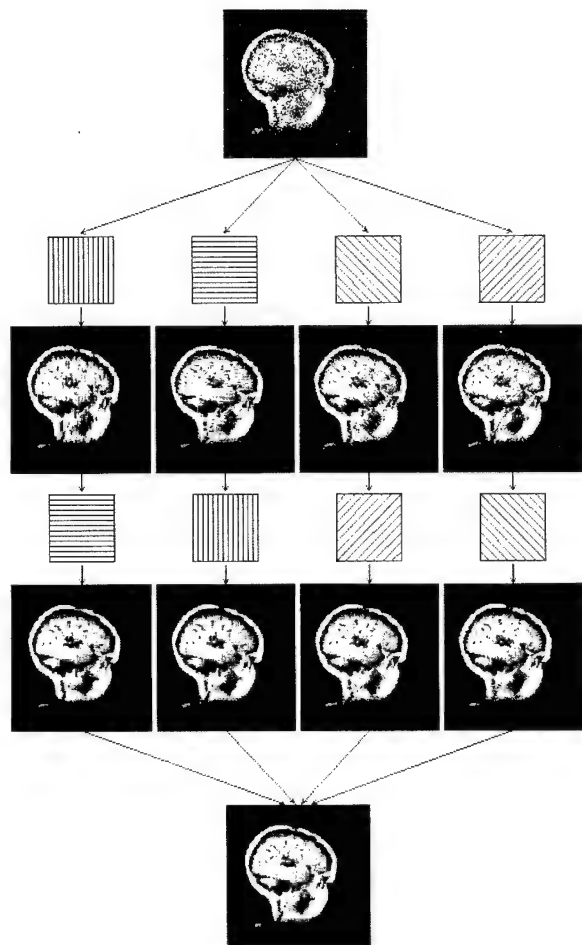


Figure 3. Application of the one-dimensional algorithm in the two dimensional monotonic noise-reduction algorithm. The pixels between extrema along the columns are made monotonic. The rows of the processed image are then processed using the one-dimensional algorithm. This forms one intermediate image. Processing the rows and then the columns forms another intermediate image. Processing the upper left to lower right diagonal followed by the lower left to upper right diagonal forms another intermediate image. Processing the lower left to upper right diagonal followed by the upper left to lower right diagonal forms the last intermediate image. All four intermediate images are averaged together to form the final processed image.

II. REDUCING NOISE IN FMRI ACTIVATION MAPS

In functional magnetic resonance imaging (fMRI), multiple serial images of the same anatomy are obtained during a series of mental tasks (Frank et al., 1998; Jezzard and Song, 1996; Turner, 1997; Weisskoff, 1995). Small changes in the signal of brain tissue reflect the small blood flow changes and oxygenation levels that are associated with activation. At 1.5 T the changes in signal are around 3% (Turner et al., 1993), which is the same size as the random noise in good-quality images. Therefore, only changes that are correlated with the mental tasks over many task cycles signify activation. Noise in the images limits fMRI studies in several ways. The images are generally low resolution to obtain sufficient SNR to detect the activations. As much imaging time as possible is used to obtain the required SNR. Reducing the imaging time would reduce the SNR, but it would mitigate several other problems. It might be possible to

reduce artifacts and it would allow more flexibility in task design. Many mental tasks are difficult to turn on and off consistently over several cycles. For example, memory tasks are difficult to turn off because it is difficult to stop thinking about something. Distraction can be effective but is not consistent and distraction introduces other activations. On the other hand, many activations are difficult to maintain in a controlled manner. Concentration can wander to the noise of the scanner or other unintended subjects very easily. Therefore, reducing the sensitivity to noise is important. We have used monotonic noise reduction to eliminate some of the random noise in the images so the activation-related signal changes are more easily identified from noisier images that can take less time to acquire.

A. Methods. We used the monotonic noise reduction algorithm described above on each image in an fMRI motor activation study. The unusual aspect of filtering fMRI images is that they are all nearly identical so the average image is an excellent, low-noise estimate of each individual image. We used the average image to estimate the best parameters to use in the noise reduction algorithm. The parameters that made one of the images in the middle of the series most like the average image were used. The Nelder-Mead-type simplex search method implemented in Matlab® was used to find the optimum parameters for the monotonic noise-reduction method. Then, each image in the series was processed using the same parameters. Simple *z*-scores of the images were used to form the activation map.

We used a simple motor activation study that clearly showed both right- and left-hand activation. We then added normally distributed random noise to the images. The activation maps were calculated with and without monotonic noise reduction. The average *z*-scores in the activated regions and in the background brain were calculated to evaluate how well the activation could be identified. The activated regions were those that had a *z*-score above 3 in the original activation maps. The background region was the entire brain except rectangular regions centered on the right and left activations. The activation maps were calculated with nine amounts of added noise. The standard deviation of the noise ranged from 0% to 25% of the maximum signal in the image. The noise energy added ranged from 0% of the total image energy to 93% of the total image energy.

The motor study we used is a simple one that is used in a laboratory exercise for engineering students. Although the study design is old, the random noise is representative of almost any fMRI study. Therefore, the noise reduction shown using this study is representative of noise reduction using other fMRI studies. The study was performed on a 1.5-T General Electric Signa system with 10 mT/m gradients. A single axial plane 4 cm below the apex of the cranium was imaged. Six cycles of rest and motor activation were obtained. Each cycle of images consisted of five resting images followed by five images taken during tapping of the right hand followed by five images taken during tapping of the left hand. Each image was a 256×256 , 24-cm field of view, gradient-echo image with a TR of 70 ms and TE of 40 ms. The images were strongly T2* weighted. *z*-scores for each pixel were used to identify activated regions. The standard deviation of the 90 images was used as a measure of the total variation in signal. To obtain the signal correlated with right hand finger tapping, the average of the rest and left hand tapping was subtracted from the average of the right hand finger tapping. The activation map for the right hand motor task was the ratio of the signal correlated with right hand finger tapping over the total variation in signal. Similarly, the activation map for the left hand motor task was the ratio of the signal correlated with left hand

Right Activation Maps
Original Images

Left Activation Maps
Original Images

Right Activation Maps
with Noise Reduction

Left Activation Maps
with Noise Reduction

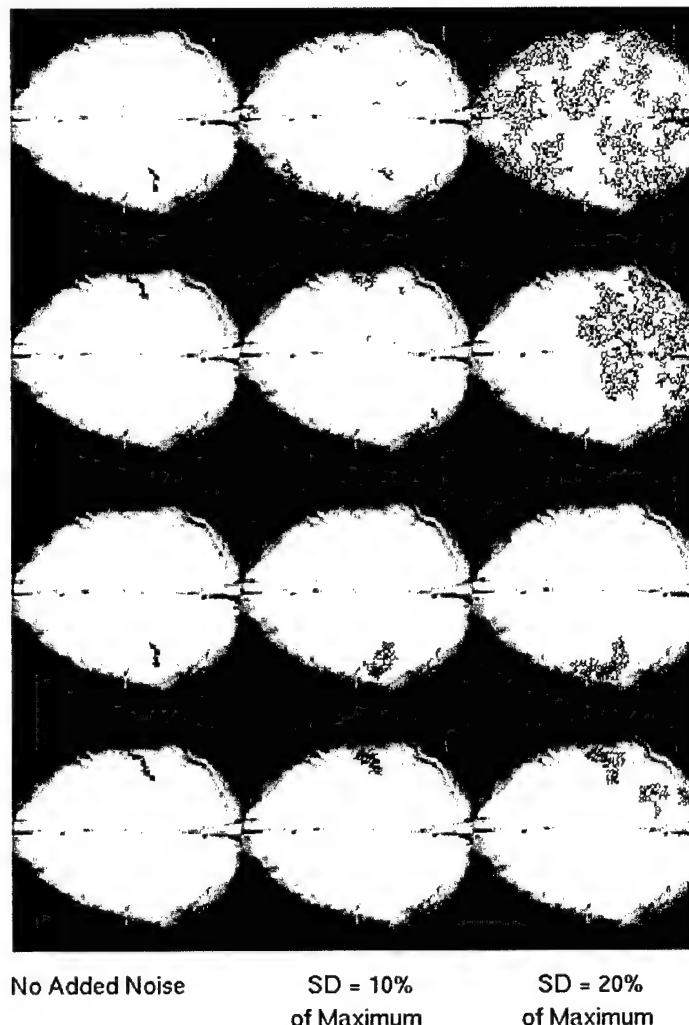


Figure 4. The activation maps for left and right motor activity obtained from six cycles of a simple motor task. The maps in each column were obtained from the original data with different amounts of added noise. Ten percent added noise means that the standard deviation of the random noise is 10% of the maximum pixel intensity in the average image. The top row are the activation maps for the right hand task. The second row are the activation maps for the left hand task. The third and fourth rows are the activation maps for the right hand and left hand, respectively, when monotonic noise reduction is applied to the raw images before the z-scores are calculated. False activations appear in both right and left maps with 10% noise when noise reduction is not used. Monotonic noise reduction allows the activations to be identified when as much as 20% added noise; in this case, the noise energy is essentially half of the total energy in the image. The regions identified were those with at least one pixel with the maximum value in the true activated region. All pixels in the region were above the mean z-score in the true activated region. This method ensured that the true activated region was identified, but it shows how unique that region is.

finger tapping over the total variation in signal. The images were aligned using a multiscale, rigid alignment method developed by Unser et al. (1993) and Kostelec et al. (1998). Alignment did not change the results dramatically.

B. Results. The z-score maps calculated from the original images were used as the true position of the motor strips. The first column of Figure 4 shows the activation maps obtained from all six cycles of the right- and left-hand motor task both with and without noise reduction. When the standard deviation of the added noise was 10% of the maximum signal value, spurious activations were seen in the right and left unfiltered maps. There were no spurious activations when noise reduction was used. When the standard deviation of the added noise was 20% of the maximum signal value, the spurious activations eliminated all possibility of identifying the correct acti-

vated regions when noise reduction was not used. There were no spurious activations in the right-hand activation map when noise reduction was used, and few in the left. The size of the activated regions increased when noise reduction was used because the cutoffs used to identify the activation were set by the unprocessed maps.

Figures 5 and 6 show the mean z-scores in the activated regions and in the background for right- and left-hand tasks, respectively. using monotonic noise reduction increased the z-score in the activated region by as much as 128% for the right-hand task and 143% for the left-hand task. The average increase was 66% for the right-hand task and 75% for the left-hand task. The average z-scores in the background region remained essentially unchanged.

Noise reduction algorithms were only effective for random noise. Systematic sources of noise such as patient motion or the cerebrospinal fluid (CSF) moving cannot be reduced with these methods.

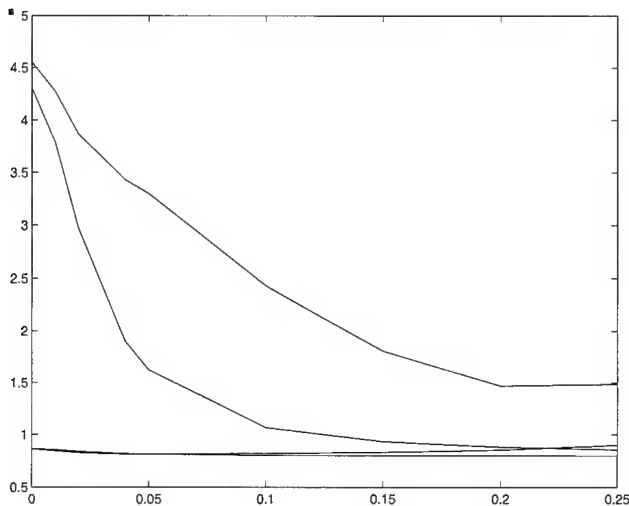


Figure 5. The mean z-scores of pixels in the region activated during right-hand activity as a function of added noise. (Top curve) When noise reduction is used. (Middle curve) When the original images were used. The two curves along the bottom are the mean z-scores in the background region. The background did not change significantly. The background is the entire brain excluding a rectangular region around the right and left hand activated regions. Noise reduction increased the mean z-score by as much as 128%.

However, the methods of image acquisition might be changed to speed up imaging or synchronize it with the other sources of physiologic noise even at the expense of increased random noise if noise reduction is employed. Random noise reduction is a useful tool that can be used to improve fMRI studies when the random noise masks the real activations.

III. PHASE RECOVERY

There are many applications where the phase of the MR signal encodes important information. For example, the phase can be used to generate frequency maps. Frequency maps might be useful in fMRI to separate the effects of large-scale susceptibility changes caused by larger vessels from intravoxel susceptibility changes caused by changes in capillary blood flow. The phase can also be used to encode velocity information in phase-contrast imaging (Moran, 1982; Van Dijk, 1984). In elastography (Muthupillai and Ehman, 1996; Plewes et al., 1995; Chenevert et al., 1998), the phase encodes the displacement of tissue produced by low-frequency vibrations. In many of these cases, these measurements have relatively low SNRs because they must be obtained with fast imaging methods.

Both the real and imaginary parts of the complex image are distorted by additive normally distributed random noise. The noise becomes Rician only after the magnitude is taken (Macovski, 1996). The real and imaginary parts of the signal can be filtered separately with no added bias because the noise is independent. The uncertainty in the phase angle at each pixel still depends on the magnitude of the signal, but reduced noise decreases that uncertainty.

It is not uncommon to repetitively scan of the same physical position. In elasticity measurements using phase-contrast estimates of periodic motion, three scans can be taken to measure displacement in all three directions. The magnitude of the image is identical in all three scans; only the phase changes. Again as in the fMRI

experiment, the average provides a good estimate of each image so we can use the same method of finding the optimum parameters for the monotonic noise reduction algorithm.

A. Methods. Noise in the real and imaginary parts of the signal is suppressed separately using monotonic noise reduction. The phase is calculated from the resulting complex signal.

A one-dimensional simulation has been used to demonstrate the potential. The phase varied linearly from π to $-\pi$ across the signal. The total signal energy over the total noise energy is 0.38. The standard deviation of the noise in both the real and imaginary channels is 0.25 and the peak signal is one.

For the two-dimensional case, it was assumed that the magnitude of the image was known. In that case, the average can be used to find the optimum parameters in the filtration. The threshold and bandwidth used to find the extrema were selected to minimize the difference between the magnitude of the filtered image and the magnitude of the average image. The Nelder-Mead type simplex search method implemented in Matlab® was used to find the optimum parameters for the monotonic noise reduction method. For demonstration, we assumed that the magnitude was a clinical axial image. The phase was simulated with a quadratic polynomial. Normally distributed random noise was added to both images to disturb the phase and magnitude of the image.

B. Results. The one-dimensional signal is shown in Figure 7. The standard deviation of the error in phase was reduced from 31 degrees in the original noisy data to seven degrees following monotonic noise reduction.

The two dimensional results also depend on the initial SNR in the complex data. Figure 8 shows the phase of the original image, the noisy image and the results of noise reduction. The mean error in the phase was decreased by a factor of almost three from 58 degrees to 21 degrees.

IV. CONTRAST ENHANCEMENT

Contrast enhancement can be extremely useful in a wide variety of applications. It can be used to improve the conspicuity of low-

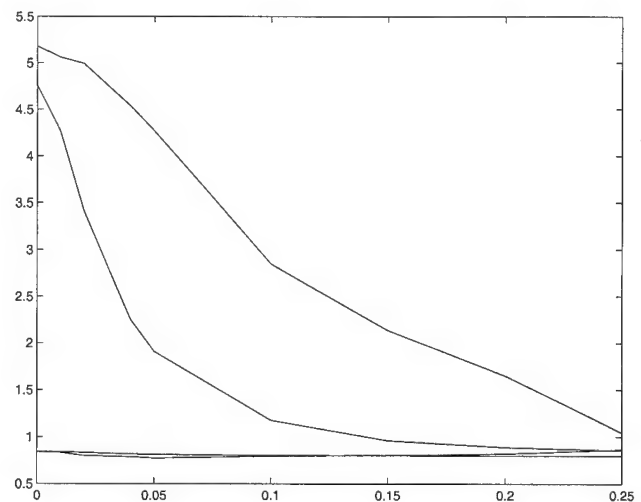


Figure 6. The mean z-scores of pixels in the region activated during left-hand activity as a function of added noise. The order of curves is the same as in Figure 5. Noise reduction increased the mean z-score by as much as 143%.

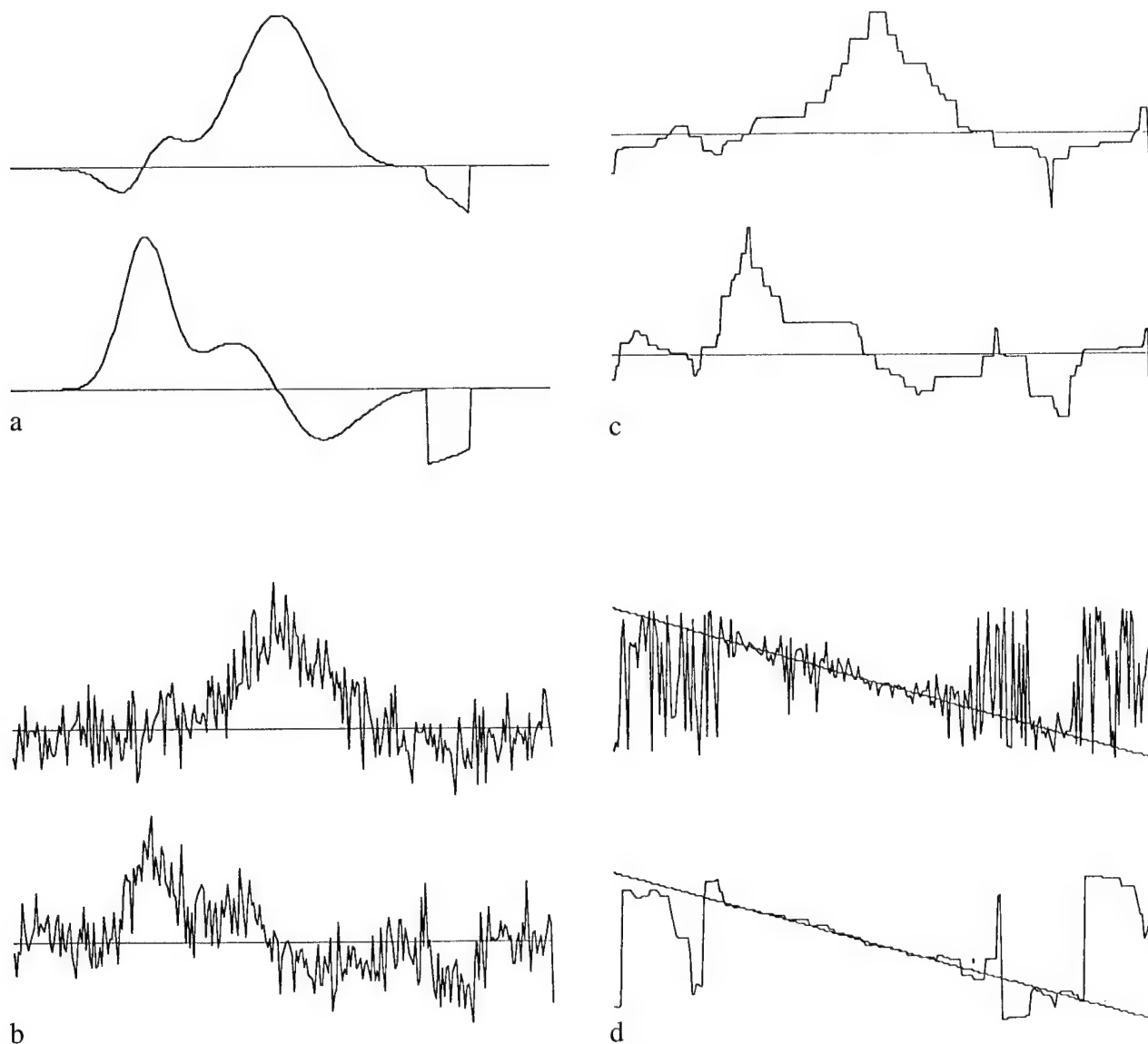


Figure 7. (a) The real and imaginary parts of the simulated signal. (b) The signal with added noise. (c) The signal recovered from the noisy data using monotonic noise reduction. (d) The top plot is the phase of the unprocessed signal plotted with the true phase. The bottom shows the phase recovered from monotonic noise reduction compared to the original phase is shown on the bottom. The noise is very accurately recovered in regions where the signal is large enough. In regions where the signal is almost zero, the phase is not accurate.

contrast features making them harder to overlook. Contrast enhancement has been used in mammography to make lesions more prominent (Lu et al., 1994; Li et al., 1997). Contrast enhancement can be used on digitized chest images (Rehm et al., 1990; Souto et al., 1992; McNitt-Gray et al., 1993) and routine bone images (Ogoda et al., 1997), or it could be used in radiation therapy to improve the contrast of port films.

Contrast enhancement can be accomplished with histogram modification (Gonzalez and Wintz, 1977) or edge-based techniques (Beghdadi and LeNegrate, 1989; Neycensac, 1993). Histogram equalization performs poorly with large uniform regions. Several edge-based methods (Barrett and Swindell, 1981) can be reduced to variations of the blurred-mask algorithm (Bednarek and Rubin, 1991; Jain, 1989). Blurred-mask or unsharp-mask methods can be used to amplify different size features by different amounts. Other

techniques that use the wavelet transform can amplify features of different sizes by different amounts as well (Lu et al., 1994b). We have used monotonic noise suppression in a blurred-mask method to enhance contrast. The primary advantages of the monotonic method are that it works well at lower SNRs, is not bandlimited, and does not introduce ringing in the image. Ringing produced by undersampling can be amplified and introduce false lesions. Unsharp-mask methods also allow the basic intensity distribution to remain similar, so the look and feel of the contrast-enhanced image are the same as those of the original image.

A. Methods. We used monotonic noise reduction in a variation of the blurred-mask method to enhance contrast. Two filtered images, I_1 and I_2 , are obtained using the standard noise-reduction algorithm. The more heavily filtered image, I_2 , is used to reduce the baseline

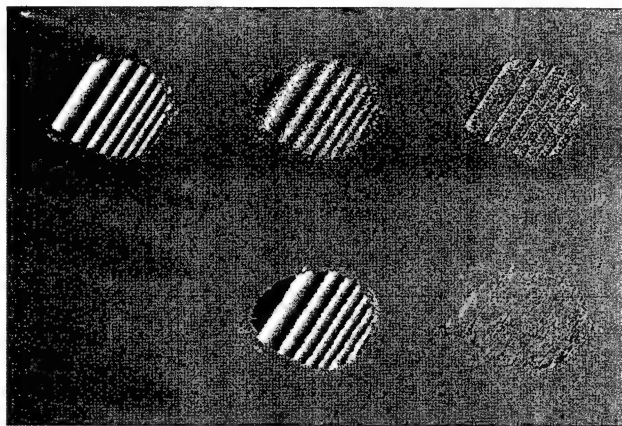


Figure 8. The phase of the noiseless complex image is the upper right image. The other two images in the top row are the phase of the noisy image and phase error in the noisy image. The two images in the bottom row are the phase of the monotonically noise suppressed image and the phase error. The noise in the monotonically noise suppressed image is reduced significantly. The error in the phase is improved by a factor of almost three, from 58 degrees in the noisy image to 21 degrees in the monotonically noise suppressed image.

variations in the image. The details to be enhanced are left in the first image, I_1 , and filtered out of the second image, I_2 . Those details are found by subtracting I_2 from I_1 . However, the general brightness pattern of the image needs to be maintained so the details are amplified and added to I_1 :

$$I_{ce} = I_1 + a(I_1 - I_2)$$

where a is the factor used to vary the contrast enhancement. Factors of 10–15 are commonly used in our experience.

Features of different sizes can be amplified by different amounts if multiple filtered images are obtained. Let I_1, I_2, \dots, I_n be a series

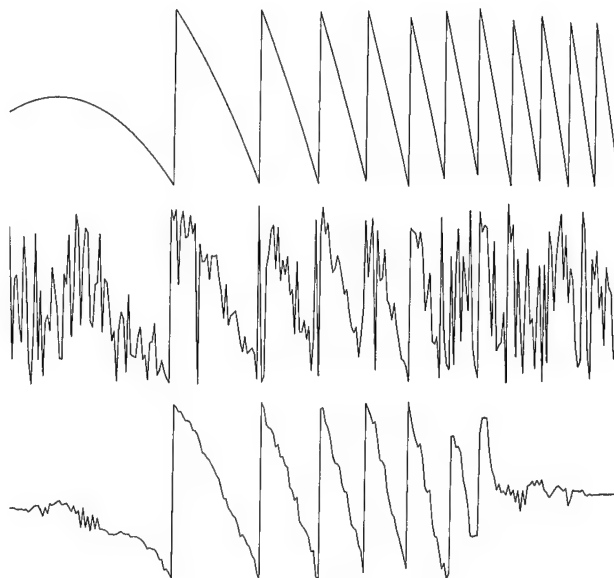


Figure 9. The top curve is the phase of the 128th row of the noiseless image shown in Figure 8. The middle row is the phase of the 128th row of the noisy image. The bottom row is the phase of the 128th row of the monotonically noise suppressed image.

of filtered images obtained using increasingly large thresholds so each image has fewer small features than previous ones. Subtracting pairs of adjacent images can separate the features of each size range. Each subtracted pair can be amplified by any desired amount in the contrast-enhanced image:

$$I_{ce} = I_1 + \sum_{i=1}^{n-1} a_i(I_i - I_{i+1})$$

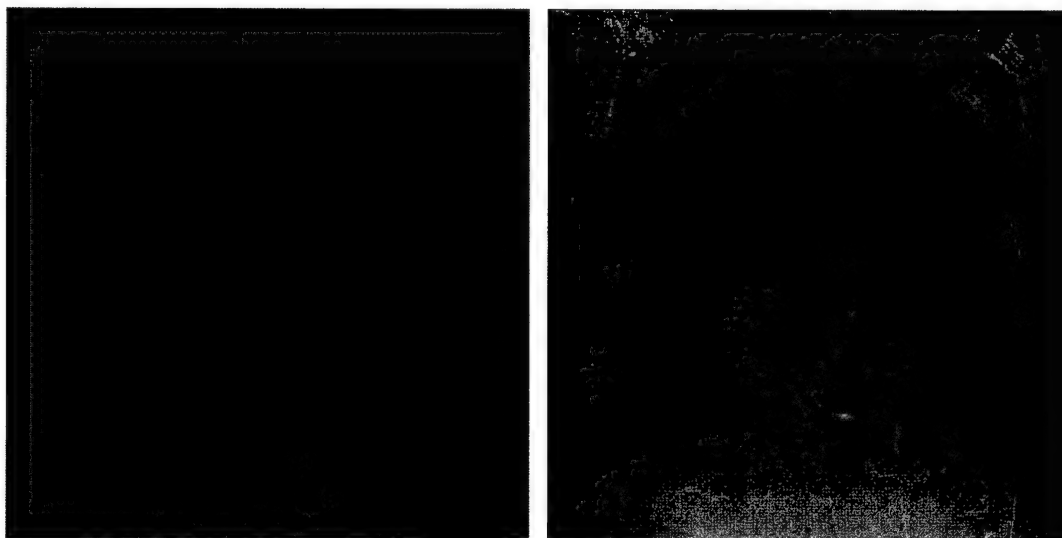


Figure 10. Original chest image is shown on the left and the contrast enhanced image is shown on the right. The image was enhanced to visualize the vessels in the lung and the pacemaker leads. The vessels in the lung and the sharp outlines of the vertebrae in the mediastinum are all much more clearly visible in the contrast-enhanced image. The leads are visible in the lung and as they cross the mediastinum.

B. Results. We enhanced the contrast in a digitized chest image to improve the conspicuity of the vessels in the lung and the pacemaker lines. The original and contrast enhanced images are shown in Figure 10. It is clear that the vessels are well depicted and there are no spurious signals. The vertebrae and the ribs are also seen much more clearly in the contrast-enhanced image.

We also enhanced the contrast in a mammogram. Both the original image and the contrast enhanced image are shown in Figure 11. The vessels throughout the breast are much more clearly depicted. A plot of the 150th column of both images is shown in Figure 12. The plot allows the reader to match features in the original image with features in the contrast-enhanced image. No extra peaks were introduced by the contrast enhancement, and the general intensity distribution of the image was maintained.

V. CONCLUSIONS

Monotonic noise reduction is useful in situations where noise is large, and it is especially useful when significant information about the extrema exists. We have shown three examples of the utility of monotonic noise reduction. Suppressing noise prior to calculating the z-scores significantly enhances fMRI activation maps. The CNR can be more than doubled. The average image provides an effective way to estimate the optimum parameters for the noise-reduction algorithm. The phase error can be improved significantly by filtering both real and imaginary parts of the reconstructed image before calculating the phase. If only the phase changes between multiple measurements of the same physical region, the accurate estimate of the magnitude of the image can be used to improve the estimate of the phase even more. Finally, a simple robust method of contrast enhancement using monotonic noise reduction was shown to be effective in maintaining the general appearance of the image while improving contrast significantly. There are many improvements that can be made to the algorithm. Methods of reducing the noise leakage

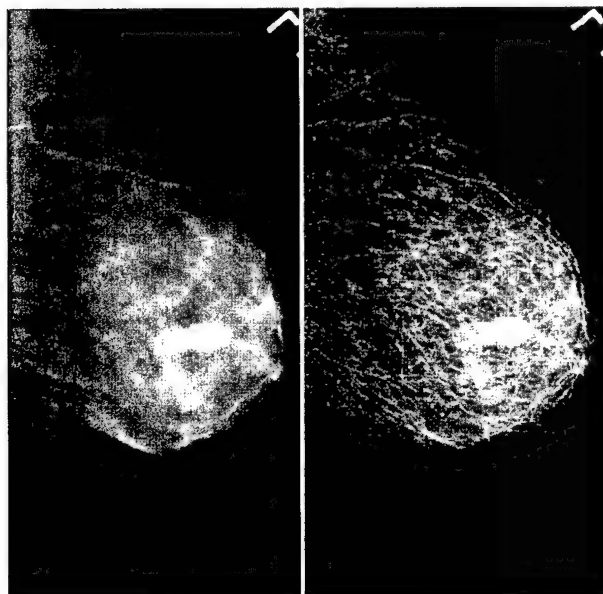


Figure 11. A mammogram is shown on the left and the contrast enhanced mammogram is shown on the right. The vessels and ducts are much more clearly delineated.

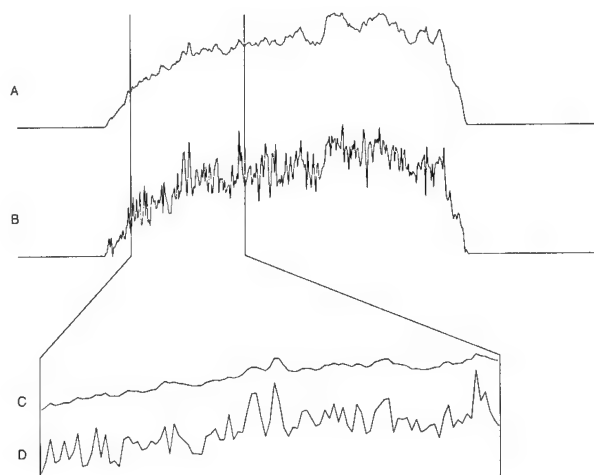


Figure 12. Plot comparing of the 150th column of the original and contrast enhanced breast images. (A) The original image. (B) The contrast enhanced image. (C) Rows 100–200 of the original image in greater detail. (D) Rows 100–200 of the contrast enhanced image for comparison. The general intensity distribution is maintained. The expanded views show that each peak in the contrast enhanced image corresponds to a peak in the original image. There are no new peaks and the position of the peaks remains the same. No spurious features are introduced and there is no ringing to interfere with the vessels.

at boundaries are particularly promising. There are also many variations of the basic method that can be made to adapt it to specific situations.

REFERENCES

- H.H. Barrett and W. Swindell, Radiological imaging, Academic Press, New York, 1981.
- D.R. Bednarek and S. Rudin, Blurred-mask density compression for improved reproduction of radiographs, *Radiology* 26 (1991), 358–363.
- A. Beghdadi and A. LeNegrate, Contrast enhancement technique based on local detection of edges, *Comput Vision Graph Images Process* 46 (1989), 162–174.
- T.L. Chenevert, A.R. Skovoroda, M. O'Donnell, and S.Y. Emelianov, Elasticity reconstructive imaging by means of stimulated echo MRI, *Magn Reson Med* 39 (1998), 482–490.
- I.C. Demetriou, A characterization theorem for the discrete best monotonic approximation problem, *Math Comput* 55 (1990), 191–195.
- I.C. Demetriou and M.J.D. Powell, Least squares smoothing of univariate data to achieve piecewise monotonicity, *IMA J Numer Anal* 11 (1991), 411–432.
- L.R. Frank, R.B. Buxton, and E.C. Wong, Probabilistic analysis of functional magnetic resonance imaging data, *Magn Reson Med* 39 (1998), 132–48.
- R.C. Gonzalez and P. Wintz, Digital image processing, Addison-Wesley, Reading, MA, 1977.
- A.K. Jain, Fundamentals of digital signal processing, Prentice-Hall, Englewood Cliffs, NJ, 1989.
- P. Jezzard and A.W. Song, Technical foundations and pitfalls of clinical fMRI, *Neuroimage* 4 (1996), S63–S75.
- P.J. Kostelec, J.B. Weaver, and D.M. Healy, Jr., Multiresolution elastic image registration, *Med Phys* 25 (1998), 1593–1604.
- H. Li, K.J. Liu, and S.C. Lo, Fractal modeling and segmentation for the enhancement of microcalcifications in digital mammograms, *IEEE Trans Med Imaging* 16 (1997), 785–798.

- Jian Lu, D.M. Healy, Jr., and J.B. Weaver, Contrast enhancement of medical images using multiscale edge representation, *Proc SPIE Wavelet Appl* 2242, 1994a, pp. 711–719.
- Jian Lu, D.M. Healy, Jr., and J.B. Weaver, Contrast enhancement of medical images using multiscale edge representation, *Opt Eng* 33 (1994b), 2151–2161.
- A. Macovski, Noise in MRI, *Magn Reson Med* 36 (1996), 494–497.
- M.F. McNitt-Gray, R.K. Taira, S.L. Johnson, and M. Razavi, An automatic method for enhancing the display of different tissue densities in digital chest radiographs, *J Digital Imaging* 6 (1993), 95–104.
- P.R. Moran, A flow velocity zeugmatographic interlace for NMR imaging in humans, *Magn Reson Med* 1 (1982), 197–203.
- R. Muthupillai and R.L. Ehman, Magnetic resonance elastography, *Nat Med* 2 (1996), 601–603.
- F. Neyenssac, Contrast enhancement using the Laplacian-of-a Gaussian filter, *CVGIP Graph Models Image Process* 5 (1993), 447–463.
- M. Ogoda, K. Hishinuma, M. Yamada, and K. Shimura, Unsharp masking technique using multiresolution analysis for computed radiography image enhancement, *J Digital Imaging* 10(Suppl 1) (1997), 185–189.
- D.B. Plewes, I. Betty, S.N. Urchuk, and I. Soutar, Visualizing tissue compliance with MR imaging, *J Magn Reson Imaging* 5 (1995), 733–738.
- K. Rehm, G.W. Seeley, W.J. Dallas, T.W. Ovitt, and J.F. Seeger, Design and testing of artifact-suppressed adaptive histogram equalization: a contrast-enhancement technique for display of digital chest radiographs, *J Thorac Imaging* 5 (1990), 85–91.
- M. Souto, J. Correa, P.G. Tahoces, D. Tucker, K.S. Malagari, J.J. Vidal, and R.G. Fraser, Enhancement of chest images by automatic adaptive spatial filtering, *J Digital Imaging* 5 (1992), 223–229.
- R. Turner, Signal sources in bold contrast fMRI, *Adv Exp Med Biol* 413 (1997), 19–25.
- R. Turner, P. Jezzard, H. Wen, K.K. Kwong, D. Le Bihan, T. Zeffiro, and R.S. Balaban, Functional mapping of the human visual cortex at 4 and 1.5 Tesla using deoxygenation contrast EPI, *Magn Reson Med* 29 (1993), 277–279.
- M. Unser, A. Aldroubi, and C. Gerfen, A multiresolution image registration procedure using spline pyramids, *Proc SPIE, Vol. 2034, Mathematical Imaging: Wavelets and Applications in Signal and Image Processing*, San Diego, 1993, pp. 160–170.
- P. Van Dijk, Direct cardiac NMR imaging of heart wall and blood flow velocity, *J Comput Assist Tomogr* 8 (1984), 429–436.
- J.B. Weaver, Reducing noise in images by forcing monotonic change between extrema, *Int Soc Anal Appl Comput* (1997), 189.
- J.B. Weaver, Removing noise from images: Least squares monotonic functions on line segments through the image, *Proc Soc Magn Reson, Vancouver, Canada, August 1997*, p. 2043.
- R.M. Weisskoff, Functional MRI: Are we all moving towards artifactual conclusions? Or fMRI fact or fancy? *NMR Biomed* 8 (1995), 101–103.

Reducing Noise in Images by Forcing Monotonic Change Between Extrema

John B. Weaver

Department of Radiology, Dartmouth-Hitchcock Medical Center,
Lebanon, N.H. 03755

Supported by a grant from the National Cancer Institute, CA23108 and by a grant from the Department of Defense, DAMD17-96-1-6119. The author takes pleasure in acknowledging his introduction to monotonic fits by Jian Lu and Dennis M. Healy, Jr. The help and ideas of Peter J. Kostelec is also gratefully acknowledged.

Abstract

A novel method of reducing noise in images is presented. The significant extrema (maxima and minima) in the image are selected using a simple low pass Fourier filter. The method forces the pixel values in the image to vary monotonically between the selected extrema. For example, the pixel values in the filtered image should decrease monotonically in all directions from an isolated maximum. Because the algorithm that performs the monotonic fits is one dimensional, we approximate monotonic change in all directions by doing monotonic fits along line segments throughout the image. The filtering operation on each line segment replaces the pixel values on that segment with a monotonic sequence that fits the original pixel values best in a least squares sense. Monotonic change is enforced along line segments in as many directions as desired. The method is simple, reasonably fast and quite stable. Good results can be obtained for images with SNR's as low as 0.5.

Keywords

Noise reduction, Monotonic, Extrema

I. BACKGROUND

There are many methods of removing noise from images. The basic idea is almost always to represent the signal and noise in a basis that separates the true signal from the noise as completely as possible. In Fourier filters, the noise is assumed to be dominant in the high frequencies and the signal dominant in the low frequencies so removing high frequencies removes mostly noise. However, removing or damping the high frequencies produces bandlimited blurring. Wavelet denoising [1, 2, 3, 4, 5, 6] adds another twist by allowing the bandwidth passed to be different at different positions in the image. The high frequencies are allowed to pass where edges have been identified or are likely and the high frequencies are more strongly suppressed where edges are not likely. Edges produce extrema in the wavelet transform domain so a wider bandwidth is passed around large values of the wavelet transform. One of the keys in wavelet denoising is deciding when an edge is present and when the large wavelet response is from noise. An alternative method of preferentially suppressing noise is presented here. Instead of identifying extrema of the derivative as in wavelet denoising, the extrema of the signal itself (peaks) are found; the signal is then forced to change monotonically between the extrema. The method should be more robust than wavelet denoising because averages are more stable than differences. However, identifying the correct extrema is again the key to the performance of the method. The filter is made possible by an elegant algorithm due to Demetriou and Powell that finds the monotonic series that fits data points best in a least squares sense [7]. It basically averages large enough groups of adjacent points in the series to achieve a monotonic progression. Monotonically decreasing series can be found by reversing the order of the data. It is a robust and relatively fast method. Our noise reduction method for images has two parts: selecting the important extrema and forcing monotonic change between those extrema. Extrema selection is best done in two dimensions because extra stability is gained by smoothing in both dimensions rather than only one. The process of forcing monotonic change in all directions is accomplished by forcing monotonic change along many line segments. We will first look at the relevant properties of the algorithm that forces monotonic change along a single line segment. Then we will describe the two dimensional algorithm in detail, show some results, give some applications, and propose future improvements.

II. ONE DIMENSIONAL EXAMPLES

The values of a function at points between two adjacent extrema must vary monotonically essentially by definition. Therefore, a function of one variable in additive noise can be retrieved by identifying the positions of the extrema and fitting the points bounded by each pair of adjacent extrema to a monotonic function. For any segment bounded by a pair of adjacent extrema, the monotonic series that fits the points best in a least squares sense can be found using the Demetriou and Powell algorithm [7]. This algorithm has several very interesting properties. The result is not just a fit to a limited set of basis functions. Any monotonic series can be recovered. The result is not bandlimited; edges are not blurred.

The algorithm takes the first element of the series as the starting value and advances through the series element by element. If an element in the series is smaller than the previous element, the algorithm averages past points in the series to bring the past values down and the present element up enough to maintain monotonic increase. The algorithm is fast, works in place so memory requirements are minimal and is relatively robust. Figures 1 to 4 demonstrates the important properties. Figure 1 shows a simulated signal made up of three boxcars with moderate added noise. The local SNR over the boxcars is approximately ten. The ratio of the total signal energy to the total noise energy is six. This is generally a relatively poor SNR for medical imaging; a good, crisp MR image generally has a SNR of at least 80. The blurred signal and the extrema selected are shown as well as the final noise suppressed signal. Two features of the noise suppressed signal should be noted: the edges are not blurred at all and there are spurious peaks at the boundaries between monotonic segments. Demetriou and Powell's algorithm is very happy with sharp edges; they are not blurred at all. This is obviously very important because edges are among the most important features we use to interpret images. Blurring is also the most limiting property of many noise reduction techniques especially the Fourier based methods. Wavelet based noise suppression methods have been promising largely because they promise to leave edges unblurred. The spurious peaks at the boundaries between monotonic segments are the only deformation of the signal resulting from the noise suppression. It is caused by the lack of averaging at the ends of the segments. A large value caused by noise in the center of the segment will be balanced by random small values on both sides of it while a large value caused by noise at the end of the segment satisfies the monotonic criteria and is not changed. Another way to see the effect is to run the algorithm over a series of random values. Some part of the noise energy is monotonic and it is primarily at the ends of the segment as shown in Figure 5. That monotonic part of the random noise can not be distinguished from real monotonically increasing signal. Figure 2 shows the results at very low SNR's. The noise has a standard deviation of one and the signal peaks have a height of one. The SNR over the peaks is one and the ratio of the total signal energy to the total noise energy is 0.6. The peaks are recovered and the edges are sharp. The leakage of noise at the boundaries between the segments is much more pronounced than at higher SNR, as might be expected. Figure 3 demonstrates the importance of extrema selection. All three peaks were recovered when the thresholds were properly selected. However, if the threshold for extrema selection was too low, too many extrema were selected and extraneous peaks were introduced as in Figure 3B. If the threshold for extrema selection was too high, too few extrema were selected and features with small energy were lost as the 6 pixel wide peak was lost in Figure 3D. As the SNR was reduced to extremely low levels, approximately 0.1, the noise leakage at the boundaries between monotonic segments dominates the result as shown in Figure 4. Features that have a large enough area were still found and the sharp edges were recovered effectively. However, the noise leakage at the boundaries between monotonic segments overwhelms the recovered signal. The noise leakage at the boundaries can be reduced by averaging the monotonic fits

obtained with several (5 to 11) boundary points near the maximum. If the average is weighted by the error between the data and the fit, sharp peaks can still be recovered. However, computation times increase enough to discourage use of this technique on images.

III. METHODS

The first method of processing images to try is to simply process the rows of the image, then rotate the result and process the rows again. Then iterate by rotating the result and processing the rows until nothing is changing and quit. This simple method works pretty well but it needs to be modified a bit because of two directional effects.

A. Directional Effects

The first is that there are many kinds of extrema in two dimensions. It is a directional property in two dimensions; i.e., a point can be an extrema in one direction but not in another. For example, a saddle point is an extrema in all directions but two. Therefore, the extrema must be determined independently for each direction processed in an image. The second directional effect is somewhat more subtle. When an image is processed in multiple directions, most of the noise is suppressed in the first direction processed. The leakage of noise at the boundary between monotonic segments is greatest perpendicular to the first direction processed and much less in other directions. The results of making the columns monotonic first and then the rows is different from those obtained by making the rows monotonic first and then the columns. If this effect were limited to the edges of the image it would be tolerable but it occurs at each and every boundary between segments throughout the image. The leakage of noise at boundaries leads to the widening of a peak perpendicular to the first direction made monotonic. The effect is demonstrated in Figure 6. Just noise was processed to show how it is blurred. If the rows are made monotonic first, the rows stay essentially monotonic after the columns are made monotonic. Therefore, each direction needs to be made monotonic only once.

B. Algorithm

Our method of processing images attempts to handle these directional effects. An intermediate image was found for each angle used. To obtain the an intermediate image, the original image was rotated to the appropriate angle. The rotated images were obtained by interpolating to a rotated grid using cubic B-splines [9, 8]. The rotated version of the image was blurred using a simple Gaussian filter in the Fourier domain. The extrema along the rows and along the columns of the blurred image were identified. The two sets of extrema were examined and those that differed from adjacent extrema by less than the threshold were eliminated. Each row of the image was made monotonic between extrema. Then the columns of the row processed image were made monotonic between extrema. The row-column processed image was averaged with the column-row processed image to obtain the intermediate image. Making

the image monotonic in two directions is sufficient to suppress most of the noise and keep most of the features. Processing the image at more angles to get the intermediate image takes too much processing time. Each intermediate image had the noise leakage primarily perpendicular to the first direction made monotonic. To remove the noise leakage, intermediate images at several angles were averaged together. Actually the intermediate images were least squares fit to the original image to obtain the final processed image. A simple average can also be used instead of a least squares fit. The final processed image is almost monotonic between extrema in all directions and contains no preferred directional effects.

IV. RESULTS

The preliminary results are very promising. Noise can be suppressed significantly. Good quality images can be extracted from noise that would otherwise make the images of very limited usefulness. The first example is an MRI of a phantom shown in Figure 7. The imaging technique selected produced very noisy images. The 'true' image was obtained from averaging 64 of the images to suppress noise through averaging. Four angles were used in the noise suppression. The edges and most of the small features are recovered well. The first two rows of small pins in the black field on the upper left section of the phantom are retained. The edges remain sharp. However, the fan shaped resolution pattern is less well seen. Smaller parts of the fan pattern could probably be visualized if more angles were used. Most of the noise remaining in the noise suppressed image is leakage at the boundaries between segments. The second example is of a functional MRI (fMRI) image. Functional MRI is a procedure that identifies areas of the brain that are used to perform mental tasks such as the motor strip or the areas used for different kinds of memory. Surgeons need such information to avoid critical areas of the brain when operating. It is also important to understand damage and reorganization of the brain following injury such as stroke or trauma. In fMRI many sequential images of the brain are obtained during a mental task and during rest from that task. The area of the brain that is active during the task has very small signal intensity changes that correlate with the task being on and off. These signal changes are caused by increased blood flow during activation and are only around two percent of the signal. Noise or patient movement can render the study inconclusive. The image shown in Figure 8 is a single image from an fMRI study. The monotonic noise suppression produces excellent results. Eight angles were used in the noise suppression. The noise suppressed image has almost all the features present in the original but the noise is reduced significantly. The gray and white matter can also be more easily segmented in the noise suppressed image. The regions of similar signal intensity are grouped very well. The third example is an T1 weighted MR image of a brain study. One of the important features of T1 weighted images is to differentiate gray and white matter. The gray matter is the less bright shell of tissue forming the cortical surface. The brighter white matter is inside the gray and the dark cerebrospinal fluid that cushions the brain is between the gray matter and the skull. Eight angles were used in the noise suppression. Noise was added to the image to reduce the SNR from 80 to 16 and more noise was added to decrease the SNR farther to 4. The

monotonic noise suppression increased the SNR from 16 to 85 and from 4 to 30. The gray-white matter separation is recovered well.

A. Applications

There are many potential applications of monotonic noise suppression but two applications are the most promising. Segmentation is the most natural. Areas that have similar signal intensities are grouped into contiguous regions very effectively. Recovery of images in very high noise is the other natural application because this technique works well at high SNR's and at very low SNR's. Most noise reduction methods do not perform well at low SNR's. For example, in mammography we are using monotonic noise suppression as a preprocessing step for a watershed algorithm that is used to segment the digitized mammograms. Monotonic noise suppression can be adjusted to remove the small features that tend to make the watershed algorithm oversegment.

B. Future Improvements

This technique is still being actively developed and there are many improvements to be made. Many of the improvements necessary require better theoretical understanding. For example, how many angles need to be used to suppress noise adequately? The answer will depend on the area of the regions between extrema; more angles will be needed for larger areas. How fast can extrema change with angle? Most extrema are found if only four angles are used. Can the leakage at the boundaries be suppressed without eliminating smaller features? The most important improvement to make is to make the selection of extrema more robust and automatic. The same tricks that are used to find maximum gradient points in wavelet denoising can be applied here as well. For example, tracking extrema across multiple scales and using continuity would probably help. Also estimating the cutoffs that determine the extrema automatically from the estimated SNR would help. Now the selected extrema are shown on the screen to select the correct cutoff parameters.

V. CONCLUSIONS

Forcing monotonic change between extrema is a very promising noise suppression technique. Edges are not blurred and it works well over a wide range of SNR's. As the SNR drops, features that have less energy than the noise spikes are lost. The key to recovering the image accurately is to identify the correct extrema.

REFERENCES

- [1] S.G. Mallat, A theory of multiresolution signal decomposition: the wavelet representation, *IEEE Trans. Patt. Anal. Machine Intell.*, Vol. PAMI-11, No. 7, pp. 674-693, 1989.
- [2] J.B. Weaver, Yansun Xu, D.M. Healy, Jr., L.D. Cromwell, Filtering Noise From Images With Wavelet Transforms., *Magnetic Resonance in Medicine*, 21:288-295, 1991.
- [3] S. Mallat, Characterization of Signals from Multiscale Edges, *IEEE Trans on PAMI*, Vol. 14, 1992, pp. 710-732.
- [4] Jian Lu, J.B. Weaver, D.M. Healy, Jr., Yansun Xu, Noise Reduction with Multiscale Edge Representation and Perceptual Criteria., *Proceeding of the IEEE-SP International Symposium on Time-Frequency and Time-Scale Analysis*, Victoria, B.C., October 1992..
- [5] Yansun Xu, J.B. Weaver, D.M. Healy, Jr., Jian Lu, Wavelet Transform Domain Filters: A Spatially Selective Noise Filtration Technique., *IEEE Trans. on Image Processing*, 3(6) 747-758 Nov 1994.
- [6] D.L. Donoho, De-noising by soft-thresholding., *IEEE Trans on Info Theory*, Vol. 41, 1995, pp. 613-627.
- [7] I.C. Demetriou and M.J.D. Powell, Least Squares Smoothing of Univariate Data to Achieve Piecewise Monotonicity, *IMA Journal of Numerical Analysis*, Vol. 11, No. 2, 1991, pp. 411-432.
- [8] M. Unser, A. Aldroubi, M. Eden, Fast B-Spline Transforms for Continuous Image Representation and Interpolation, *IEEE Trans. Patt. Anal. Machine Intell.*, Vol. 13, No. 3, pp. 277-285, Mar. 1991.
- [9] M. Unser, A. Aldroubi, M. Eden, Pyramid, The L_2 Polynomial Spline Pyramid, *IEEE Trans. Patt. Anal. Machine Intell.*, Vol. 15, No. 4, pp. 364-379, April 1993.

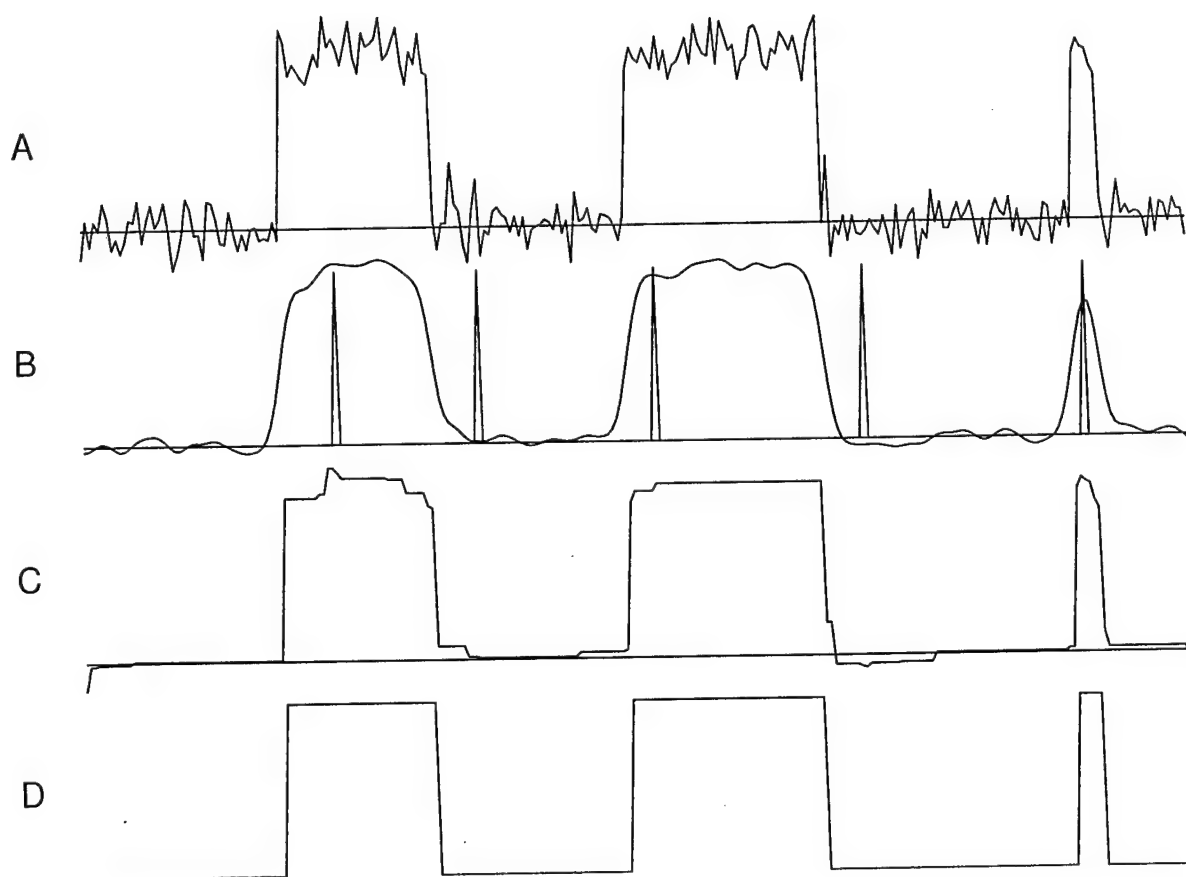


Fig. 1. An example of suppressing noise on a line segment with a simulated signal and normally distributed random noise. The signal is three boxcars. The height of the boxcars is 1. The boxcars, from left to right, are 35, 45 and 6 pixels wide. The signal with added noise is shown in A. The standard deviation of the normally distributed random noise is 0.1. The Gaussian smoothed signal with the extrema selected are shown in B. Standard deviation of the Gaussian is 4 percent of the total bandwidth and the extrema were required to change by 20 percent of the maximum signal. The result of forcing monotonic change between the extrema is shown in C. The original signal before noise was added is shown in D for comparison.

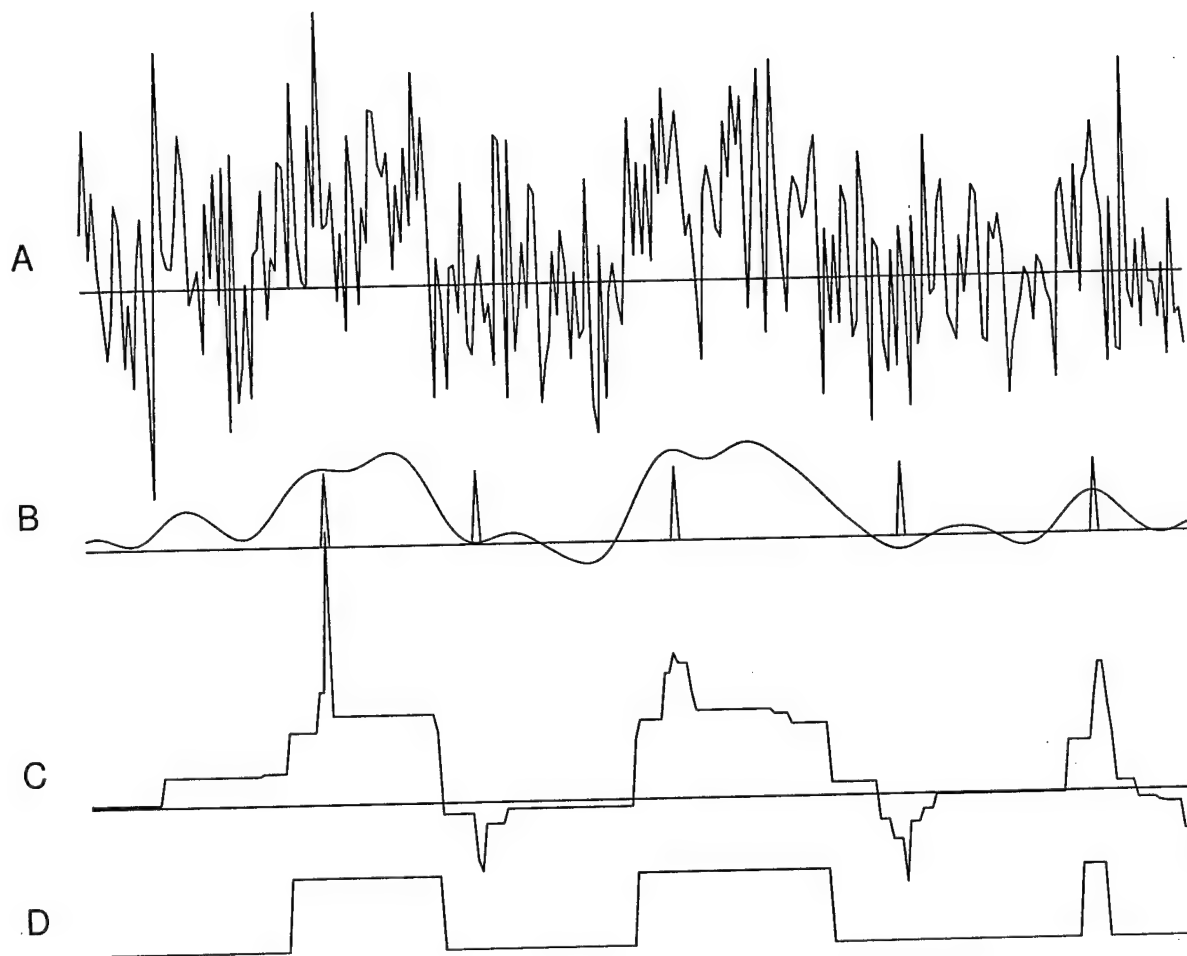


Fig. 2. The result when the noise is much larger. The same signal as in Figure 1 was corrupted with noise with a standard deviation of 1 instead of 0.1. The format is the same as in Figure 1.

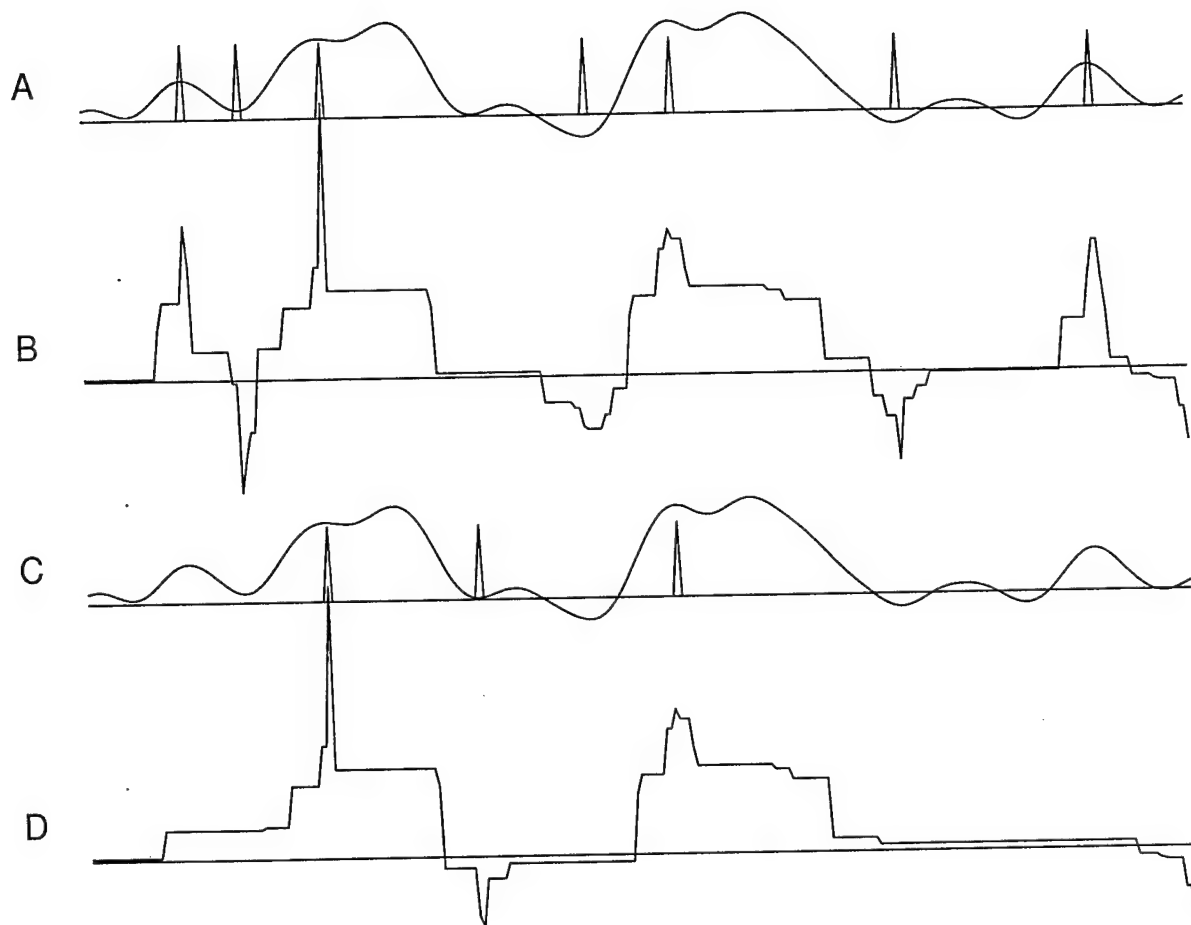


Fig. 3. The result of suboptimal selection of extrema. Figure 2 was reconstructed with extrema that were larger than 15 percent of the maximum. Figures A and B show the result of selecting extrema larger than 10 percent of the maximum. Figures A and C correspond to B in Figure 2 and Figures B and D correspond to C in Figure 2. The lower threshold result in two new extrema seen to the far left of the segment. That extra extrema produces a rather large peak in the final result. Figures C and D show the result of selecting the extrema larger than 20 percent of the maximum. The extrema over the 6 pixel wide spike in the signal is lost and does not appear in the final result.

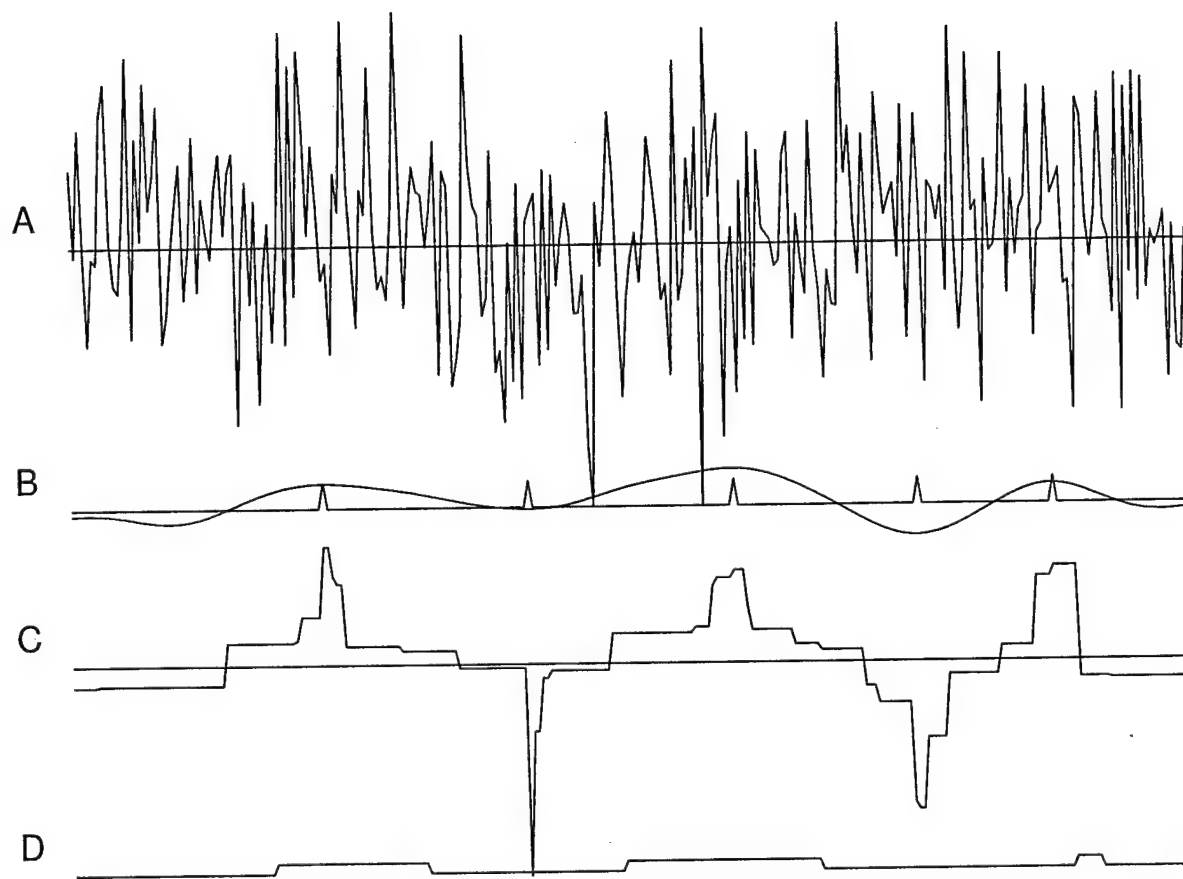


Fig. 4. The result with extremely large noise. The same signal as in Figure 1 was corrupted with noise with a standard deviation of 10. The format is the same as in Figure 1. Figures A-D are scaled the same.

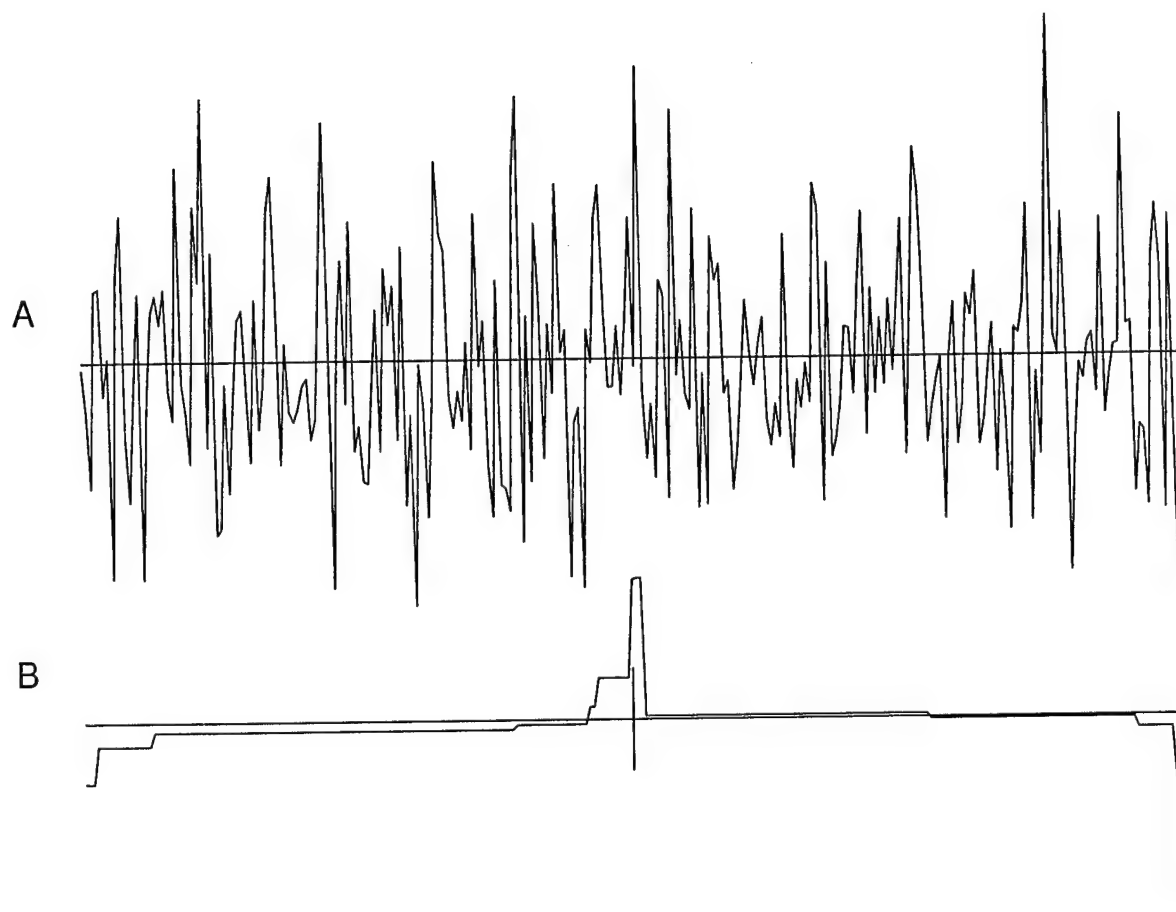


Fig. 5. The result of forcing monotonic change on normally distributed random noise shows the leakage of noise at the boundaries between monotonic segments. The random series was monotonically fit to two segments: the first increasing and the second decreasing. There is always a false peak at the boundaries between monotonic segments because the monotonic fit allows negative noise to pass at the beginning of the segment and positive noise to pass at the end of an increasing segment. In the middle of the segment, values to either side are enough to average out the positive and negative noise.

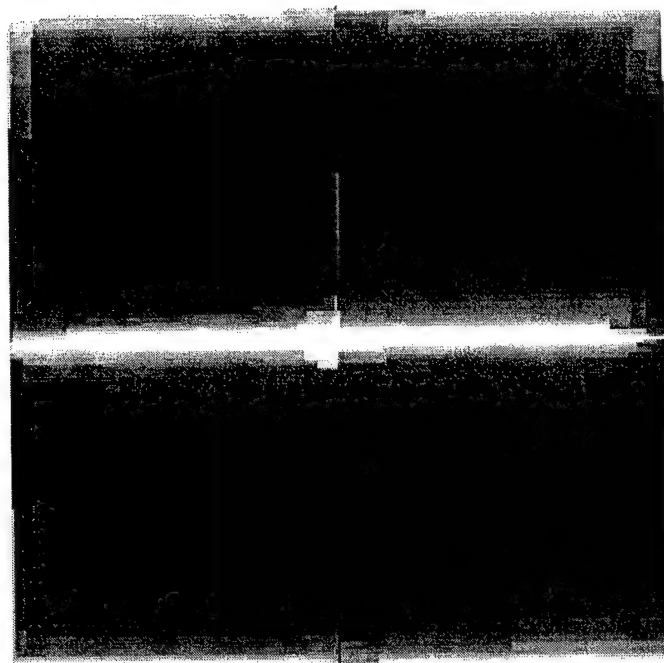


Fig. 6. A field of random numbers with standard deviation 1024 was made monotonic along the columns first and then along the rows. The center row were the maxima when the columns were processed and the central column were the maxima when the rows were processed. The result shows the directional blurring of noise perpendicular to the direction first processed.

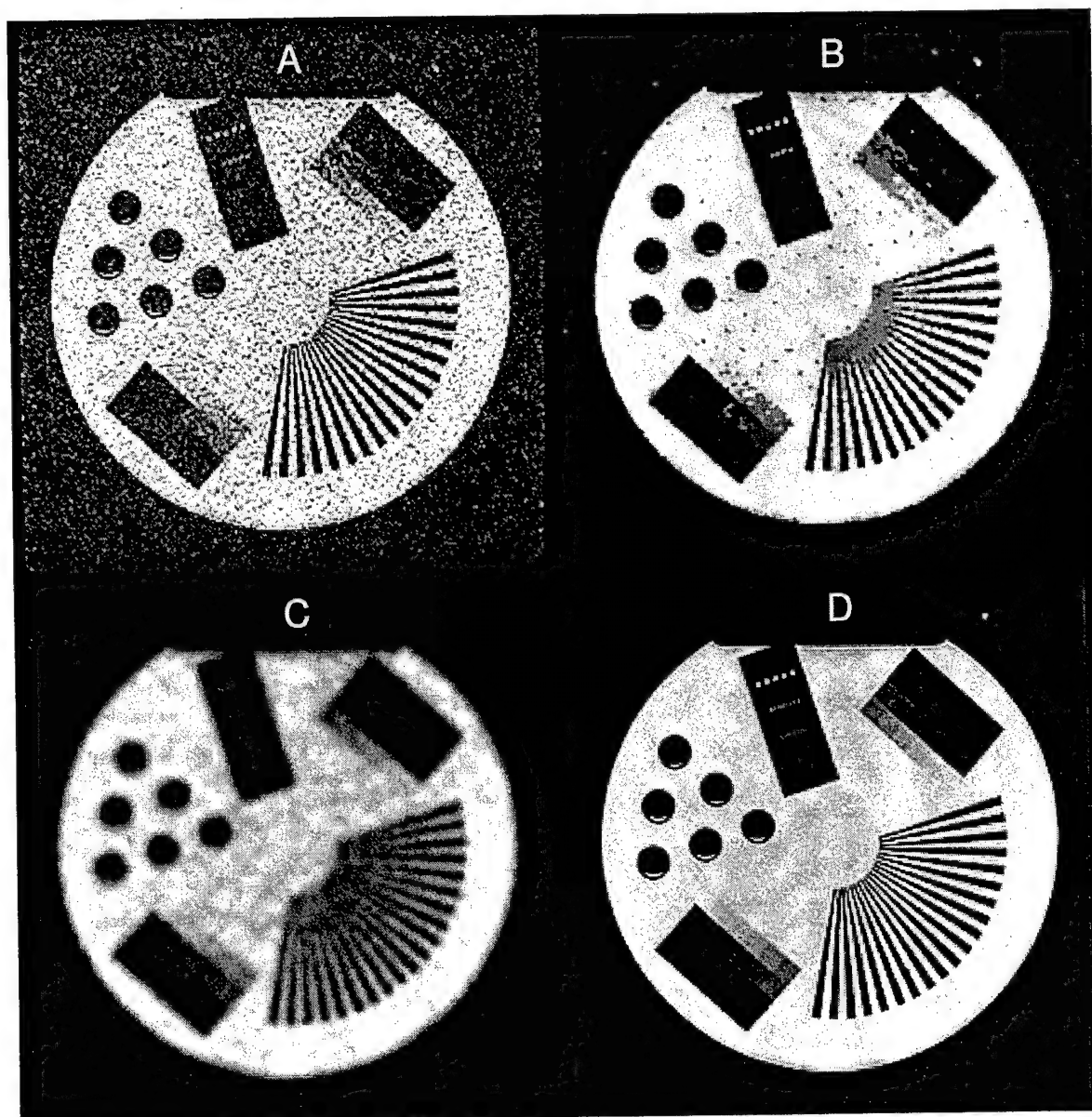


Fig. 7. Figure A shows an MRI image of a phantom. The imaging technique used produced a very poor SNR image, shown in Figure A. Figure B shows the results of noise reduction using monotonic fits between extrema. Figure C shows a Fourier filtered image with the same SNR as in Figure B; the blurring limits the usefulness of the image. Figure D shows the average of 64 acquisitions averaged together to reduce noise. The SNR in Figure D is 8 times that in Figure A.

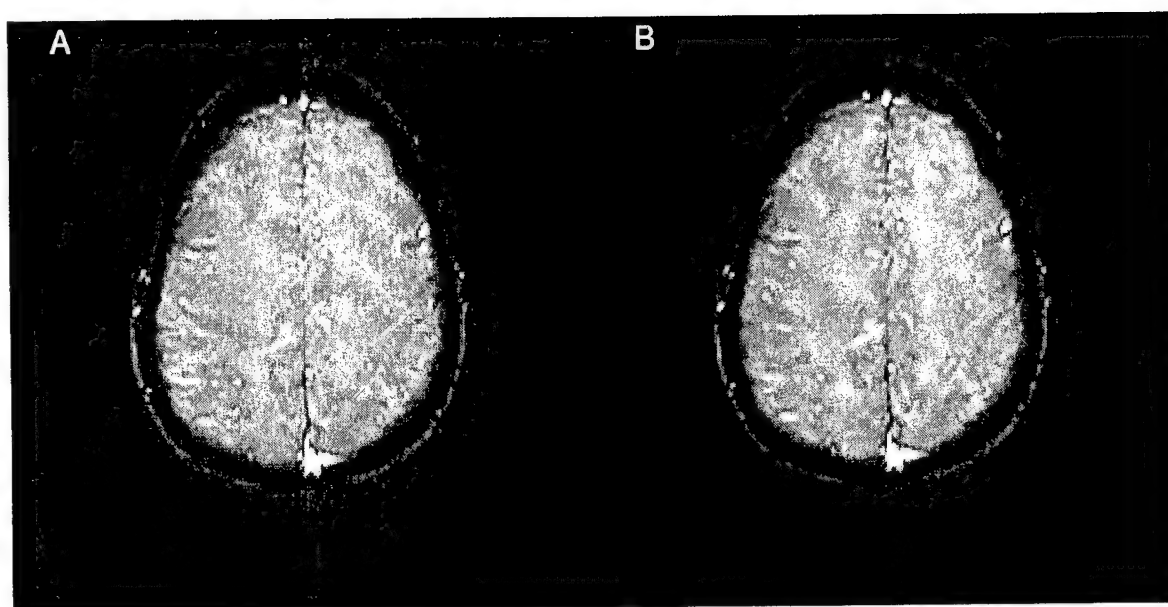


Fig. 8. Figure A shows the original axial MR image and Figure B shows the results of forced monotonic noise suppression. The parameters were set to produce uniform areas that could be useful in segmentation. The SNR is improved significantly by forced monotonic noise suppression.

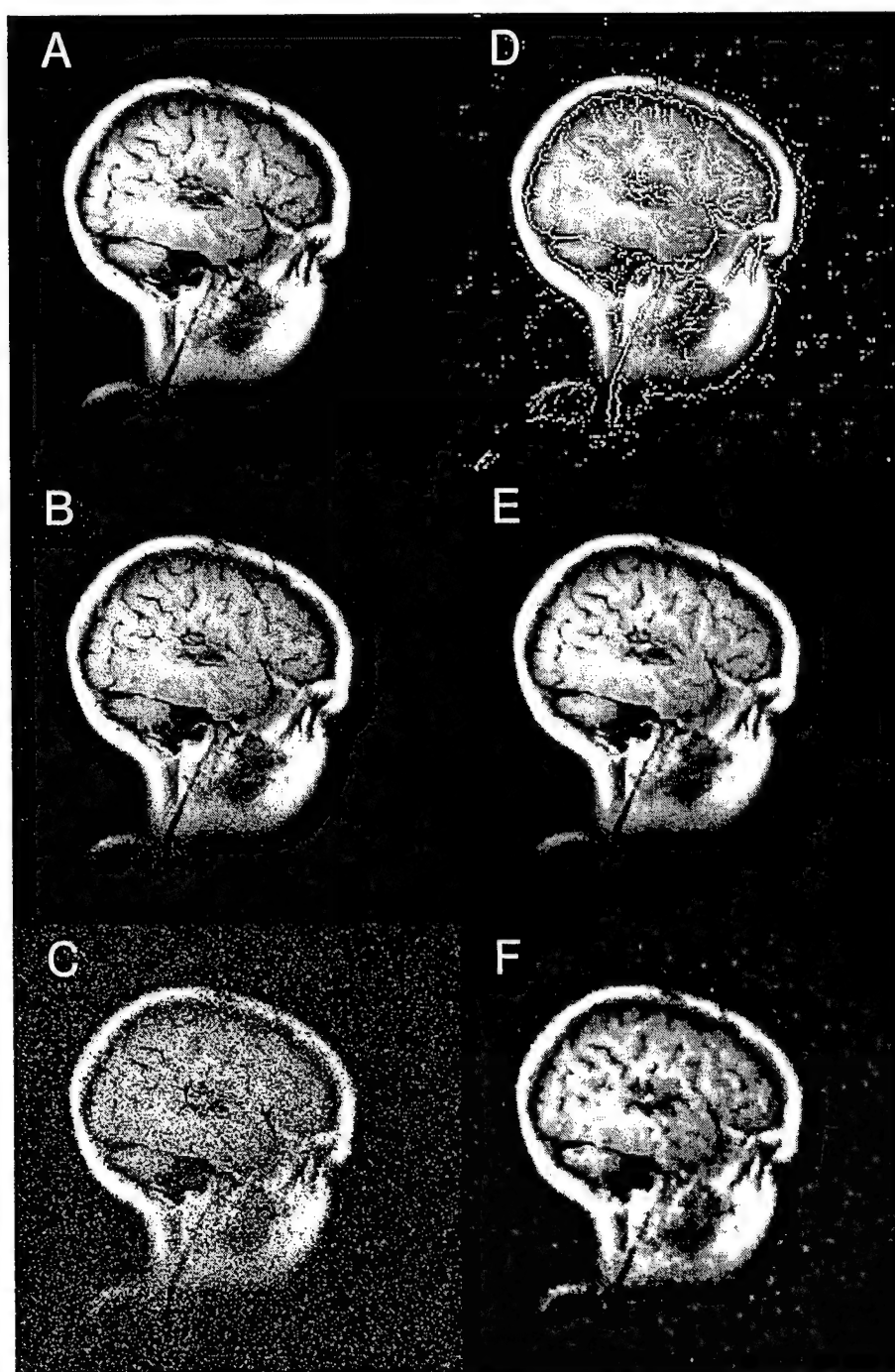


Fig. 9. Figure A shows the original T1 weighted sagittal MR image that has a relatively high SNR, SNR=80 within the brain. Figures B and C show the original image with added normally distributed random noise, SNR=16 and SNR=4 within the brain for Figures B and C respectively. Figure D shows the Gaussian filtered image with the selected extrema superimposed. Figure E shows the result of forced monotonic noise suppression on Figure B. The SNR increased from 16 to 85. Figure F shows the result of monotonic noise suppression on Figure C. The SNR is increased to from 4 to 30.

Monotonic Noise Suppression Used to Improve the Sensitivity of fMRI Activation Maps

John B. Weaver

We have introduced a new method of removing noise from images that identifies significant extrema and forces the pixel intensities between any two extrema to change monotonically. The method has some similarities to wavelet denoising methods we worked with several years ago but is generally more stable and is effective on images with lower SNR's. In this paper the method of monotonic filtering is used to increase the sensitivity in functional magnetic resonance imaging (fMRI) studies. We have used the increased sensitivity to improve the temporal resolution in fMRI studies by roughly a factor of six. A motor activation study was acquired with single slice 256×256 pixel T2* weighted images; six cycles of finger tapping were acquired. Each cycle consisted of five images of rest followed by five images of right hand finger tapping followed by five images of left hand finger tapping. The z-scores were calculated and used as the activation map. The left and right activations were both clearly visible when all six cycles were used in the analysis. However, no definitive activation was seen for any one cycle. When the original 256×256 images were averaged down to 64×64 pixel images before calculation of the z-scores, the activations were partially identified. When the original images were filtered using the monotonic noise reduction algorithm, the left activation was clearly visible in three of the six cycles and partially visible in two others. The right activation was partially visible in 4 out of 6 cycles. Optimized noise reduction should improve the results significantly. The ability to use a single cycles is very important in fMRI studies because many stimuli are more difficult to maintain over many cycles and because complex processes such as in cognitive or memory activity do not have simple responses.

Copyright © 1998 by W.B. Saunders Company

NOISE REDUCTION has many applications: eg, as a preprocessing step for many image interpretation algorithms, in segmentation, in contrast enhancement among many others. Noise reduction can be seen as finding the features in the image

and preferentially separating the features from the noise in some way. Fourier filters reduce the high frequencies where noise is assumed to be dominant and leave the low frequencies where signal is assumed to be dominant. The undesired result is bandlimited blurring of real features. Wavelet denoising¹⁻⁶ improves the situation by allowing the bandwidth passed to be increased around edges in the image and decreased in flat regions. This mitigates the bandlimited blurring if the edges can be found in the image. Indeed the key to wavelet denoising is correctly identifying the edges. Shrinkage algorithms assume that large wavelet coefficients are likely to be a result of an edge and smaller wavelet coefficients are likely to be noise. Therefore, the larger coefficients are kept and the smaller ones are suppressed.

Functional magnetic resonance imaging (fMRI) looks for small changes in blood flow that are produced by mental activity associated with mental tasks. The signal changes are on the order of the noise in MR images. They are generally around 3%.⁷ Identifying these changes in MR images with comparable noise is a difficult task. The signal can only be found by averaging over many cycles of the task. However, many tasks are difficult to consistently sustain over multiple cycles; e.g., cognitive tasks or other tasks with multiple parts and complex activations. We are using monotonic noise reduction to reduce the number of activation cycles required to identify the region activated.

METHODS

Monotonic Noise Reduction

Monotonic noise reduction^{8,9} finds the significant extrema, both the maxima and the minima, and forces monotonic change between the extrema. The procedure is best described in one dimension first and then extended to two dimensions. The significant features are the extrema in a slightly blurred image that are different from adjacent extrema by a user defined minimum value. The selection of the correct extrema is of critical importance. When the significant extrema have been selected, the signal must by definition change monotonically between any pair of adjacent extrema. Monotonic change is forced by using an elegant, simple algorithm for finding the monotonic series of numbers that fits the original series best in the least squares sense.¹⁰ The monotonic fit averages large

From the Department of Radiology, Dartmouth-Hitchcock Medical Center, Lebanon, NH.

Supported by DOD-AMRD, DAMD17-96-1-6119 and NIH grant H133G70031-98.

Address reprint requests to John B. Weaver, Ph.D., Department of Radiology, Dartmouth-Hitchcock Medical Center, One Medical Center Drive, Lebanon, N.H. 03756.

*Copyright © 1998 by W.B. Saunders Company
0897-1889/98/1103-1015\$8.00/0*

Fig 1. A flow chart of the steps taken to obtain the extrema in all four directions that are used in the monotonic noise reduction algorithm. The image is blurred using a simple Gaussian filter in the Fourier domain to average out small extrema. Then the pixels are reordered into strings that follow the four primary directions and the extrema are selected in each reordered string of numbers. Only extrema that are different from adjacent extrema by more than a threshold are included in the four final sets of extrema. The user selects the width of the Fourier filter and minimum difference between extrema. These two parameters determine how small a feature is rejected as noise or is included in the final image.

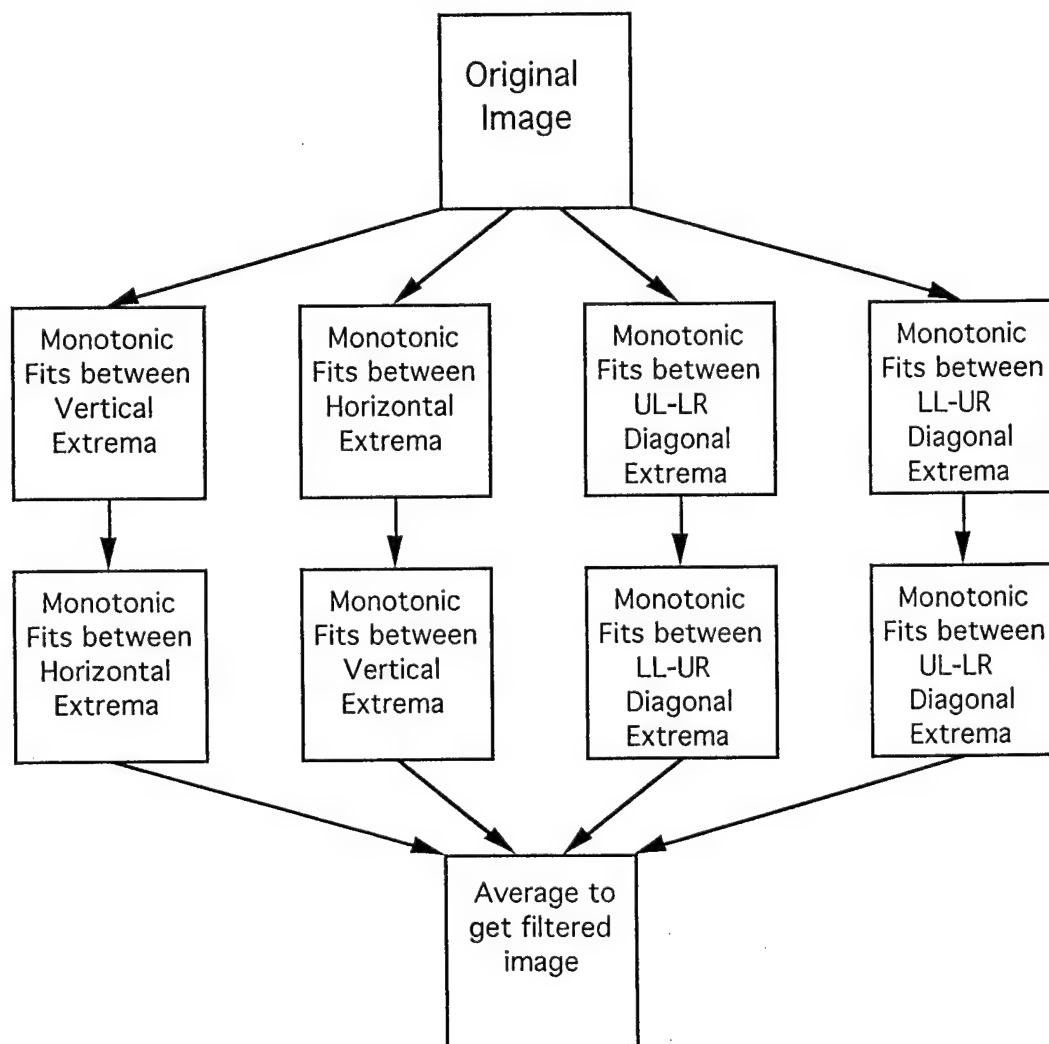
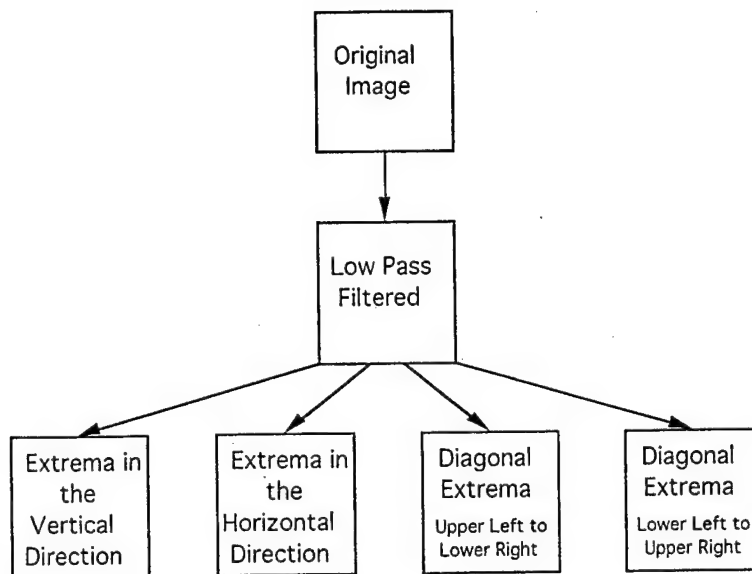


Fig 2. A flow chart of the steps taken in monotonic noise reduction. The pixels in the original image are reordered along the four primary directions and the pixel values between extrema are fit to monotonic functions. The resulting series of pixel values are reordered in the direction orthogonal to the first direction and the pixel values between that set of extrema are fit to monotonic functions. The resulting four images are averaged to form the final filtered image.



Fig 3. The fifth resting image in the raw data from a motor activation study.

enough groups of adjacent points in the series to achieve a monotonic progression. It is robust and relatively fast. The resulting monotonic series is not just a fit to a limited set of basis functions. The monotonic series is not bandlimited so edges are not blurred.

The extension to two dimensions is complicated because an extrema in one direction is not necessarily an extrema in another direction. For example, pixels along a ridge will be extrema perpendicular to the ridge but not along the ridge. The method we use is to find the extrema in four directions as in Fig 1 and filter the image separately in four directions: horizontal, vertical, diagonal upper-left to lower-right, and diagonal lower-left to upper-right. There are four intermediate images formed by first filtering the original image in each of the four primary directions. The intermediate images are then filtered in the direction perpendicular to the first filter direction. Filtering in other directions can be done but produces little change. Once an image has been filtered in two orthogonal directions, it is essentially monotonic in the other directions, too. However, the four intermediate images are all different valid solutions that are essentially monotonic in all four directions. We average the four

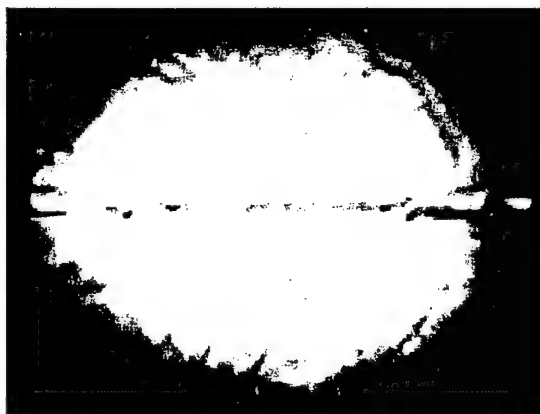


Fig 4. The results of monotonic noise reduction on the fifth image in the motor activation study. The noise is significantly reduced from that in Fig 3.

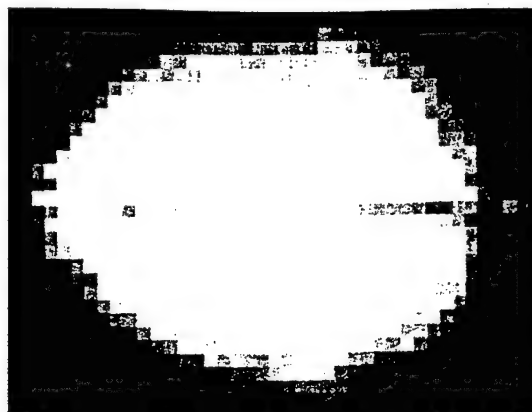


Fig 5. The fifth image in the motor study after it has been averaged down to a 64×64 image. Each pixel is the average of sixteen pixels in the full resolution image. The noise is reduced but the resolution suffers.

to obtain the final filtered image. The procedure is outlined in Fig 2.

We have tried a weighted least squares fit of the four to the original image but it is a little more unstable and does not produce a noticeably better image. We have also filtered the image in more than four directions but the most improvement in image quality is obtained in the first four directions so we usually limit ourselves to four directions.

fMRI Protocol

An axial plane four cm below the apex of the cranium was imaged. Six cycles of rest and motor activation were obtained. Each cycle of images consisted of five resting images followed by five images taken during tapping of the right hand followed by five images taken during tapping of the left hand. Each gradient echo image was a 256×256 , 24 cm field of view, image with TR of 70 ms and TE of 40 ms. The images were strongly T2* weighted to identify BOLD contrast changes.



Fig 6. The average of all 90 images from the study provides a relatively noise free comparison. The noise and resolution resemble that in the monotonically filtered image in Fig. 4 more closely than that in the original image in Fig 3 or that in the reduced resolution image in Fig 5.

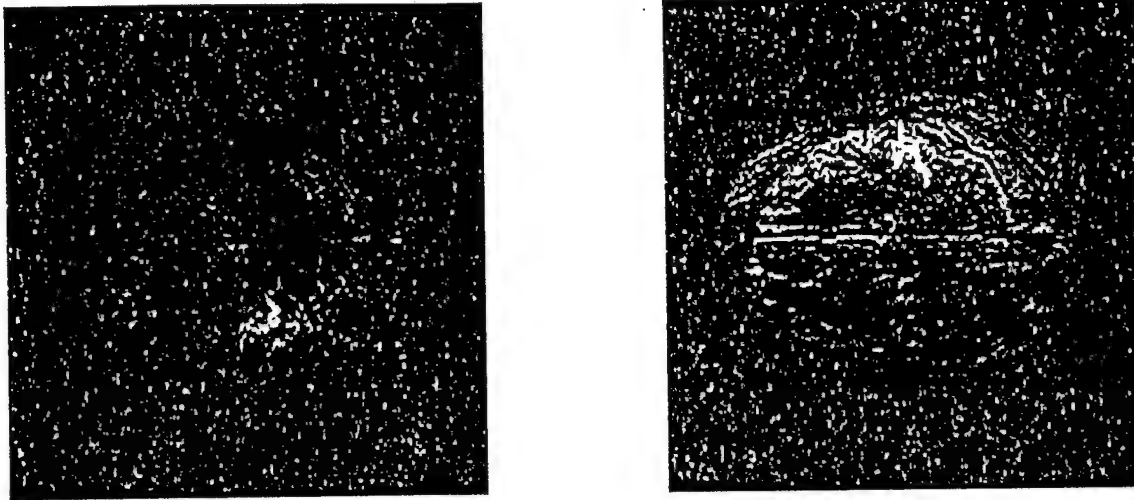


Fig 7. The full resolution 256×256 pixel reference activation maps for the right hand motor task (on the left) and the left hand motor activation task (on the right). The map is the correlation with the right hand motion over the standard deviation of the intensities at that pixel position. All six cycles were used to obtain the activation maps. The activations are clearly present in the expected locations.

Activation Maps

Simple z-scores for each pixel were used to identify activated regions. The standard deviation of the ninety images was used as a measure of the total variation in signal. To obtain the reference activation maps all six cycles were used to obtain the z-scores. To obtain the signal correlated with right hand finger tapping, the average of the rest and left hand tapping was subtracted from the average of the right hand finger tapping. The activation map for the right hand motor task was the ratio of the signal correlated with right hand finger tapping over the total variation in signal. Similarly, the activation map for the left hand motor task was the ratio of the signal correlated with left hand finger tapping over the total variation in signal. No realignment of the images was done.

Single Cycle Tests

The reference activation maps were obtained with all six task cycles. The reference activation maps were used as the gold standard showing the true regions activated which were taken to be the motor centers. During any single task cycle there could be transient activation in other areas or lack of activation in the regions identified in the reference activation maps. However, the regions shown in the reference activation maps do show the most likely areas activated.

The activation maps for each cycle were calculated and compared to the reference activation maps. The images were processed in two ways to average out noise in the images and help make single cycle activations definitive. First, the images were averaged down from 256×256 pixels to 64×64 pixels.

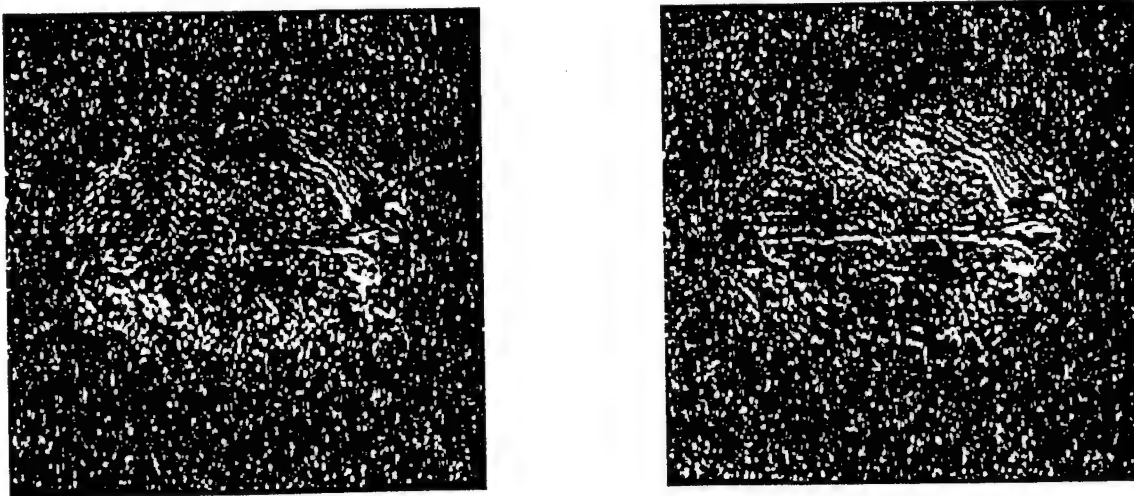


Fig 8. The full resolution 256×256 pixel activation map obtained using the fourth task cycle. The right hand motor task is on the left and the left hand motor activation task is on the right. No activation can be identified without reference to the maps in Fig 7. There are a few pixels in the motor areas but not enough to differentiate the motor centers from other areas in the maps.

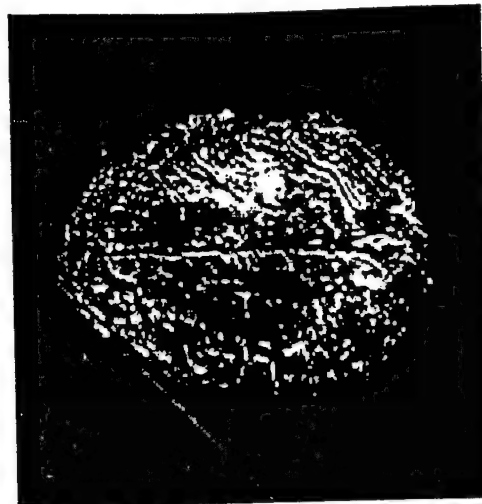
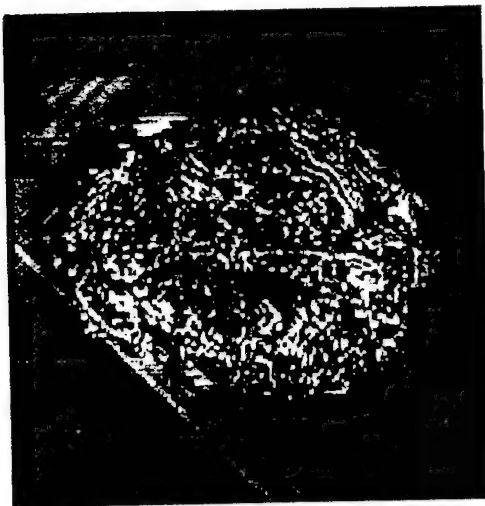


Fig 9. The activation maps obtained from the full resolution, monotonically filtered images when only the fourth task cycle was used. The right hand motor task is on the left and the left hand motor activation task is on the right. The left hand activation is clearly visible but more dispersed than in the reference activation maps. This could be the real activation that was averaged away in the composite activation maps or it could be the result of noise. The right hand activation is visible when compared to Fig 7 but it is not as clear as the left hand activation.

The averaging reduced noise but also reduced the resolution. Second, the images were processed with monotonic noise reduction. The resolution remained the same as in the original images.

RESULTS AND DISCUSSION

The fifth image of the study is shown in Fig 3. The same image after monotonic noise reduction and after averaging are shown in Figs 4-5. The average image of the 90 image study is shown in

Fig 6 for comparison. The noise that is apparent in Fig 3 is much reduced in Fig 4 without loss of significant features. The resolution in Fig 5 suffers significantly.

Figure 7 shows the reference activation maps obtained with all six task cycles. The right and left motor centers are clearly visible. The locations of both motor centers are also in roughly the same locations as in most subjects. The signal that correlates with the activation is around seven times

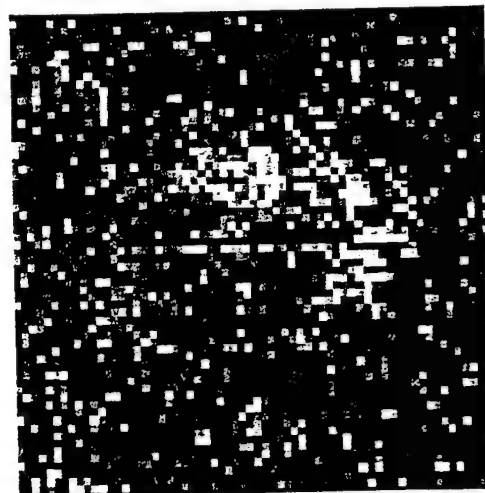
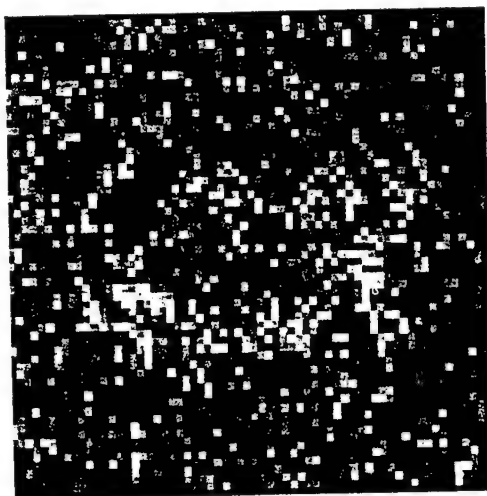


Fig 10. The 64 by 64 pixel, activation maps obtained from the reduced resolution images when only the fourth task cycle was used. The right hand motor task is on the left and the left hand motor activation task is on the right. The left hand activation is clearly visible. The right hand activation is not visibly different from other areas in the map.

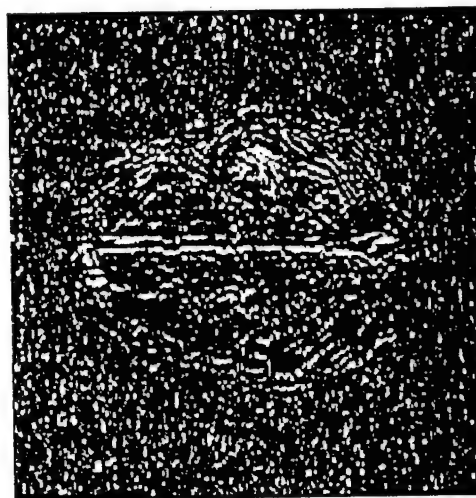
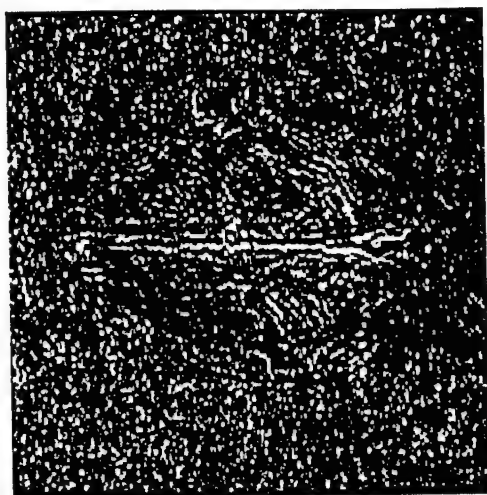


Fig 11. The full resolution 256×256 pixel activation map obtained using the fifth task cycle. The right hand motor task is on the left and the left hand motor activation task is on the right. No activation can be identified. Regions of activation can only be seen if compared to the known activation maps in Fig 7.

the standard deviation in the activated pixels so the confidence in the activations is high.

The fourth and fifth single cycle activation maps are shown in Figs 8-13. The other single cycle maps are similar. No definitive activation was seen for any one cycle without filtering or averaging the images prior to calculation of the activation map. The activations in Figs 8 and 11 can be seen in retrospect if compared to the six cycle activations in Fig 7. The activation maps obtained from the monotonically filtered images in Figs 9 and 12 show the left hand activation very clearly. The right

hand activation can be seen retrospectively if compared to the six cycle activation maps in Fig 7. The reduced resolution activation maps in Figs 10 and 13 are similar to the monotonically filtered activation maps. The left hand activations are visible but the activation for the right hand task is even less visible than in the maps obtained from the monotonically filtered images. The reduced right hand visibility might be a partial volume effect.

A method to optimize the monotonic filter settings is needed to improve the results. The filter settings were set arbitrarily to what produced a

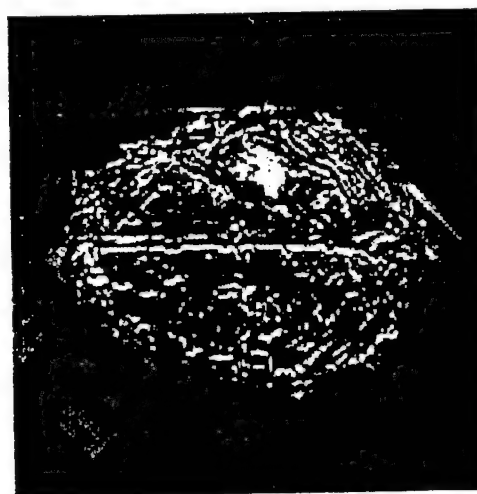
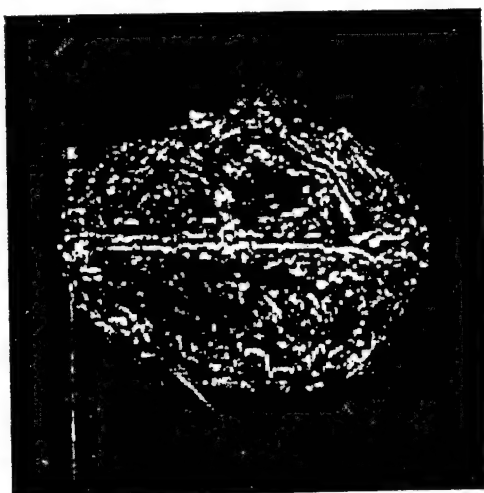


Fig 12. The activation maps obtained from the full resolution, monotonically filtered images when only the fifth task cycle was used. The right hand motor task is on the left and the left hand motor activation task is on the right. The left hand activation is clearly visible but again it is more dispersed than in the reference activation maps. The right hand activation is also only visible when compared to Fig 7.

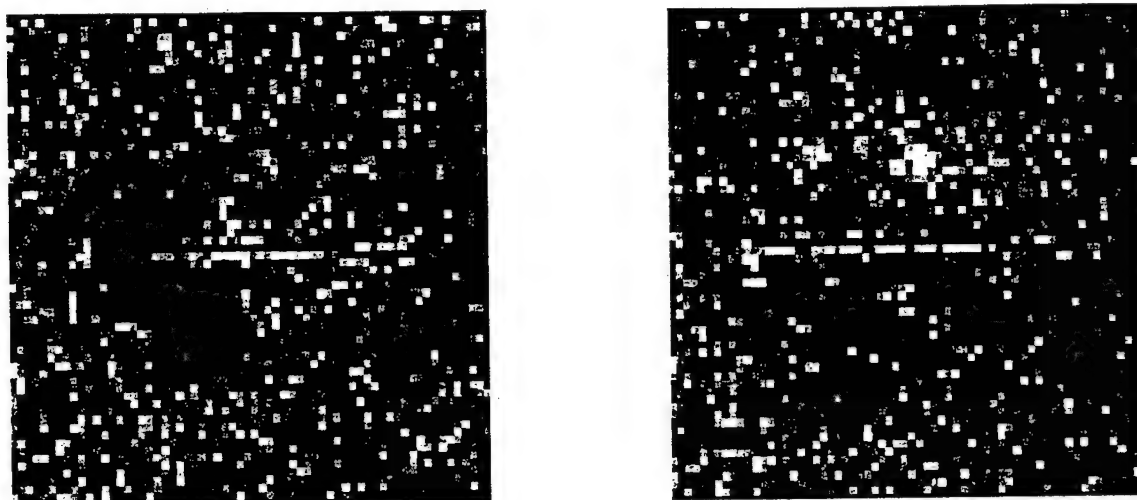


Fig 13. The 64 by 64 pixel, activation maps obtained from the reduced resolution images when only the fifth task cycle was used. The right hand motor task is on the left and the left hand motor activation task is on the right. The left hand activation is clearly visible. The right hand activation is not visibly different from other areas in the map.

visually good image. Better results can probably be obtained with optimal filter settings.

CONCLUSIONS

Forcing monotonic change between extrema is a promising noise suppression technique. Edges are not blurred and it works well over a wide range of SNR's. As the SNR drops, features that have less energy than the noise spikes are lost but edges are not blurred. The key to recovering the image accurately is to identify the correct extrema.

We used the monotonic filtering method to

reduce the noise in functional magnetic resonance (fMRI) images. It improves the SNR enough to identify motor activations from a single task cycle rather than multiple cycles in some cases. The increased visibility of activated regions is comparable to that obtained by averaging the pixels in the images to reduce the noise. However, the resolution is not degraded when monotonic noise reduction is used as it is when the pixels are averaged. Because monotonic filtering is effective at much lower SNR's than the common wavelet filtering methods, it is particularly useful in fMRI studies where the noise is relatively high.

REFERENCES

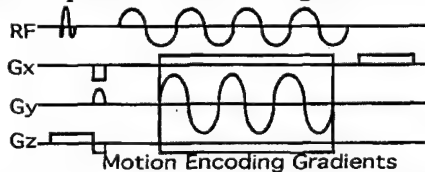
1. SG Mallat: "A theory of multiresolution signal decomposition: the wavelet representation." IEEE Trans. Patt. Anal. Machine Intell., Vol. PAMI-11, No. 7, pp. 674-693, 1989
2. JB Weaver, Yansun Xu, DM Healy, Jr., LD Cromwell: "Filtering Noise From Images With Wavelet Transforms," Magn Reson Med, 21:288-295, 1991.
3. S Mallat: "Characterization of Signals from Multiscale Edges," IEEE Trans on PAMI, Vol. 14, 1992, pp. 710-732.
4. Jian Lu, JB Weaver, DM Healy, Jr., Yansun Xu: "Noise Reduction with Multiscale Edge Representation and Perceptual Criteria," Proceeding of the IEEE-SP International Symposium on Time-Frequency and Time-Scale Analysis, Victoria, B.C., October 1992.
5. Yansun Xu, JB Weaver, DM Healy, Jr., Jian Lu: "Wavelet Transform Domain Filters: A Spatially Selective Noise Filtration Technique," IEEE Trans. on Image Processing, 3(6) 747-758 Nov 1994.
6. DL Donoho: "De-noising by soft-thresholding," IEEE Trans on Info Theory, Vol. 41, 1995, pp. 613-627.
7. R Turner, P Jezzard, H Wen, KK Kwong, D Le Bihan, T Zeffiro, RS Balaban, "Functional mapping of the human visual cortex at 4 and 1.5 tesla using deoxygenation contrast EPI," Magn Reson Med 29(2), 277-9 (1993).
8. JB Weaver: "Reducing Noise in Images by Forcing Monotonic Change Between Extrema," The International Society for Analysis, its Applications and Computation (ISAAC), 1997.
9. JB Weaver: "Removing Noise from Images: Least Squares Monotonic Functions on Line Segments Through the Image" Proceedings of the Society of Magnetic Resonance, Vancouver, Canada, August, 1997, p 2043.
10. IC Demetriou and MJD Powell: "Least Squares Smoothing of Univariate Data to Achieve Piecewise Monotonicity," IMA Journal of Numerical Analysis, Vol. 11, No. 2, 1991, pp. 411-432.

Measurement of Harmonic Motion for MR Elastography

J. B. Weaver†, E. van Houten§, M. I. Miga§, F. E. Kennedy§, A. Hartov§, S. P. Poplack†, H. M. Nagy†, K. D. Paulsen§
† Dept. of Radiology, Dartmouth-Hitchcock Medical Center § Thayer School of Engineering, Dartmouth College

Tissue elasticity is thought to hold great promise for the diagnosis of cancer because it is often harder than normal tissue. MR based methods encode the static displacements [1] or dynamic displacements [2,3] in the phase and reconstruct the elasticity from the motion.

We have used dynamic displacements because density and frequency effects can be evaluated as well as the elasticity. The gradient echo sequence below was implemented on a GE MRI. The RF amplifier was blanked during the 100Hz sinusoid on the RF channel. It was fed into the power amplifier for the piezoelectric actuator stacks. The 100Hz sinusoidal gradients encoded the harmonic displacement. The 3 gradients allowed displacement in all 3 directions to be measured. The relative phase between the gradients and the



motion was controlled very precisely by changing the starting time of the gradient pulse. Four starting times were used and phase at each position was fit to: $\phi = C + A \cos(\omega t + P)$. The first term is an irrelevant constant. The amplitude and phase of the cos term describe the harmonic motion completely.

The motion was produced by three stacks of piezoelectric actuators. Three actuators were used to get sufficient displacement. Three stacks gave mechanical stability. The system was current limited with one audio amplifier; in independent measurements the device produced 24 micron displacements. The specifications state that the stacks can provide 42 micron displacements with sufficient current. The device generates large forces which is an important advantage.

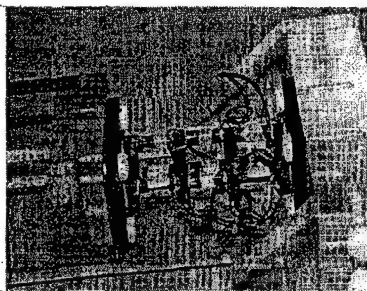


Fig. 1: Three stacks of piezoelectric actuators mounted to vibrate a box.

Discussion: Because the measured displacement patterns match the calculated patterns quite well, we are confident that we have made accurate measurements of the motion and accurate calculations of the motion. The magnitude of the simulated displacements are larger than the measured values. Damping, transient effects, and changes in Poisson's ratio could all account for the variation.

References:

- 1) T.L. Chenevert et. al.: *Mag. Reson. Med.* 39(3):482 1998.
- 2) R. Muthupillai et. al.: *Science* Vol. 269:1854, 1995.
- 3) J. Bishop et. al.: *JMRI* 8: 1257, 1998.

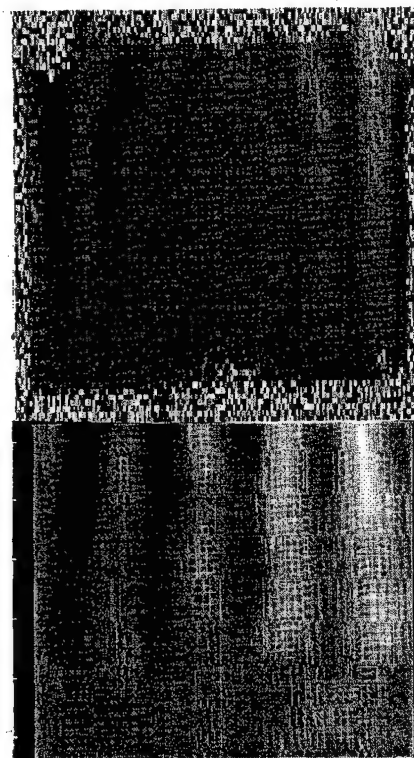
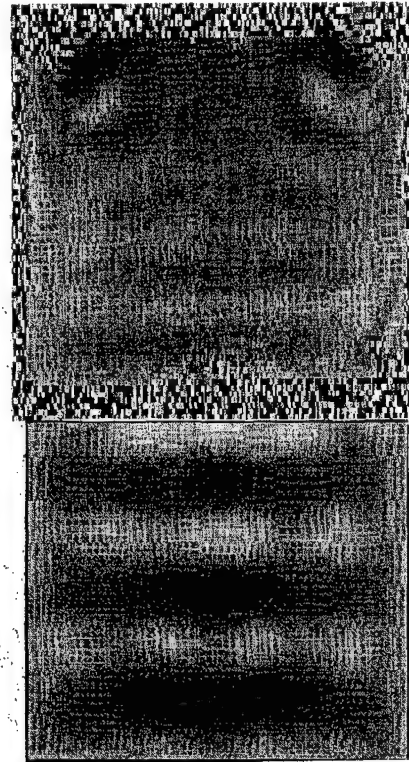


Fig. 2: The measured displacement amplitudes in the X and Y directions in a homogeneous agar gel are shown in Figs. a and b. The TR=300ms, TE=58ms, NEX=2, SL=1cm, FOV=8cm, resolution is 128 x 256. Figs. c and d show the forward simulation for that geometry and material.

MRI Elastography Reconstruction Using A Harmonic Elastodynamic Model

Elijah Van Houten, Michael I. Miga, Francis E. Kennedy, John B. Weaver, Keith D. Paulsen

*Thayer School of Engineering, Dartmouth College, HB8000, Hanover, NH 03755

Abstract

Recently, imaging modalities such as ultrasound and magnetic resonance (MR) have been used to measure subsurface displacements in tissue and several inversion schemes have been proposed to solve for stiffness properties. We have developed a finite element based inversion scheme which operates in a sweeping fashion on small overlapping subzones of the tissue space. The zone approach allows for a high degree of spatial discretization while maintaining algorithm convergence. Additionally, we are using a harmonic elastodynamic tissue model as the basis of our inversion and have shown accurate reconstruction simulations with up to 15% added noise.

Introduction

Palpation, although effective at diagnosing large near-surface cancerous tissue, is not an adequate technique for detecting small deep tumors. However, based on the success of palpation, the high contrast in stiffness between healthy and cancerous tissues remains an impetus for developing an elastographic imaging modality. MR and ultrasound elastography are the first imaging modalities to provide subsurface displacement data, which consequently provides tissue strain information, that can be used in an inverse method to recover stiffness properties.

Methods

Previous work has focused on estimating stiffness properties by calculating local wavelengths resulting from shear excitation of the tissue [1]. More recently model based reconstruction has been used in this same context [2]. It has been our experience that shear wave excitation of tissue is limited due to attenuation. In our approach, we use longitudinal harmonic waves which ultimately generate standing shear waves deep within the tissue.

The equations describing the elastodynamic response of soft tissue under an applied harmonic deformation are,

$$\rho \frac{\partial^2 \mathbf{u}}{\partial t^2} = \nabla \cdot \boldsymbol{\tau}. \quad (1)$$

where $\boldsymbol{\tau}$ is the stress tensor, \mathbf{u} is the displacement vector and ρ is the tissue density. Assuming that the material is excited harmonically at frequency ω , these equations can be solved in the frequency domain,

$$\rho \omega^2 \mathbf{U} = \nabla \cdot \mathbf{T}. \quad (2)$$

where $\mathbf{u} = \mathbf{U}e^{i\omega t}$. Depending on the constitutive relationships assumed between stress and strain, the presence of damping can be incorporated; however, for this discussion we have assumed Hookean dependence with a constant Poisson's ratio of $\nu = 0.49$; thus leaving Young's modulus the only unknown in the domain (recall that displacement data, \mathbf{u} , is measured from the imaging technique).

The inversion problem is a nonlinear Newton-based iterative scheme which minimizes the square of the error between measured and model-predicted values for each zone and solves for the distribution of Young's modulus. The zone domain is radially shaped and determined by a hierarchical ordering of local residual errors which cover the entire mesh (zone boundary conditions are determined from the MR dataset). After

all areas of the mesh have been iterated on a specified number of times (zone iterations vary due to overlapping capability), a global forward problem is executed using the updated modulus distribution and the zone process begins again. The main advantage of this technique is that it allows sufficient discretization to resolve the wavelengths found in soft tissue harmonic motion.

Results & Discussion

Using this inversion scheme, a simulation was performed on a breast cross-section with complex phantom shapes of varying contrast. Random noise (up to 15 % of original displacement) was added to the forward solution data to simulate signal degradation in the MR measurements. This noisy solution is then operated on by the inversion algorithm described previously. Figure 1 shows the results with an initial guess of a uniform Young's modulus of 7000 Pa. The inversion process

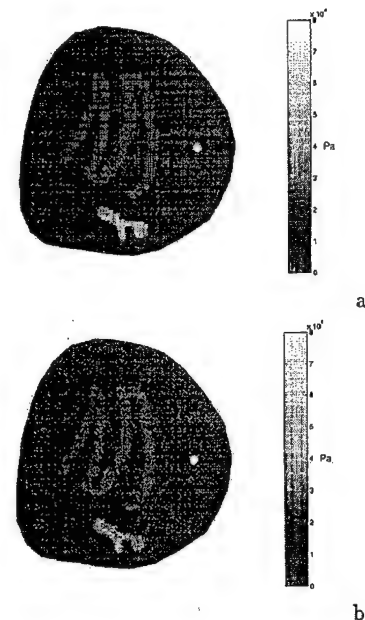


Figure 1: Breast computational phantom/reconstruction with regions of varying contrast (2x, 5x, 10x): (a) phantom Young's modulus distribution, (b) inverse solution with 15% random noise added to data.

consisted of 18 sweeps over the entire space, each sweep using roughly 1000 zones of about 150 elements and 100 nodes to insure that every node within the discretization was operated on at least once. Overall the results shown in our simulations are extremely encouraging. This work was supported by NIH grant R01-NS33900 awarded by the NINDS.

References

1. R. Mathupillai, et al. *Magnetic Resonance in Medicine*, 36, 266-274, 1996.
2. A. Manduca, et al. *Lecture Notes in Computer Science*, 1496, 606-613, 1998.

Contrast Enhancement Using Monotonic Noise Suppression Methods

John B. Weaver, Department of Radiology, Dartmouth-Hitchcock Medical Center

This work was supported by DOD-AMRD, DAMD17-96-1-6119

We introduced monotonic noise suppression and applied it to improving fMRI activation maps. Now we are using monotonic noise suppression to increasing contrast in images. Almost any noise reduction algorithm can be used to enhance contrast. Monotonic noise suppression has some advantages over the wavelet denoising based contrast enhancement method we introduced previously.

The basic idea is to subtract two versions of the image obtained by using two different noise thresholds. The first image is filtered to remove just the noise. The second image is filtered to remove noise and small features leaving only the large features. When the second image is subtracted from the first, the large features are subtracted away leaving the small features. Actually the second image times some factor less than one is subtracted; so the large features are reduced rather than eliminated. The amount of contrast enhancement can be changed by changing the linear combination of filtered images.

Two features of the monotonic noise reduction method make it attractive for this application. First, it is not band-limited. Edges are not blurred at all. There is no reduction of sharpness in the contrast enhanced image. Second, there is no ringing caused by undersampling. When a noise reduction method that introduces ringing into the image, the ringing can be amplified and distorted to look like small features in the contrast enhanced image. Fourier noise reduction methods are infamous for introducing ringing and wavelet denoising also introduces ringing although to a lesser extent.

Contrast Enhancement Using Monotonic Noise Suppression Methods

John B. Weaver, Department of Radiology, Dartmouth-Hitchcock Medical Center

This work was supported by DOD-AMRD, DAMD17-96-1-6119

Contrast enhancement requires the balance of two competing features: making small changes in the image bigger and controlling the growth of noise. There are two general types of techniques that have been used in the past to enhance contrast. The first is contrast equalization. However, it does not do well when there are big bright and big dark areas with low contrast objects in each because the large bright and dark areas dominate the histogram and do not help the low contrast objects in between. (See Gonzalez and Wintz, Digital Image Processing, Section 4.2.3)

The second class of contrast enhancement techniques that have been used in medical imaging are variants of transform based noise reduction methods. We developed a wavelet based algorithm that is used in mammography by several groups [Lu 1994]. One way of seeing the process is that the coarse shape of the object (formed by the coarse scale coefficients) is extracted and allowed less of the dynamic range to make room for the midscale coefficients. The idea is the same as the old blurred mask or unsharp masking methods.

The contrast enhancement method we are presenting here follows the same form as the wavelet based one described above. But, we are using the monotonic noise reduction algorithm [Weaver 1997 a&b] that we have used for noise reduction in fMRI studies [Weaver 1998].

We describe monotonic noise reduction and then shown how it is used to enhance contrast.

Monotonic Noise Reduction:

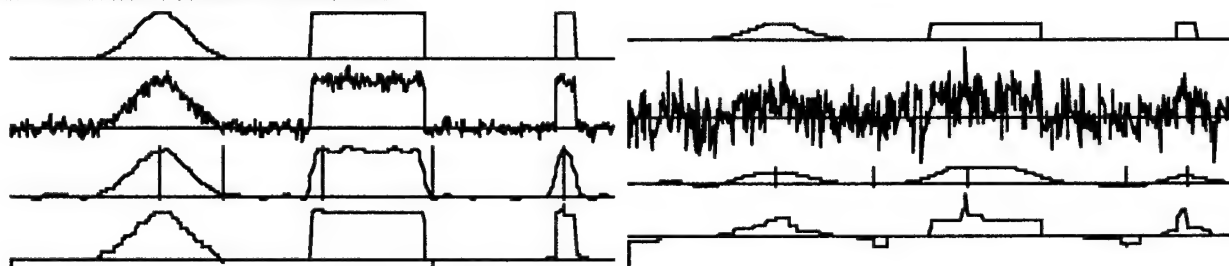


Figure : Monotonic noise reduction works in 1D. The layout is the same for both figures. The top is the original signal. The next line is the signal with added noise; SNR=10 on the left and SNR=1 on the right. The next line is the blurred signal with the selected extrema. The filtered signal is shown at the bottom. The filtered signal is the best monotonic fit between selected extrema. The results are quite good even at very low SNR. There is no blurring of the edges and no ringing. The only distortion is the noise leakage at the extrema.



Figure : A sagittal MRI image is shown at the left; SNR=80. The middle is the original image with added noise; SNR=16. The right is the result of monotonic noise reduction; SNR=85. The images are of good quality with no blurring or distortion. Monotonic noise reduction works with much lower SNR than common wavelet denoising algorithms.

Contrast Enhancement: Two features of the monotonic noise reduction method make it attractive for contrast enhancement. 1) It is not band-limited; edges are not blurred at all. So there is no reduction of sharpness in the contrast enhanced image. 2) There is no ringing caused by undersampling in monotonic noise reduction. Ringing must be controlled just as noise must in the contrast enhanced images or they will dominate the image.



Figure 1: An image from an fMRI study. The contrast is low as it generally is in fMRI studies. The image on the right is the contrast enhanced image. The darker areas are darker and the brighter areas are brighter than in the original image. No visible artifacts were introduced in the contrast enhanced image. However, the artifacts that were present in the original image are enhanced just as the small features are. The general intensity distribution remains the same so the "look and feel" of the contrast enhanced image is the same as the original image.

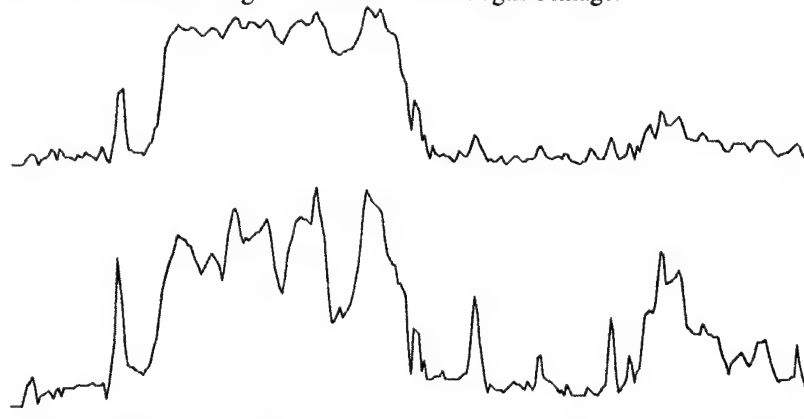


Figure 2: The top curve is the 180th column of the original image. The bottom curve is the 180th column of the contrast enhanced image. The same peaks are present but the size of the peaks are equalized: the larger discontinuities are relatively smaller and the smaller peaks are relatively larger. The relative sizes of the peaks are generally the same so the "look and feel" of the image is the same unlike histogram equalized images.

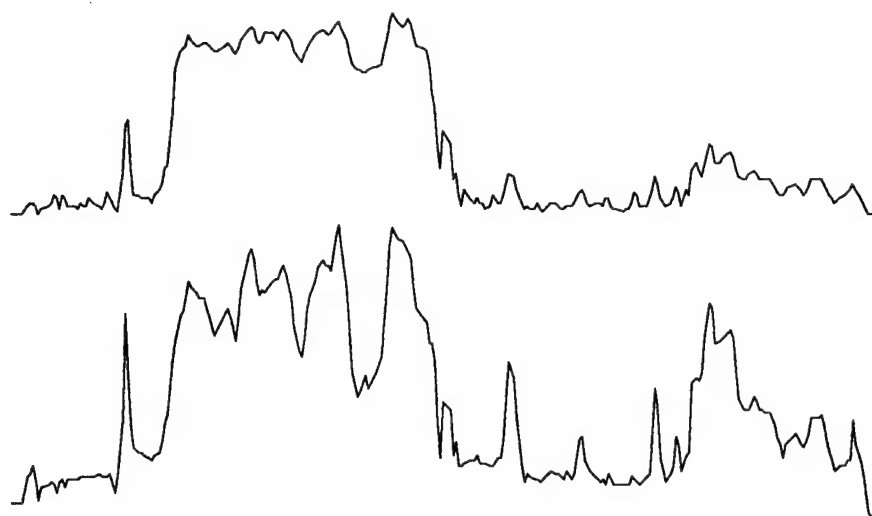
Figs. 1 & 2 show that the contrast has been enhanced without allowing noise to dominate. Each feature in the contrast enhanced image can be seen in the original image but less clearly.

Jian Lu, D.M. Healy, Jr. and J.B. Weaver: "Contrast Enhancement of Medical Images Using Multiscale Edge Representation." *Optical Engineering*, 33(7), 2151-61, 1994.

J.B. Weaver: "Reducing Noise in Images by Forcing Monotonic Change Between Extrema," The International Society for Analysis, its Applications and Computation (ISAAC), 1997.

J.B. Weaver: "Removing Noise from Images: Least Squares Monotonic Functions on Line Segments Through the Image" Proceedings of the Society of Magnetic Resonance, Vancouver, Canada, August, 1997, p 2043.

J. B. Weaver: "Monotonic Noise Suppression Used to Improve the Sensitivity of fMRI Activation Maps." Society of Computer Applications in Radiology (SCAR) 1998, Journal of Digital Imaging.



Elasticity estimates using phase contrast MRI measurements of displacement.

by

John B. Weaver †, Elijah van Houten §, Michael I. Miga §, Francis E. Kennedy §, Steven P. Poplack †, Helene M. Nagy †, Keith D. Paulsen §

† Department of Radiology, Dartmouth-Hitchcock Medical Center

§ Thayer School of Engineering, Dartmouth College

We are studying methods of reconstructing the elasticity from MRI measurements of tissue vibration. There has been significant interest in estimating tissue elasticity from MRI phase contrast measurements of periodic and quasi-static displacement. MRI seems to hold more promise than ultrasound because of its ability to measure small tissue displacements simultaneously in all three directions resulting from a single mechanical stimulus while ultrasound is limited to recording tissue displacements in one preferred direction at a time.

We have calculated tissue displacements with the partial differential equations describing dynamic and static elastic deformation. Models of the breast were generated from MRI scan data. We have performed simulations for various modes of vibration. These simulations have led to three conclusions which impact how estimates of elasticity can be obtained from displacement fields:

- 1) If the driving displacement is large enough to obtain 3D MR phase contrast images in reasonable times, there is likely to be significant displacement in directions perpendicular to the direction of the driving force.
 - 2) Multi-dimensional displacement (e.g. in directions other than in-line with the driving force) requires partial differential equation solution to adequately describe the displacement field.
 - 3) Because partial differential equations are necessary to describe the motion, those equations must be used to estimate the elasticity.
- If the displacement is all essentially in the direction of the driving force, simple local estimates of the elasticity would be possible.

Removing Noise from Images: Least Squares Monotonic Functions on Line Segments Through the Image

John B. Weaver

Department of Radiology, Dartmouth-Hitchcock Medical Center, Lebanon, N.H.

Introduction:

We introduce a new method of removing noise from images. The method selects significant maxima (includes the minima) in the image and forces the pixel values in the filtered image to vary monotonically in all directions between those maxima. For example, if an isolated maximum is identified, the filtered image should fall away from it monotonically in all directions. We can only perform monotonic fits in one dimension, so we approximate monotonicity in all directions by doing monotonic fits along line segments through out the image. The line segments are bounded by maxima and are oriented in many directions through the image. The filtering operation on each line segment replaces the pixel values on that segment with a 1D monotonic sequence that fits the original pixel values best in a least squares sense. The method is simple, relatively fast and stable. SNR's as low as 0.1 can produce acceptable results.

Methods:

An intermediate filtered image is found at each angle. The original image is rotated to the appropriate angle. The rotated image is blurred using a simple Gaussian filter in the Fourier domain. The maxima along the rows of the image are identified. The maxima that differ from the adjacent maxima by less than the threshold are removed from the set. In each row, all sequences of adjacent pixels ending in maxima are replaced by the monotonic sequence that best fits the original pixel values [1,2]. Then the same procedure is followed on the columns of the row filtered image. Remarkably, the rows stay essentially monotonic when the columns are processed. The row-column filtered image is averaged with the column-row filtered image and rotated back to the original orientation. The result is the intermediate filtered image for that angle. Intermediate filtered images are obtained for each angle. The final

filtered image is a least squares combination of all of the intermediate filtered images. The final filtered image is almost monotonic between maxima in all directions.



Fig. 1 An example of the filter on a row. a) signal: two boxcars with noise, SNR=1. b) the blurred signal and the identified maxima. c) result of the monotonic fits superimposed on the original boxcars. Peaks in the filtered signal is noise that passes through the filter at the maxima when the SNR is very low. Note that the edges of the recovered boxcars are sharp & in the correct positions.

Conclusions:

We have presented a method of removing noise from images using monotonic fits between maxima. It does not blur edges, is robust and can be effective on images with very low SNR's unlike most wavelet denoising methods. However, it does not yet have the mathematical structure and rigor that wavelet denoising methods have. It also leaves point noise at the maxima at very low SNR's.

- 1 I.C. Demetriou and M.J.D. Powell, *IMA Journal of Numerical Analysis* 11:411-432 1991.
- 2 J.B. Weaver, et al. *SPIE: Medical Imaging* 2710-79, 1996.

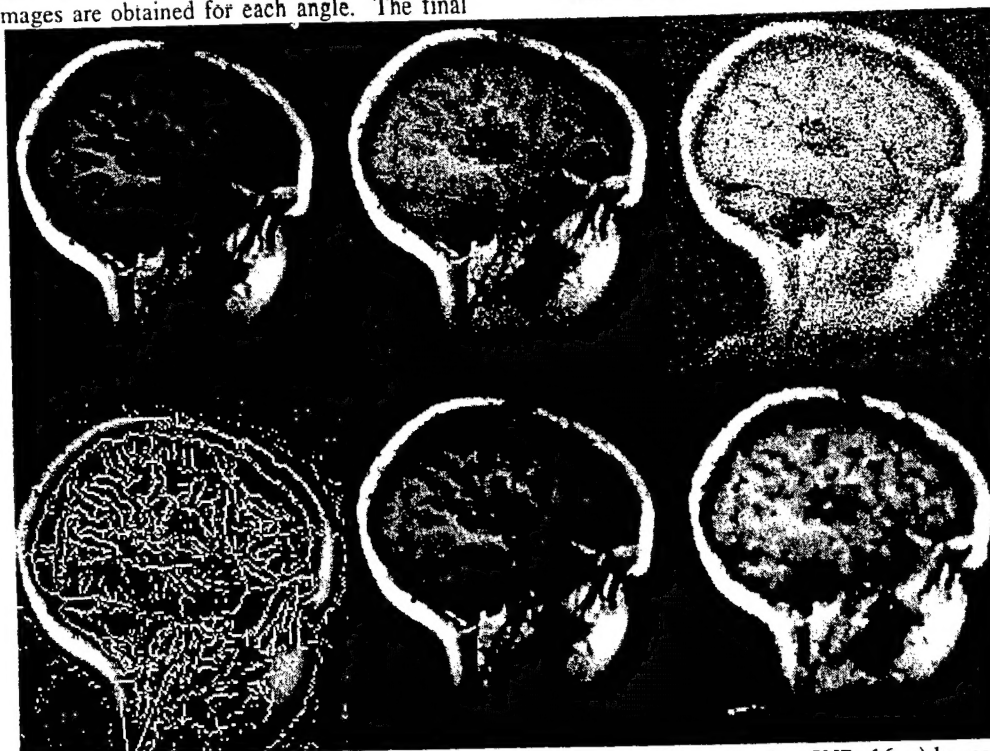


Fig. 2 a) original high SNR image, SNR=80 within brain. b) image with added noise, SNR=16. c) lower SNR=4. d) Gaussian blurred b showing the maxima. e) result of filter on b, SNR=85. f) result of filter on c, SNR=30.

Acquisition of MR Elastography Measurements Using Steady State Motion

John B. Weaver*, Elijah Van Houten†, Michael I. Miga†, Francis E. Kennedy†, Keith D. Paulsen†

*Dartmouth-Hitchcock Medical Center, Lebanon, N.H. 03756 and †Thayer School of Engineering, Dartmouth College

Abstract

We have developed a method of reconstructing the tissue elasticity from MR displacement measurements. The model used to reconstruct the elasticity is based on the partial differential equations describing steady state, harmonic motion. Therefore, we have developed a system to generate true steady state motion within tissue as well as within gel samples. Our first motion maps and reconstructions from a homogeneous gel phantom are shown.

Introduction

Measurements of harmonic motion and quasi-static displacement can be accomplished accurately using MR [1,2,3]. The inversion of that data to estimate the mechanical properties of the tissue has proved to be a difficult problem. Currently several groups have taken different approaches and the MR acquisition has been modified to fit the inversion approach. Methods to estimate the elasticity from traveling waves and from quasi-static displacements have been developed. In all of these methods, reconstruction has been problematic. We have implemented an inversion method using finite element solutions to the partial differential equations describing the elastodynamic response of soft tissue under an applied harmonic deformation. The inversion method is a nonlinear Newton-based iterative scheme which finds the distribution of Young's modulus which minimizes the difference between the measured and model-predicted displacement values [4]. The problem with our previous MR acquisitions is that the motion is started and stopped during each cycle of the pulse sequence and we have suggested that the transients in the motion produce incorrect reconstructions [5,6]. Therefore, we have developed a method of measuring displacements during steady state motion.

Methods

With simulations we have estimated that 100 cycles of 100 Hz motion allow the transients to dissipate for a wide variety of mechanical properties and geometries. It is impractical to get 100 cycles of motion for each MR excitation so we kept the motion going throughout the gradient echo pulse sequence. The motion was small enough that it did not disturb the signal significantly except when the motion sensitizing gradients were on. The difference between an image with and without the motion was negligibly small without the motion sensitizing gradients, which were two sine waves just before the read-out.

The signal used to drive the gel sample was produced by an HP 33120A signal generator that was phase locked to the 10 MHz MR system clock. The signal generator was setup to generate a set number of 100 Hz sine waves after it was triggered with a pulse from the MR. The signal generator then drives the sample at 100 Hz for the duration of the pulse sequence. The initial phase of the 100 Hz signal was controlled by the signal generator and could be set by the operator. That initial phase controls the relative phase between the motion and the motion sensitizing gradients which must be changed to determine the motion in each voxel. To keep the motion synchronized with the pulse sequence throughout, the actual TR must be an integer multiple of the 10 msec cycle. The measured TR was actually 1 msec more than the TR set on the console. The signal from the signal generator was the input of a power am-

plifier that drove a set of 6 piezoelectric stacks that vibrated the sample.

Results

Our first maps of steady state motion in a homogeneous gel sample are shown below. The reconstruction of the elasticity is also presented. The average elasticity in the image is approximately what we expect from physical measurements in the gel, around 20 kPa. The reconstruction is fairly uniform, although there is some structure in the image where the recovered values deviate from the nominal level.

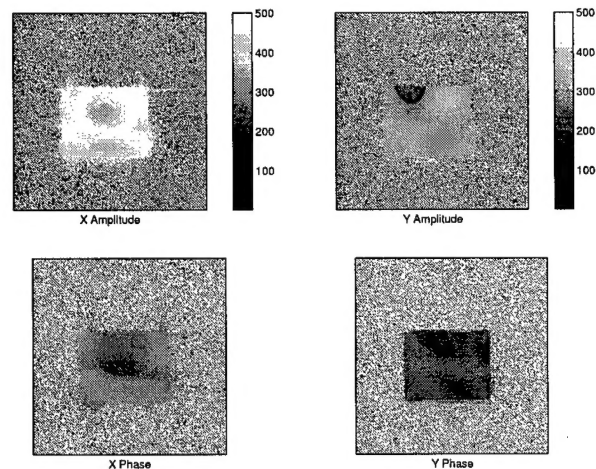


Figure 1: The amplitudes and phases of the harmonic steady state motion in an essentially homogeneous agar gel phantom.

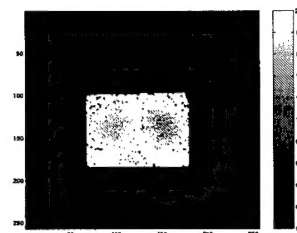


Figure 2: The elasticity reconstructed from the motion shown above in an essentially homogeneous agar gel phantom.

This work was supported by NIH grant R01-NS33900, NSF grant BCS-9978116 and NIH grant P01 CA80139-01A1.

References

1. R. Mathupillai, et al. *Mag. Reson. in Med.*, 36, 266, 1996.
2. T.L. Chenevert, et al. *Mag. Reson. in Med.*, 39, 482, 1998.
3. J. Bishop, et al. *JMRI*, 8:1257, 1998.
4. E.E.W. Van Houten, et al. *Mag. Reson. in Med.*, 42, 779, 1999.
5. E.E.W. Van Houten, et. al. *Proceedings of the Society of Mag. Reson.*, May, 1999, p. 260.
6. J.B. Weaver, et. al. *Proceedings of the Society of Mag. Reson.*, May, 1999, p. 1617.

Three Dimensional Reconstructive Elastographic Imaging

Elijah E.W. Van Houten, Michael I. Miga, Francis E. Kennedy, John B. Weaver, Keith D. Paulsen

*Thayer School of Engineering, Dartmouth College, HB8000, Hanover, NH 03755

Abstract

Recently, a variety of methods for generating elastic contrast images of biological tissue have been put forward [1,2,3]. To date the large majority of these methods have been developed under assumptions of two dimensional mechanical behavior for the tissue in question. While this may well be valid in certain idealized conditions, it is by no means accurate for the general case, especially for non-symmetric tissue geometries or property distributions. In these situations, a three dimensional property reconstruction scheme will be necessary. Here, our efforts to develop a three dimensional elastic property reconstruction scheme are discussed and simulation results are presented.

Introduction

MR based elastic property imaging is a rapidly evolving field which seeks to determine the mechanical property distribution within a tissue region using displacement or strain information obtained for that region. This approach is necessary as a tissue's characteristic elastic makeup is not directly visible by means of magnetic resonance or ultrasound imaging. For the most part, the schemes developed for reconstructive imaging have been presented using two dimensional assumptions. While such assumptions are valid in certain cases, namely perfect symmetry in both property distribution and geometry, they will not be valid in a general heterogeneous tissue, such as the human breast. In these instances motion or strain in the third dimension is not insignificant and must be accounted for.

Methods

Previously, a finite element implementation of a subzone based elasticity reconstruction scheme has been presented [2]. This method uses the full field displacement data available from the MR to drive a non-linear reconstruction process based on squared error minimization. This approach, documented using a two dimensional plane strain approximation, is fully amenable to a complete, three dimensional treatment. Using a linear elastic model as the basic assumption for tissue motion, the governing equation for the harmonic tissue response is

$$\nabla \cdot G \nabla \mathbf{u} + \nabla (\lambda + G) \nabla \cdot \mathbf{u} = \rho \omega^2 \mathbf{u}. \quad (1)$$

The inversion process based upon the three dimensional equations of linear elasticity is executed in a similar fashion to the two dimensional scheme, with one notable exception. The automated zoning process for the two dimensional inversion problem is driven by a hierarchical ordering of element based error, requiring a global solution using the current property distribution estimate for every global iteration. For high resolution three dimensional problems global solutions are too costly to perform at each global inversion iteration. Thus, for the three dimensional inversion algorithm the zone location is selected in a random manner from the list of elements not yet operated on during the current iteration step.

Results & Discussion

Initial simulation experiments have been performed, fig. 1,

using displacements generated through a finite element solution with 15% random noise added to the data. To minimize the effects of such added noise on the inversion solution, a small degree of spatial filtering was used during the inversion process. This is achieved by incorporating the current property estimate of nodes in direct contact with a given node, i , such that $E_i^{new} = (1 - \theta)E_i^{old} + \frac{\theta}{N_i} \sum_{j=1}^{N_i} E_j^{old}$, where N_i is the number of neighbor nodes connected to node i . For this experiment a value of 0.05 was used for θ .

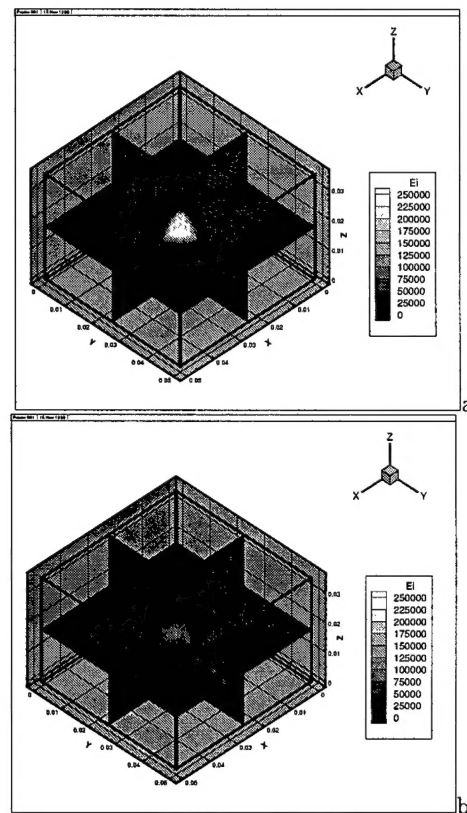


Figure 1: Three dimensional phantom simulation reconstruction for a 5cm x 5cm x 3.5cm geometry with a 25 kPa background Young's modulus and a 1 cm diameter 250 kPa spherical inclusion. (a) Inversion solution for 0% noise case. (b) Inversion solution for 15% noise solution.

The inversion process consisted of roughly 20 global iterations, each consisting of 300 zone based parameter updates on average, with the average zone size being roughly 330 nodes. The total solution consists of 24094 nodal stiffness values. This work was supported in part by NIH grant 530374.

References

1. R. Mathupillai, et al. *Magnetic Resonance in Medicine*, 36, 266-274, 1996.
2. E.E.W. Van Houten, et al. *Magnetic Resonance in Medicine*, 42, 779-786, 1999.
3. T.L. Chenevert, et al. *Magnetic Resonance in Medicine*, 39, 482-490, 1998.